Physics of Microswimmers – Single Particle Motion and Collective Behavior

Jens Elgeti, Roland G. Winkler, Gerhard Gompper*

(Dated: December 9, 2014)

Locomotion and transport of microorganisms in fluids is an essential aspect of life. Search for food, orientation toward light, spreading of off-spring, and the formation of colonies are only possible due to locomotion. Swimming at the microscale occurs at low Reynolds numbers, where fluid friction and viscosity dominates over inertia. Here, evolution achieved propulsion mechanisms, which overcome and even exploit drag. Prominent propulsion mechanisms are rotating helical flagella, exploited by many bacteria, and snake-like or whip-like motion of eukaryotic flagella, utilized by sperm and algae. For artificial microswimmers, alternative concepts to convert chemical energy or heat into directed motion can be employed, which are potentially more efficient. The dynamics of microswimmers comprises many facets, which are all required to achieve locomotion. In this article, we review the physics of locomotion of biological and synthetic microswimmers, and the collective behavior of their assemblies. Starting from individual microswimmers, we describe the various propulsion mechanism of biological and synthetic systems and address the hydrodynamic aspects of swimming. This comprises synchronization and the concerted beating of flagella and cilia. In addition, the swimming behavior next to surfaces is examined. Finally, collective and cooperate phenomena of various types of isotropic and anisotropic swimmers with and without hydrodynamic interactions are discussed.

CONTENTS

* Theoretical Soft Matter and Biophysics, Institute of Complex Systems and Institute for Advanced Simulation, Forschungszentrum Jülich, D-52425 Jülich, Germany

I. INTRODUCTION

Cell motility is a major achievement of biological evolution and is essential for a wide spectrum of cellular activities. Microorganisms, such as spermatozoa, bacteria, protozoa, and algae, use flagella—whip-like structures protruding from their bodies—for their propulsion. Swimming of uni- and multi-cellular organisms is essential for their search for food (chemotaxis), the reaction to light (phototaxis), and the orientation in the gravitation field (gravitaxis). Furthermore, flagellar motion plays a major role in higher organisms, where they transport fluid in the respiratory system in form of cilia, are involved in cellular communications, and even determine the morphological left-right asymmetry in the embryo.

Unicellular swimmers, e.g., bacteria like *Escherichia coli*, spermatozoa, and *Paramecia* are typically of a few to several ten micrometers in size. The physics ruling

the swimming on this micrometer scale is very different from that applying to swimming in the macro-world. Swimming at the micrometer scale is swimming at low Reynolds numbers (Purcell, 1977), where viscous damping by far dominates over inertia. Hence, swimming concepts of the high Reynolds-number macro-world are ineffective on small scales. In the evolutionary process, microorganisms acquired propulsion strategies, which successfully overcome and even exploit viscous drag.

The design of artificial nano- and microswimmers is highly desirable to perform a multitude of tasks in technical and medical applications. Two general design strategies are currently followed, each posing particular challenges. First, successful concepts realized in nature can be adopted or underlying principles and mechanisms can be exploited. Second, novel construction principles can be invented, which are simpler but potentially more efficient, or plainly more practical from an engineering perspective. Major obstacles in such an endeavor are the availability of sustainable energy sources for artificial microswimmers, and physical concepts for efficient energy conversion into a propulsive force. Another issue is the active control of artificial microswimmers, such that they perform tasks or respond to external stimuli. The design and fabrication of a synthetic swimmer with such features would be extremely valuable in a diversity of fields like medicine, biology, material science, and environmental science. Such machines might transport cargo, e.g., in medicine or microfluidic chips, conduct operations in cells, remove toxic materials from human bodies or toxic water streams, or actively control material behavior as, e.g., viscoelastic properties.

Microswimmers hardly ever swim alone. Sperm cells are released by the millions to compete in the run for the egg. Bacteria grow by dividing and invading their surroundings together. Artificial microswimmers will only be able to deliver useful quantities of pharmaceuticals or modify material properties when present in large numbers. Indeed, in assemblies of motile microorganisms, cooperativity reaches a new level of complexity as they exhibit highly organized movements with remarkable large-scale patterns such as networks, complex vortices, or swarms.

In this article, we review the physics of locomotion of biological and synthetic microswimmers, and the emergent collective behavior of their assemblies. Several previous review articles concerning microswimmers have addressed different aspects of their motility and collective behavior. Generic aspects of the emergent large-scale behavior of self-propelled particles and active soft matter have been reviewed by Toner *et al.* (2005a), Ramaswamy (2010), Vicsek and Zafeiris (2012), Marchetti *et al.* (2013), and Saintillan and Shelley (2013). The hydrodynamics of swimming has been reviewed by Lauga and Powers (2009), Ishikawa (2009), Koch and Subramanian (2011), and Golestanian *et al.* (2011). Aspects of bacterial motility have been discussed by Harshey (2003) and Cates (2012). Sperm motility and chemotaxis has been reviewed by Alvarez *et al.* (2014). The dynamical properties of active Brownian particles have been discussed by Romanczuk *et al.* (2012), with emphasize on the stochastic dynamics in the framework of statistical physics. The propulsion of synthetic swimmer on the nanoscale and the development of nanomachines have been addressed by Ozin *et al.* (2005), Sengupta *et al.* (2012), and Ebbens and Howse (2010).

A. Biological Microswimmers

Flagellated Bacteria. A wide variety of bacteria exploit helical filaments, called flagella, for their propulsion. Different species possess various numbers and different arrangements of flagella. According to the arrangement, flagellated bacteria are classified as *monotrichous* bacteria which possess a single flagellum only, *lophotrichous*, bacteria with multiple flagella located at a particular spot on their surface, *amphitrichous* bacteria grow a single flagellum on each of the two opposite ends, and *peritrichous* bacteria are covered by multiple flagella pointing in all directions (Janssen and Graham, 2011). Prominent examples of *peritrichous* bacteria are *Escherichia coli* (Berg, 2004), *Salmonella typhimurium*, see Fig. 1, *Rhizobium lupini*, or *Proteus mirabilis* bacteria to name just a few. A flagellum is rotated by a motor complex, which consists of several proteins, and is anchored in the bacterial cell wall (Berg, 2003, 2004; Brennen and Winet, 1977), see Fig. 2. The motor itself is connected to the flagellum by a flexible hook.

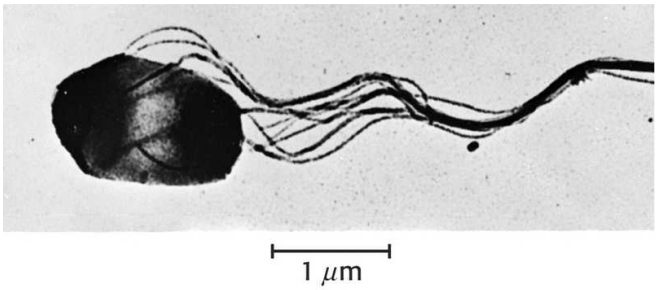

FIG. 1 Salmonella swim by a bundle of rotating helical flagella. From Brennen and Winet (1977).

Bacteria like *E. coli* and *Salmonella* swim in a "run-and-tumble" motion illustrated in Fig. 3 (Berg, 2004; Hyon *et al.*, 2012; Macnab, 1977; Turner *et al.*, 2000). In the "run" phase (stage 1 in Fig. 3), the helical winding of all flagella is left-handed, and they rotate counterclockwise. The flagella form a bundle (see also Fig. 1), and the bacterium moves forward in a direction determined by its long axis. At the beginning of the "tumble" phase, one flagellum reverses its rotational direction to clockwise (stage 2 in Fig. 3). The flagellum leaves the bundle

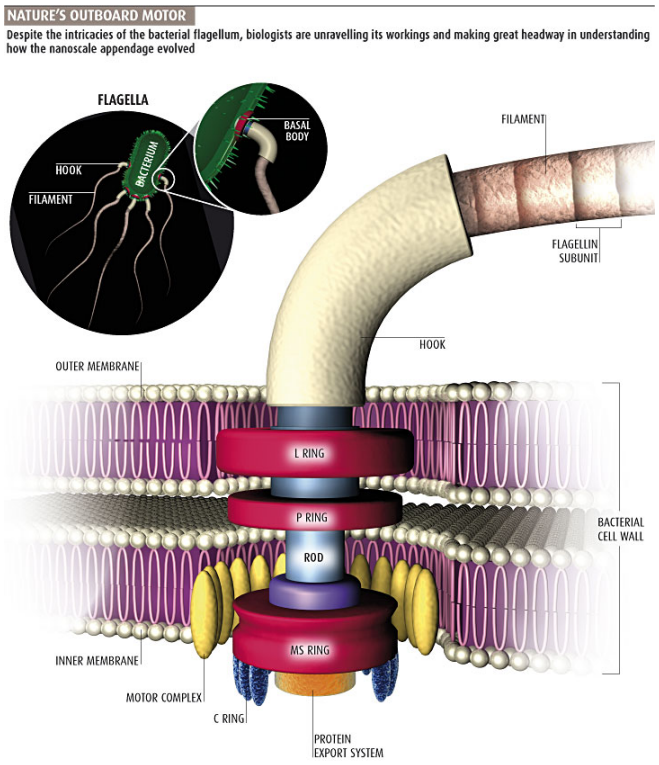

FIG. 2 Each bacterial flagellum is driven by a rotary motor embedded in the bacterial cell wall. The motor has a series of rings, each about 20 nanometers in diameter, with a rod inside. Attached to the rod is a curved "hook" protein linked to the flagellum. The flagellum is 5 to 15 micrometers long and made of thousands of repeating units of the protein flagellin. The motor is powered by the flow of sodium or hydrogen ions across the cell wall. From Jones (2008).

which implies a random reorientation of the bacterium (stage 3 and 4). The reversal of the rotational direction is accompanied by a change of the helical handedness from left-handed to right-handed and the flagellum undergoes a polymorphic transition (Armitage and Macnab, 1987; Calladine, 1975; Calladine *et al.*, 2013; Darnton and Berg, 2007; Darnton *et al.*, 2007; Macnab, 1977; Shah *et al.*, 2000; Vogel and Stark, 2010, 2013). At the end of the "tumbling" phase, all flagella start to rotate again in the same counterclockwise direction (stage 5), the bundle reforms (stage 6), and the bacterium returns to a directional motion (stage 7 and 8).

The flagella of bacteria like *Rhizobium meliloti* or *Rhizobium lupini* are only capable of limited polymorphic transitions and their motors are unidirectional (Platzer *et al.*, 1997; Scharf, 2002; Schmitt, 2002). These bacteria modulate the rotation speed of individual motors to induce tumbling (Platzer *et al.*, 1997; Scharf, 2002).

Uni-flagellated bacteria, e.g., *Vibrio alginolyticus*, tumble by motion reversal and by exploition of a buckling instability of their hook (Son *et al.*, 2013). This mechanism represents an example of one of the smallest

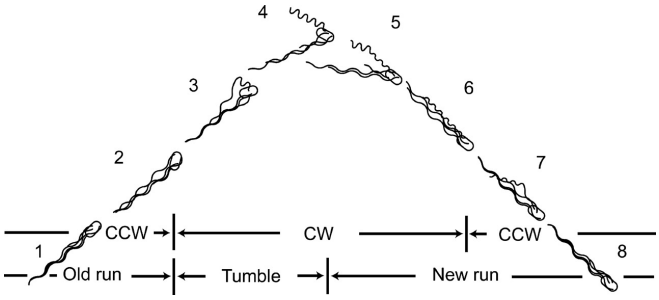

FIG. 3 Bacteria like *E. coli* and *salmonella* move by a "run-and-tumble" motion. During the "run" phase, the flagella form a bundle, and the bacterium moves forward in one direction. In the "tumble" phase, one or a few flagella reverse their rotational direction and leave the bundle. This induces a tumbling motion which changes the orientation of the bacterium randomly. CW denotes clockwise, CCW counterclockwise rotation. From Darnton *et al.* (2007).

engines in nature where a biological function arises from controlled mechanical failure, and reveals a new role of flexibility in biological materials.

The purpose of the "run-and-tumble" motion is to detect gradients in the concentration of chemicals (e.g. food) or temperature (to avoid regions of too high or too low temperature). This is achieved by extending the "run" phase in case of improving environmental conditions, and by shortening it in case of worsening conditions.

Bacteria not only swim as individuals, but exhibit collective behavior at a moist surface or in a thin liquid film in form of swarming (Copeland and Weibel, 2009; Darnton *et al.*, 2010; Kearns, 2010; Partridge and Harshey, 2013b). Swarming was distinguished from other forms of surface translation (Darnton *et al.*, 2010; Heinrichsen, 1978; Kearns, 2010), e.g., swimming, due to particular shape changes which swarming bacteria undergo. During the transition from swimming to swarming cells, the number of flagella increase and the cells become often more elongated by suppression of cell division (Darnton *et al.*, 2010; Jones *et al.*, 2004; Kearns, 2010; Stahl *et al.*, 1983). This points toward the significance of flagella and flagella interactions between adjacent cells (Jones *et al.*, 2004; Stahl *et al.*, 1983) for swarming, aside from possible shape induced physical interactions.

Listeria. Listeria is a facultative anaerobic bacterium, capable of surviving in the presence or absence of oxygen. It can grow and reproduce inside the host cell. Outside the body, Listeria use flagella for swimming, but at body temperature flagellin production is turned off, and Listeria hijack the actin cytoskeleton of the cell for its mobility. By expressing actin promotors on their surface, a thick actin gel develops on the surface. The gel formes a comet and pushes the bacterium through the cell.

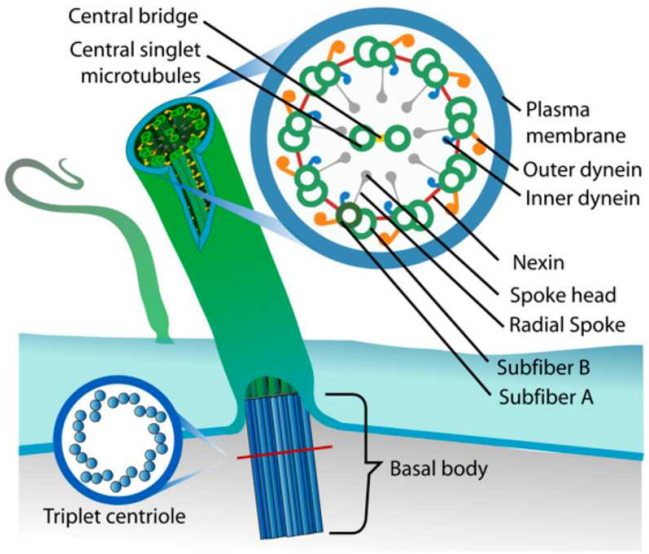

FIG. 4 The axoneme consists of nine double microtubules, arranged around the perimeter, and two central microtubules. The microtubules are connected by many linker proteins. Motor proteins connecting neighboring double microtubules lead to active bending. From `http://en.wikipedia.org/wiki/Cilium`.

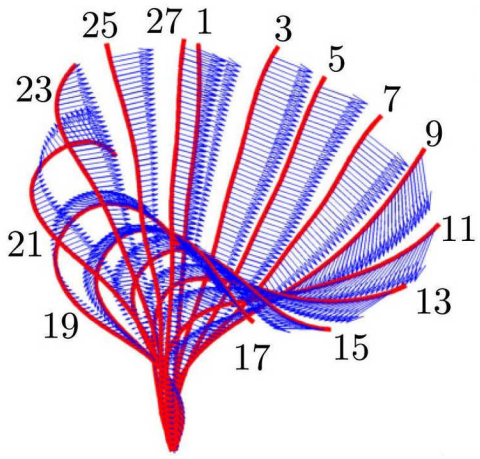

FIG. 5 The beat of cilia has two distinct phases, the power stroke and the recovery stroke. Snapshots are shown from Volvox somatic cells, imaged at 1000 frames per second. During the power stroke, the cilium is stretched out straight and moves rather fast in one direction (frames 1 - 11), while during the recovery stroke, it bends and slowly retracts (frames 13-27). Adapted from Brumley *et al.* (2014).

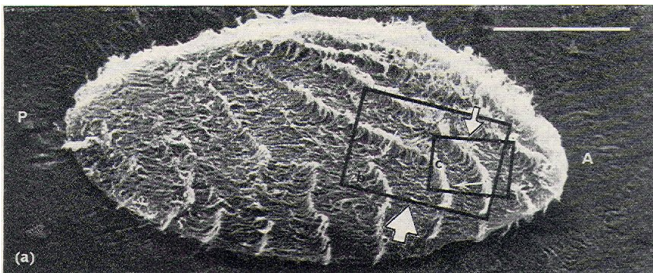

FIG. 6 The surface of *Opalina* is covered by many hairlike filaments called cilia. *Opalina* swims forward by a stroke-like wiggling of the cilia. The formation of metachronal waves is clearly visible. The scale bar is $100\mu m$. From Tamm and Horridge (1970).

In vitro, this mechanism can be mimicked by micrometer-size colloid beads coated with nucleation promotion factors. The gel initially formes isotropically, but due to tension in the growing gel layer, the symmetry is broken spontaneously, and an actin comet formes (Kawska *et al.*, 2012). The physics of Listeria motility has been reviewed recently by Prost *et al.* (2008).

Eukaryotic Cells. Eucaryotic swimmers are usually propelled by cilia or (eucaryotic-)flagella. These motile hairlike extensions of the cell consist of a bundle of microtubules, which are connected by motor proteins and other connecting proteins, see Fig. 4. The underlying structure is called the axoneme. It consists of two central microtubules, which are surrounded by nine double microtubules (rather stiff filaments with a persistence length of about 1 mm). The microtubules are connected by many proteins (nexin links, central spokes, ...), which stabilize the structure. Motor proteins (dynein) connecting neighboring double microtubules cause a local active bending force by sliding the microtubules relative to each other. Thus, motor activity is spread out over the whole length of the eukaryotic flagellum. The axoneme structure is well conserved across all eukaryotes. Hence, it seems very likely that it has evolutionary already been present in the very first eukaryotic cells.

The main structural difference between *cilia* and *flagella* is their length. A typical cilium is $10\mu m$ long, while sperm flagella are about $50\mu m$ long. The second large difference concerns their beat patterns. While flagella beat with an almost perfect propagating sinusoidal bending wave, the ciliar beat has two distinct phases. During the *power stroke*, the cilium is stretched out straight and moves rather fast in one direction, while it bends, twists a little sideways and slowly retracts in the *recovery stroke*, as shown in Fig. 5. A particularly interesting feature of the beat pattern of cilia arrays is the formation of "metachronal waves", as shown in Fig. 6; the cilia do not beat synchronously, but in a pattern resembling a wheat field in the wind.

Different physical mechanisms for the beat of eukaryotic flagella and cilia have been suggested. Either the beat arises from a coupling of the activity of motor proteins with the curvature of the flagellum, where large curvature implies detachment of motors from the neighboring filament (Bayly and Wilson, 2014; Lindemann, 1994, 2014; Lindemann and Lesich, 2010), or it arises from the

cooperative behavior of several motors pulling in opposite directions, with the "winners" pulling along the "losers" for a while. This tug-of-war of the molecular motors results in a negative force-velocity relation at zero velocity. The system is thus intrinsically unstable, and starts moving in one direction. As the filaments move relative to each other and deform, elastic forces build up, eventually causing stalling and motion reversal. The system thus starts to oscillate in time. This oscillation explains how the axoneme's internal machinery self-organizes to generate the flagella beat (Camalet *et al.*, 1999; Hilfinger *et al.*, 2009; Jülicher and Prost, 1997; Riedel-Kruse *et al.*, 2007).

The domain of eukaryotes is home to an extraordinary number of different microswimmers. While all employ axonemes as motors, they use them in all kinds of ways and arrangements to propel themselves. In the following, we present a few examples of eukaryotic microswimmers, which have received particular attention in the biophysical community.

Sperm. Many sperm cells consist of a (roughly spherical) head, which comprises the genetic material, a midpiece, which contains many mitochondria for energy production, and the eukaryotic flagellum, see Fig. 7. A sperm cell is propelled though a fluid by a snake-like wiggling of its flagellum, as shown in Fig. 8. The flagellar beat is a propagating bending wave, with wave lengths smaller than the flagellar length. The beat can either be planar, as in Fig. 8, in particular for sperm swimming near surfaces (Friedrich *et al.*, 2010), or be three-dimensional with a conical envelope (Cosson *et al.*, 2003; Woolley, 2003). The purpose of sperm motility is of course the transport of the genetic material to the egg. Here, chemotaxis is important to guide the spermotozoa to find their target (Alvarez *et al.*, 2014; Eisenbach and Giojalas, 2006; Friedrich and Jülicher, 2007; Kaupp *et al.*, 2008, 2003).

Trypanosomes. Trypanosomes (*T. brucei*) are motile parasites responsible for sleeping sickness. Their motility is mediated by a single flagellum. However, unlike in sperm the flagellum of a trypanosome emerges from the flagellar pocket near the base of the cell and runs along the length of the entire body, as illustrated in Fig. 9. The cell surface hydrodynamic drag is used by trypanosomes to sweep antibodies to the flagellar pocket, the "cell mouth", for host immune evasion. Trypanosomes are pulled forward by the planar beat of the flagellum, while the asymmetrically shaped body induces also a rotational motion (Babu and Stark, 2012; Heddergott *et al.*, 2012; Uppaluri *et al.*, 2011).

Ciliates. Ciliates are a phylum of microorganisms characterized by motile cilia on their surface. Among them, *Paramecia* and *Opalina* have received significant

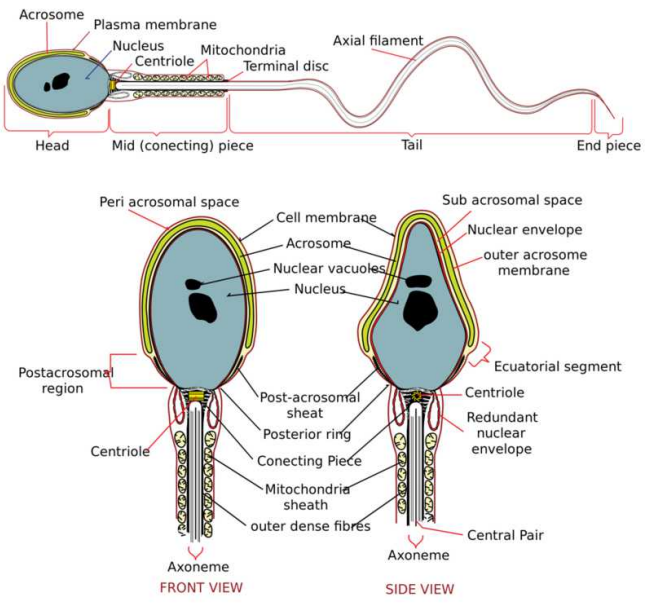

FIG. 7 Schematic presentation of the structure of human sperm. Sperm cells consist of a head 5 μm by 3 μm and a tail 41 μm long. Spermatozoa beat at $10-60$ Hz, which generates swimming velocities on the order of 100 μm/s. From `http://en.wikipedia.org/wiki/Spermatozoon`.

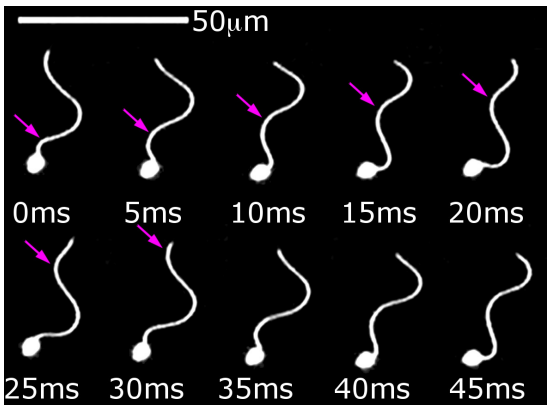

FIG. 8 Sperm swim by a snake-like motion of their flagellum. The time sequence (from left to right) of snapshots of the beat of sea-urchin sperm shows a sinusoidal traveling wave on the flagellum. Arrow indicate the wave propagation from the head to the tip. Images courtesy of J. Jikeli, L. Alvarez and U.B. Kaupp (Forschungszentrum caesar, Bonn).

attention in the biophysics community as model systems. *Paramecia* is a group of unicellular ciliate protozoa, which range from about 50 μm to 350 μm in length and move with a speed of approximately $10^3\mu$m/s (10 body lengths per second). They generally feed on bacteria and other small cells. *Opalina* is a genus of protozoa found in the intestines of frogs and toads. It is without a mouth or contractile vacuole. The surface of Opalina is covered uniformly with cilia.

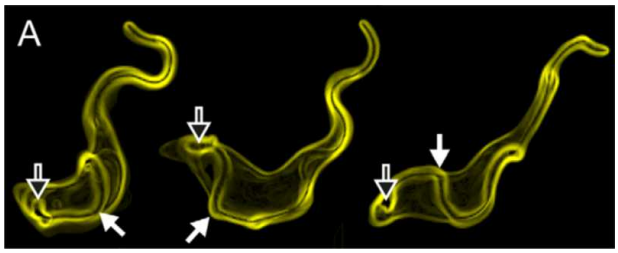

FIG. 9 Swimming motion of trypanosomes. The contour of the flagellum attached to the cell body (closed arrows) is clearly visible from the flagellar pocket (open arrows) to the anterior free end. From Heddergott *et al.* (2012).

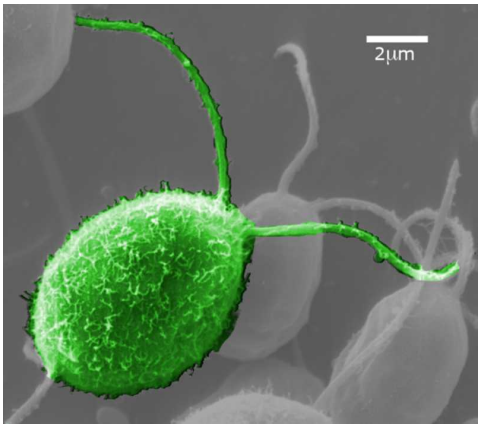

FIG. 10 *Chlamydomonas* swims by a breast-stroke-like motion of its two flagella. Steering in reaction to a light stimulus is facilitated by additional beats of one flagellum. Adapted from `http://remf.dartmouth.edu/images/algaeSEM`.

Both in *Paramecia* and *Opalina*, cilia beat neither independently nor completely synchronously, but instead (as explained above) in the form of metachronal waves (Machemer, 1972; Okamoto and Nakaoka, 1994; Tamm and Horridge, 1970), see Figs. 5 and 6.

Chlamydomonas reinhardtii. *Chlamydomonas reinhardtii* is a single-celled green algae of about 10 μm in diameter, which swims with two flagella, see Fig. 10. Chlamydomonae are equipped with a light-sensing "eye-spot". Widely distributed worldwide in soil and fresh water, *C. reinhardtii* is used as a model organism in biology in a wide range of subfields. The swimming motion of *Chlamydomonas* resembles the human breast-stroke: the flagella are pulled back in a nearly straight shape, and are then bend over and pushed forward again. The oscillatory velocity field induced by swimming *C. reinhardtii* has been observed in time-resolved measurements recently (Drescher *et al.*, 2010; Guasto *et al.*, 2010).

Volvox. Volvox is another green algae. It forms spherical colonies of up to 50,000 cells. Each mature

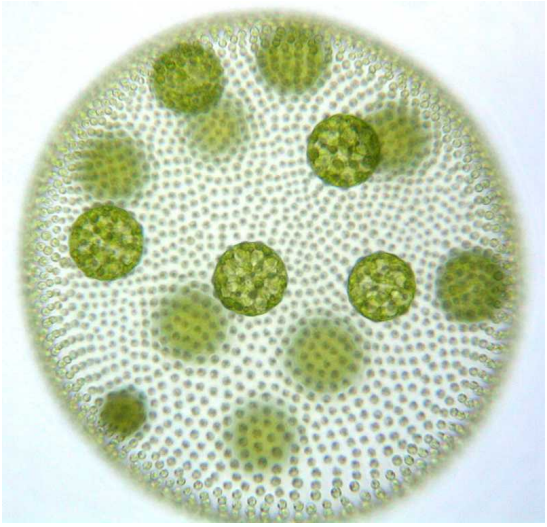

FIG. 11 Volvox carteri is a colony of several thousand cells organized around a spheroidal structure made of a gel-like extracellular matrix. The small cells are somatic cells; the larger cells visible inside the colony are the reproductive cells that will form new colonies. Each somatic cell has two flagella, which beat in a coordinated fashion to rotate and move the colony. From `http://www2.unb.ca/vip/photos.htm` (A. Nedelcu, Biology Dept., University of New Brunswick)

Volvox colony is composed of numerous flagellate cells similar to *Chlamydomonas*, embedded in the surface of a hollow sphere. The cells move their flagella in a coordinated fashion, with distinct anterior and posterior poles of the colony. Each individual cell has an eye-spot, more developed near the anterior, which enable the colony to swim towards light (Solari *et al.*, 2011). Recently, the flow field around freely swimming Volvox has been measured directly (Drescher *et al.*, 2010, 2009). The order of Volvocales contains many more microswimmers, in particular spherical swimmers of many different sizes.

Gliding Motility of Cells. Another form of cellular motility is gliding or crawling. In this case, cells do not swim in a fluid, but move on a substrate or through a gel or porous material. Because this form of locomotion on a substrate is not swimming, it goes somewhat beyond the scope of this review. However, the investigation of crawling eukaryotic cells and gliding bacteria can be a way to separate hydrodynamic contributions from generic self-propulsion effects, and provides new insights into the collective behavior of many self-propelled particles.

Crawling eukaryotic cells propel themselves with the help of their actin cytoskeleton. Velocities are of the order of a few tens of microns per hour, two to four orders of magnitude slower than swimming cells. Model organisms studied experimentally include Madin-Darby Canine Kidney (MDCK) cells, which display intriguing collective behavior (Basan *et al.*, 2013; Poujade *et al.*,

2007; Trepat *et al.*, 2009), and lymphocytes, keratocytes(Kim *et al.*, 2012) and keratinocytes for single-cell motility.

Also many bacteria can move actively by gliding on a substrate. A particularly well studied example is *myxobacteria*, which typically travel in swarms. *Myxococcus xanthus* has a signaling system that requires cell-to-cell contact, coordinates cell movements and gives rise to rippling patterns (Kaiser, 2003). It has an elongated, spherocylinder-like body with an aspect ratio of about 10. After collisions, the bacteria acquire nearly identical nematic orientation. This makes myxobacteria a very interesting model system to study the collective behavior of self-propelled rod-like particles (Gejji *et al.*, 2012; Harvey *et al.*, 2013, 2011; Peruani *et al.*, 2012).

B. Synthetic Microswimmers

Locomotion on the nanoscale through a fluid environment is one of the grand challenges confronting nanoscience today (Ozin *et al.*, 2005). The vision is to synthesize, probe, understand, and utilize a new class of motors made from nanoscale building blocks that derive on-board or off-board power from in-situ chemical reactions. The generated mechanical work allows these motors to move through a fluid phase while simultaneously or sequentially performing a series of tasks. A large variety of such swimmers have been constructed recently, from bimetallic nanorods (Fournier-Bidoz *et al.*, 2005; Ozin *et al.*, 2005; Paxton *et al.*, 2004), to rotating filaments (Manghi *et al.*, 2006), and artificial sperm (Dreyfus *et al.*, 2005; Williams *et al.*, 2014). Some examples are given below.

Bimetallic Nanorods and Microspheres. A simple class of synthetic nanoscale motors are made from bimetallic Pt-Au nanorods immersed in a H_2O_2 solution (Fournier-Bidoz *et al.*, 2005; Paxton *et al.*, 2006, 2004). The catalytic reaction $2\,H_2O_2 \rightarrow 2\,H_2O + O_2$ occurs at the Pt end of the rod and is the power source for the motion. One plausible mechanism for motion involves the surface tension gradient due to O_2 adsorption on the nonreactive Au end. The molecular-level details of how O_2 generated at the Pt end of the nanorod leads to the propulsive force remain to be elucidated.

Catalytic Janus Colloids. Similarly, spherical particles (like polystyrene or silica beads with metallic caps), which catalyze a chemical reaction inside the fluid, display self-propulsion (Erbe *et al.*, 2008; Howse *et al.*, 2007). The catalytic reaction implies an asymmetric, non-equilibrium distribution of reaction products around the colloid, which generates osmotic or other phoretic forces (Golestanian, 2009; Golestanian *et al.*, 2005; Popescu *et al.*, 2009, 2010; Rückner and Kapral, 2007; Sabass and Seifert, 2012; Thakur and Kapral, 2011). These objects are denoted "diffusio-phoretic swimmers".

The concept of diffusio-phoretic swimmers can be taken one step further by constructing self-assembled, photoactivated colloidal microswimmers. An example is a polymer sphere, which includes a smaller hematite cube in dilute H_2O_2 solution. The decomposition reaction is catalyzed by the hematite cubes, but only under illumination. Pairs of spheres and cubes then self-assemble into self-propelled microswimmers at a surface (Palacci *et al.*, 2013). The dynamic assembly results from a competition between self-propulsion of particles and an attractive interaction induced respectively by osmotic and phoretic effects activated by light.

Thermophoretic Janus Colloids. Janus colloids with a metallic cap can also display self-propulsion due to self-thermophoresis. In this case, the cap is heated by a laser beam, which generates a temperature difference between the two sides of the Janus particle; the colloid then diffuses in this temperature gradient (Jiang *et al.*, 2010). This approach has been extended to thermophoretic Janus colloids in binary fluid mixtures (with an upper miscibility gap) near the demixing critical point (Buttinoni *et al.*, 2012; Volpe *et al.*, 2011). In this case, heating by the laser beam leads to the formation of a droplet of one phase which adheres to the cap. This approach has the advantage that a small laser power suffices to induce self-propulsion.

Bubble Jets. Another type of catalytic microswimmer consists of a hollow micro-tube with functionalized surface. Such a microswimmer has been developed and fabricated by templated electrodeposition on a pre-stressed thin polymer film, which generates strain and leads to detachment from the substrate and roll-up into a tube. The catalytic reaction decomposes H_2O_2 into O_2 and water inside the tube, which leads to the formation of nano- and microbubbles. By spontaneous symmetry breaking, the bubbles leave the tube on one side; this implies a jet-like propulsion. Such tubular micro-engines offer several advantages, like easy motion control, integration of various functions, scalable size in diameter and length, and straight trajectories (Mei *et al.*, 2011; Sanchez and Pumera, 2009; Sanchez *et al.*, 2011a).

Rotators. Rotating discs (Grzybowsk *et al.*, 2000; Llopis and Pagonabarraga, 2008), rotating spheres or dumbbells (Tierno *et al.*, 2008) are another important class of swimmers. These rotators can be autonomous swimmers, like the Volvox algae mentioned above, or actuated synthetic particles, like super-paramagnetic particles rotated by an external magnetic field (Bleil

et al., 2006). Rotators show an interesting collective behavior, like a circling motion of Volvox around each other (Drescher *et al.*, 2009), or a lane formation of rotating magnetic discs in microfluidic channels (Götze and Gompper, 2010, 2011).

Self-propelled Droplets. Aqueous droplets suspended in an oil phase containing surfactants can also be made to swim. Propulsion arises for example due to the spontaneous bromination of mono-olein as the surfactant. The droplet surface is covered by a dense surfactant monolayer, which reacts with the bromine fuel that is supplied from inside the droplet, such that bromination proceeds mainly at the droplet surface, and reduces the amphiphilicity of the surfactant. This results in a self-sustained bromination gradient along the drop surface, which propels the droplet due to Marangoni stresses (Thutupalli *et al.*, 2011).

Biomimetic Microswimmers.

Artifical microswimmers can be constructed by using similar design principles as those found in biological systems. A by now classical example is a swimmer which mimics the propulsion mechanism of a sperm cell (Dreyfus *et al.*, 2005). The flagellum is constructed from a chain of magnetic colloid particles and is attached to a red blood cell, which mimics the sperm head. This artificial swimmer is set into motion by an alterating magnetic field, which generates a sidewise oscillatory deflection of the flagellum. However, the swimming motion is not the same as for a real sperm cell; the wiggling motion is more a wagging than a travelling sine wave, and generates a swimming motion toward the tail end, opposite to the swimming direction of sperm.

A more recent example of a biohybrid swimmer which mimics the motion of sperm has been presented by Williams *et al.* (2014). In this case, the microswimmer consists of a polydimethylsiloxane filament with a short, rigid head and a long, slender tail on which cardiomyocytes (heart-muscle cells) are selectively cultured. The cardiomyocytes contract periodically and deform the filament to propel the swimmer. This is a true microswimmer because it requires no external force fields. The swimmer is about 50 μm long and reaches a swimming velocity up to 10 $\mu m/s$.

Another interesting example is artificial cilia (Sanchez *et al.*, 2011b). The assembly of oscillatory active filament bundles requires three main components. The first two, kinesin motor clusters and microtubules, spontaneously organize into aster-like structures (Nédélec *et al.*, 1997). Addition of a third component, a non-adsorbing polymer, induces attractive interactions between microtubules through the depletion mechanism, leading to their bundling. This greatly increases the probability of kinesin clusters to simultaneously bind and walk along neighboring microtubules, where the relative motion

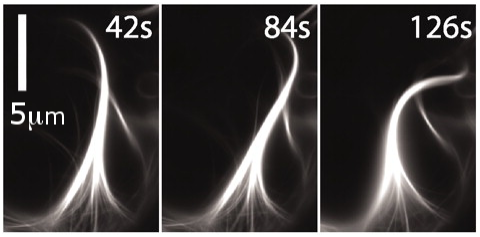

FIG. 12 A minimal system of microtubules, molecular motors, and depleting polymer assembles into actively beating bundles. The sequence of images illustrates the beating pattern. From Sanchez *et al.* (2011b).

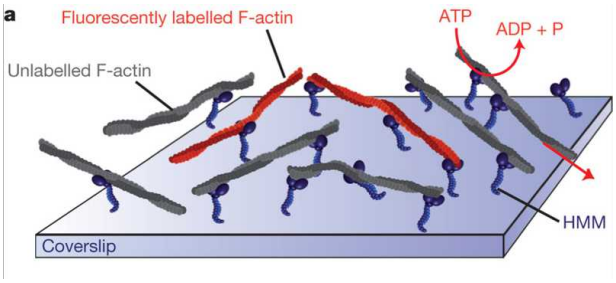

FIG. 13 Motility assays consist of carpets of motor proteins, on which polar filaments like actin are propelled along their contour. From Schaller *et al.* (2010).

of microtubules in these bundles depends on their polarity. This generates a cilia-like beat pattern, which is, however, symmetric in its forward and backward motions (Sanchez *et al.*, 2011b), see Fig. 12.

Motility Assays. An in-vitro system to study the interaction of motor proteins with biological polar filaments like actin and microtubules are motility assays. In these systems, motor proteins are grafted onto a planar substrate with their active heads pointing upwards. Polar filaments, which are lying on such a motor-protein carpet, attach to the motors and are pushed forward, see Fig. 13. The filaments in such a system are neither swimmers nor self-propelled particles, but it is nevertheless a interesting model systems to study the collective behavior of many moving particles with self-organized directions of motion, which shows phenomena like density waves and vortices (Schaller *et al.*, 2010; Sumino *et al.*, 2012).

C. Theoretical Model Microswimmers

Several detailed theoretical models have been designed during the last decades to describe and understand the behavior of flagellated microswimmers, but also of diffusio-phoretic spheres and rods, etc. These models and their properties will be reviewed in detail in the remainder of this article. However, there are also some model swimmers, which serve as generic models to

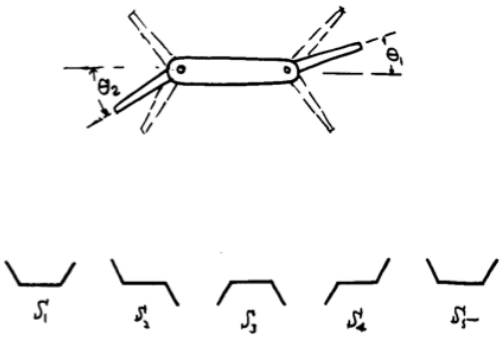

FIG. 14 The Purcell swimmer consists of three rod-like connected segments, which can be tilted with respect to each other. When the two angles θ_1 and θ_2 are varied in the non-reciprocal temporal sequence shown at the bottom, this micro-machine moves forward. From Purcell (1977).

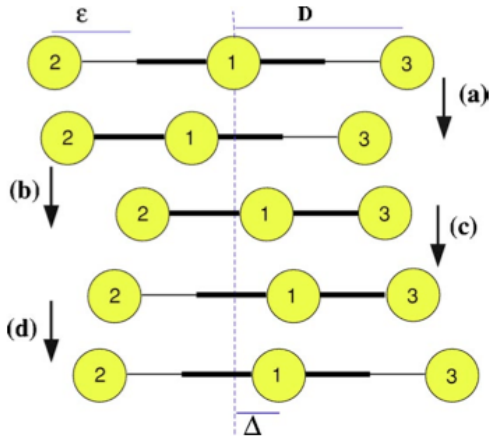

FIG. 15 Three connected beads swim forward when their distances are varied cyclically as a function of time. Here, it is important that the cycle breaks time-reversal symmetry, as shown. In one cycle, the swimmer moves by a distance Δ. From Najafi and Golestanian (2004).

elucidate the physical principles of microswimmers. The latter models are briefly introduced here.

Purcell Swimmer. It was recognized already more than 30 years ago by Purcell (1977) that directed forward swimming of micromachines in viscous fluids—at low Reynolds numbers, see Sec. II below—is not possible when the angle between *two* rigid segments is varied periodically in time. Therefore, Purcell suggested a swimmer consisting of *three* rigid segments as shown in Fig. 14. When the two angles are varied periodically in time, but in a way which breaks time-reversal symmetry, as shown at the bottom of Fig. 14, this machine performs a directed motion (Purcell, 1977).

Three-Bead Swimmer. A very simple one-dimensional swimmer can be constructed from three spheres that are linked by rigid rods, whose lengths can change between two values (Najafi and Golestanian, 2004). With a periodic motion that breaks the time-reversal symmetry as well as the translational symmetry, the model device swims at low Reynolds number as shown in Fig. 15. This swimmer is similar in spirit to the Purcell swimmer, but has the advantage that it can be treated theoretically much more easily, so that many of its properties can be analyzed in detail or even calculated analytically (Alexander *et al.*, 2008; Golestanian, 2008; Najafi and Golestanian, 2004).

Squirmers. A particular class of microswimmers are almost spherical organisms that are propelled by active hair-like organelles (cilia) covering the body. On a mesoscopic length scale, the synchronized beating of the cilia can be mapped onto a spherical envelope (Blake, 1971b; Lighthill, 1952), and its time average corresponds to a steady tangential surface velocity. These objects—called "squirmers"—may also serve as a simple generic model for other types of microswimmers, for example the self-propelled droplets mentioned above (Thutupalli *et al.*, 2011).

The squirmer is modeled as a hard sphere of radius R with a prescribed tangential surface velocity $\boldsymbol{v}_{\rm sq}$, causing a propulsion in the direction of the squirmer's instantaneous orientation $\hat{\boldsymbol{e}}$. The relative velocity at a surface point $\boldsymbol{r}_{\rm s}$ (with respect to the squirmer's center) is given by (Blake, 1971b)

$$\boldsymbol{v}_{\rm sq}(\boldsymbol{r}_{\rm s},\hat{\boldsymbol{e}}) = \sum_{n=1}^{\infty} B_n \frac{2}{n(n+1)} \left(\frac{\hat{\boldsymbol{e}}\cdot\boldsymbol{r}_{\rm s}}{R}\frac{\boldsymbol{r}_{\rm s}}{R} - \hat{\boldsymbol{e}} \right) P_n'\left(\frac{\hat{\boldsymbol{e}}\cdot\boldsymbol{r}_{\rm s}}{R} \right), \tag{1}$$

where $P_n'(\cos\theta)$ is the derivative of the nth Legendre polynomial with respect to the argument and B_n is the amplitude of the nth mode of the surface velocity. The absolute local surface velocity of the squirmer is given by

$$\boldsymbol{v}_{\rm s}(\boldsymbol{r}-\boldsymbol{r}_{\rm c},\hat{\boldsymbol{e}}) = \boldsymbol{v}_{\rm c} + \boldsymbol{v}_{\rm sq}(\boldsymbol{r}-\boldsymbol{r}_{\rm c},\hat{\boldsymbol{e}}) + \boldsymbol{\Omega}\times(\boldsymbol{r}-\boldsymbol{r}_{\rm c}), \tag{2}$$

where $\boldsymbol{r}_{\rm c}$, $\boldsymbol{v}_{\rm c}$ and $\boldsymbol{\Omega}$ are the sphere position, velocity and angular velocity, respectively. The constant B_1 sets the average velocity of the squirmer, $v = \langle \hat{\boldsymbol{e}}\cdot\boldsymbol{v}_{\rm s}\rangle = 2B_1/3$ (Ishikawa *et al.*, 2006). To cope with the biodiversity of real microswimmers, the characteristic surface velocity of the model can be varied by adjusting the coefficients B_n with $n \geq 2$. In most cases studied so far, only B_1 and B_2 are taken to be non-zero, so that $B_n = 0$ for $n \geq 3$.

This model was employed, for example, to study the hydrodynamic interaction of two squirmers without (Ishikawa *et al.*, 2007) and with (Götze and Gompper, 2010) thermal fluctuations, monolayers of squirmers without thermal fluctuations (Ishikawa and Pedley, 2008), or their behavior in external flows (Gachelin *et al.*, 2013b; Pagonabarraga and Llopis, 2013; Zöttl and Stark, 2012, 2013).

II. LIFE AT LOW REYNOLDS NUMBERS

A. Hydrodynamics

The dynamics of the incompressible fluid surrounding a microswimmers is described by the Navier-Stokes equations

$$\nabla \cdot \boldsymbol{v} = 0, \tag{3}$$

$$\rho \left(\frac{\partial \boldsymbol{v}}{\partial t} + (\boldsymbol{v} \cdot \nabla)\boldsymbol{v} \right) = \eta \nabla^2 \boldsymbol{v} - \nabla p + \boldsymbol{f}, \tag{4}$$

where ρ is the fluid density, η the fluid viscosity, $\boldsymbol{v}(\boldsymbol{r},t)$ the position- and time-dependent fluid velocity field, $p(\boldsymbol{r},t)$ the pressure field, and $\boldsymbol{f}(\boldsymbol{r},t)$ an applied body force. Scaling length, velocity, and time by characteristic values L, v_0, and T_0, respectively, yields

$$Re_T \frac{\partial \boldsymbol{v}'}{\partial t'} + Re(\boldsymbol{v}' \cdot \nabla)\boldsymbol{v}' = \nabla^2 \boldsymbol{v}' - \nabla p' + \boldsymbol{f}', \tag{5}$$

where the prime denotes dimensionless quantities. Here, the dimensionless number $Re = \rho v_0 L/\eta$ is the classical Reynolds number, which is a measure of the importance of the nonlinear advection term compared to the viscous forces. A second dimensionless number is the oscillatory Reynolds number $Re_T = \rho L^2/(\eta T_0)$. It indicates the importance of the linear unsteady term, which scales as $\rho v_0/T_0$, compared to the viscous term (Dhont, 1996; Lauga, 2011; Lauga and Powers, 2009). $Re_T = \tau_\eta/T_0$ is the ratio of the viscous time scale $\tau_\eta = \rho L^2/\eta$ for shear wave propagation over the distance L and the characteristic time T_0. Examples for T_0 could be the self advection time L/v_0 (for which $Re_T = Re$), the rotational period of a bacterial flagellum, or the period of a beating cycle of a cilia. For a swimmer of length $L = 10\mu$m and a velocity of $v_0 = 50\mu$m/s, the Reynolds number in water (with the kinematic viscosity $\nu = \eta/\rho = 10^{-6}\mathrm{m}^2/\mathrm{s}$) is $Re \approx 10^{-3}$. In this case, the nonlinear contributions on the left-hand-side of Eq. (5) can be neglected, leading to the linearized Navier-Stokes equation

$$\rho \frac{\partial \boldsymbol{v}}{\partial t} = \eta \nabla^2 \boldsymbol{v} - \nabla p + \boldsymbol{f}. \tag{6}$$

For $Re_T \ll 1$, i.e., $\tau_\eta \ll T_0$, equation (6) turns into the Stokes equation (creeping flow),

$$\nabla p - \eta \nabla^2 \boldsymbol{v} = \boldsymbol{f} \tag{7}$$

and all inertia terms are absent.

The Stokes equation (7) is linear and time-independent, and is thus symmetric under time reversal, an aspects with far reaching consequences for microswimmers undergoing periodic shape changes, as first realized by Purcell (1977). This is expressed by the famous "scallop theorem", which can be stated as: if the shape changes displayed by a swimmer are identical when viewed in reverse order, it will generate an oscillatory, but no directed motion (Lauga, 2011; Lauga and Powers, 2009; Purcell, 1977). It means that just by opening and closing its two shells, a mussel (scallop) cannot move forward. Additional degrees of freedom are required to generate a sequence of moves, which are not time reversibel. These aspect is discussed in more detail in Sec. V below.

B. Solution of Stokes Equation

The linearized Navier-Stokes equations (3), (6), and (7), can be solved analytically for an unbounded system with a external force field $\boldsymbol{f}(\boldsymbol{r},t)$. In this case, the velocity field is given by

$$\boldsymbol{v}(\boldsymbol{r},t) = \int_0^t \int \mathbf{H}(\boldsymbol{r}-\boldsymbol{r}', t-t') \cdot \boldsymbol{f}(\boldsymbol{r}',t')\, d^3r' dt', \tag{8}$$

with the time- and position-dependent hydrodynamic tensor $\mathbf{H}(\boldsymbol{r},t)$ (Bedeaux and Mazur, 1974; Español *et al.*, 1995). An explicit expression for the tensor $\mathbf{H}(\boldsymbol{r},t)$ has been provided by Español *et al.* (1995), Huang *et al.* (2012, 2013), and Theers and Winkler (2013). The creeping flow limit, i.e., the solution of Eqs. (3) and (7), follows when $\boldsymbol{f}(\boldsymbol{r},t)$ change significantly slower with time than $\mathbf{H}(\boldsymbol{r},t)$. With time-independent $\boldsymbol{f}(\boldsymbol{r})$, integration over t' in Eq. (8) yields

$$\boldsymbol{v}(\boldsymbol{r}) = \int \mathbf{H}(\boldsymbol{r}-\boldsymbol{r}') \cdot \boldsymbol{f}(\boldsymbol{r}')\; d^3r'. \tag{9}$$

$\mathbf{H}(\boldsymbol{r})$ is the well-know Oseen tensor, with the Cartesian components (Dhont, 1996; Español *et al.*, 1995)

$$H_{\alpha\beta}(\boldsymbol{r}) = \frac{1}{8\pi\eta r}\left[\delta_{\alpha\beta} + \frac{r_\alpha r_\beta}{r^2}\right]; \tag{10}$$

$\alpha, \beta \in \{x, y, z\}$ and $r = |\boldsymbol{r}|$. The Oseen tensor, also denoted as Stokeslet, shows that hydrodynamic interactions are long range, with a $1/r$ decay like the Coulomb potential. The Oseen tensor is the Green's function of the Stokes equation (7), which is easily seen, when the point force $\boldsymbol{f}(\boldsymbol{r}) = \delta(\boldsymbol{r})\hat{\boldsymbol{e}}$ (where $\hat{\boldsymbol{e}}$ is a unit vector) in the direction $\hat{\boldsymbol{e}}$ is employed. Then, Eq. (9) yields

$$\boldsymbol{v}(\boldsymbol{r}) = \frac{1}{8\pi\eta r}\left[\hat{\boldsymbol{e}} + \frac{(\boldsymbol{r}\cdot\hat{\boldsymbol{e}})\boldsymbol{r}}{r^2}\right]. \tag{11}$$

The presence of confining surfaces modifies the fluid flow field. At surfaces, the fluid velocity is typically very small, because the collisions of fluid particles with the surface imply that the molecules are scattered backwards and thereby transfer momentum parallel to the wall. Thus, no-slip boundary conditions, with $\boldsymbol{v}(\boldsymbol{r}) = 0$ at the surface, are usually employed. The solution of Stokes equations is still given by Eq. (9), however the Ossen tensor has to be replaced by the Blake tensor (Blake, 1971a), which satisfies the no-slip boundary condition.

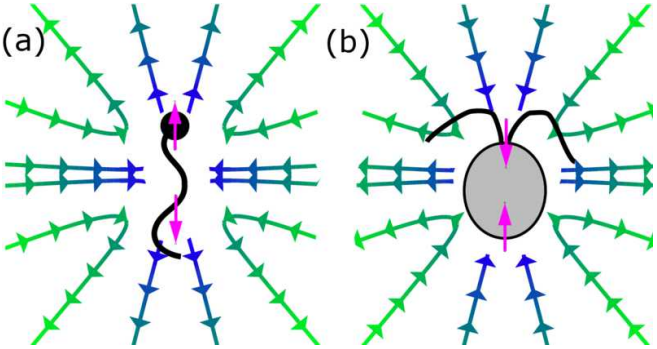

FIG. 16 Schematics of the flow field dipole swimmers, (a) pusher and (b) puller.

C. Dipole Swimmers

Most swimmers move autonomously, with no external force applied, and hence the total interaction force of the swimmer on the fluid, and *vice versa*, vanishes. In the simplest case, which actually applies to many microswimmers like bacteria, spermatozoa, or algae, the far-field hydrodynamics (at distances from the swimmer much larger than its size) can well be described by a force dipole (Ishikawa, 2009; Lauga and Powers, 2009). This has been confirmed experimentally for *E. coli* by Drescher *et al.* (2011). Two classes of such dipole swimmers can be distinguished, as shown schematically in Fig. 16. If the swimmer has its "motor" in the back, and the passive body drags along the surrounding fluid in front, the characteristic flow field of a "pusher" emerges, see Fig. 16(a). Similarly, if the swimmer has its "motor" in the front, and the passive body drags along the surrounding fluid behind, the characteristic flow field of a "puller" develops, see Fig. 16(b). It is important to notice that the flow fields of pushers and pullers look similar, but with opposite flow directions. This has important consequences for the interactions between swimmers and of swimmers with walls, as will be explained below.

Mathematically, the flow field $\boldsymbol{u}_d(\boldsymbol{r}-\boldsymbol{r}_0)$ of a hydrodynamic force dipole located at $\boldsymbol{r}_0$ can be obtained very easily from the Oseen tensor (10) by considering two opposite forces $\boldsymbol{f}_0 = f_0\hat{\boldsymbol{e}}$ of equal magnitude at $\boldsymbol{r} = \boldsymbol{r}_0 \pm \boldsymbol{d}/2$ with $\boldsymbol{d} = d\hat{\boldsymbol{e}}$. An expansion to leading order in $\boldsymbol{d}/|\boldsymbol{r}-\boldsymbol{r}_0|$ yields

$$\boldsymbol{u}_d(\boldsymbol{r}) = \frac{P}{8\pi\eta r^3}\left[-1+3\frac{(\boldsymbol{r}\cdot\hat{\boldsymbol{e}})^2}{r^2}\right]\boldsymbol{r}, \qquad (12)$$

where $P = f_0 d$ is the dipole strength. Note that the flow field of a force dipole decays as $1/r^2$ from the center of the dipole, faster than the force monopole or Stokeslet, see Eq. (10). The flow lines of a hydrodynamic dipole oriented in the x-direction are shown in Fig. 17. There are two inflow and two outflow regions in the xy-projection, which are separated by the separatrices $y = \pm\sqrt{2}x$. In three dimensions, the outflow region is a cone.

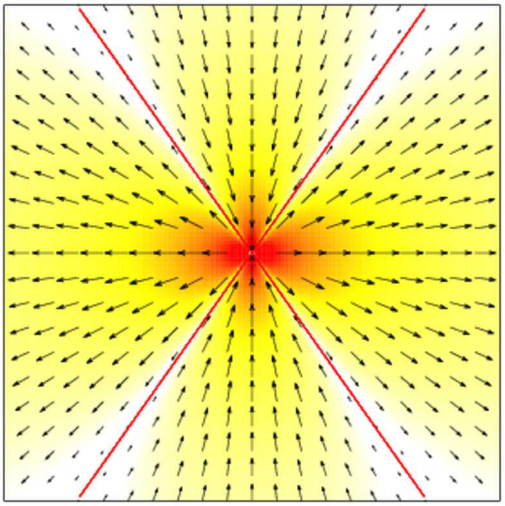

FIG. 17 Flow lines in the far-field of a hydrodynamic dipole along the horizontal direction, as given by Eq. (12). The separatrices between the inflow and outflow regions are shown by thick red lines.

The flow field of a hydrodynamic dipole in front of a surface can be obtained by the image method known from electrostatics. Considering, for simplicity, a planar wall with slip boundary conditions. The flow field is then given by

$$\boldsymbol{v}_w(\boldsymbol{r}-\boldsymbol{r}_0) = \boldsymbol{u}_d(\boldsymbol{r}-\mathbf{r}_0;\hat{e}) + \boldsymbol{u}_d(\mathbf{r}-\boldsymbol{r}_1;\hat{\boldsymbol{e}}') \qquad (13)$$

for a wall at $z = 0$, with $\boldsymbol{r}_0 = (x_0, y_0, z_0)$, $\boldsymbol{r}_1 = (x_0, y_0, -z_0)$, where $z_0 > 0$, and $\hat{\boldsymbol{e}}'$ the mirror image of $\hat{\boldsymbol{e}}$ with respect to the $z = 0$ plane. This implies that at $z = 0$ the velocity field $v_{w,z}$ perpendicular to the surface vanishes identically, i.e., $v_{w,z}(z = 0) \equiv 0$. The dipole experiences a force near the surface, which is determined by the hydrodynamic interactions between the dipole and its image. It is given by the z-component of the flow field of the image charge at the location of the dipole, thus

$$v_{w,z}(z_0) = -\frac{P}{32\pi\eta z_0^2}\left[1-3(\hat{\boldsymbol{e}}\cdot\hat{\boldsymbol{e}}_z)^2\right], \qquad (14)$$

because $(\hat{\boldsymbol{e}}'\cdot\hat{\boldsymbol{e}}_z)^2 = (\hat{\boldsymbol{e}}\cdot\hat{\boldsymbol{e}}_z)^2$. This result shows that the hydrodynamic force is attractive to the wall, and that it decays as the dipole flow field quadratic with the distance from the wall. The exact solution for a no-slip wall (Berke *et al.*, 2008) yields the same functional dependence on the angle and the wall distance as Eq. (14), only the numerical prefactor in Eq. (14) is smaller by a factor 2/3.

D. Fluctuations and Noise

Fluctuations and noise may strongly affect the motion of microswimmers. There are two major sources of noise

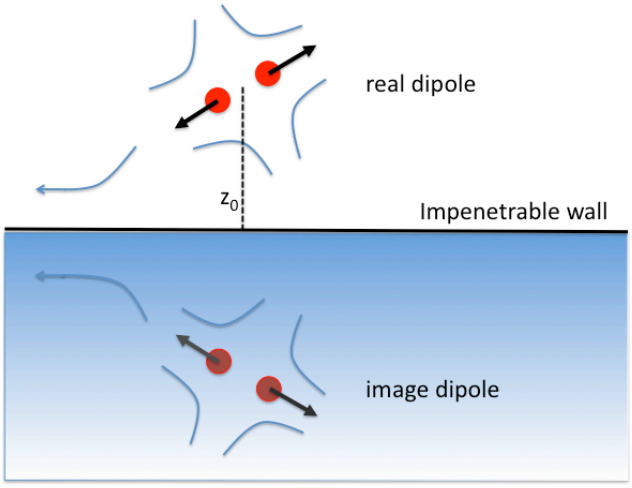

FIG. 18 Schematic representation of a dipole swimmer (pusher) near a wall. An image dipole gives the correct boundary conditions (impenetrability) at the slip wall.

in active systems. On the one hand, thermal fluctuations are present in both passive and active systems. On the other hand, active processes themselves can give rise to fluctuations. For example, in cilia beating, the motor proteins are sensitive to the availability of ATP molecules, their number attached to a filament varies in time, and different cilia will typically have different numbers of active motors. Furthermore, the smaller a system is, the more important fluctuations become.

The importance of noise for the dynamics of microswimmers can be estimated by the Péclet number Pe, which compares advective and diffusive time scales. The self-advection time scale is L/v_0, where v_0 and L are the typical swimmer velocity and length, respectively, and the diffusive time scale is L^2/D_T, with the translational diffusion coefficient D_T. Hence, a Péclet number can by defined by $Pe = v_0 L/D_T$. For motion in thermal equilibrium and under the assumption of the swimmer to be spherical, D_T can be related to the rotational diffusion coefficient D_R via $D_T = D_R L^2/3$. Thus, the Péclet number is equivalently given by

$$Pe = \frac{v_0}{L D_R}. \tag{15}$$

For the dynamics of a self-propelled sphere, we consider the persistent motion of a Brownian particle with independent stochastic processes for its velocity and acceleration. Hence, the equation of motion for translation is

$$\dot{\boldsymbol{r}} = \boldsymbol{v} + \frac{1}{\gamma_T}\boldsymbol{\Gamma}, \tag{16}$$

which is coupled to changes of the velocity described by

$$\dot{\boldsymbol{v}} = -\gamma_R \boldsymbol{v} + \boldsymbol{\xi}. \tag{17}$$

Strictly speaking, in this description the magnitude of the velocity is not preserved, only the relation $\langle \boldsymbol{v}^2 \rangle = v_0^2$ applies. In Eqs. (16) and (17), γ_T and γ_R are the translational and rotational friction coefficients, where the latter is related to the rotational relaxation time τ_R by $\tau_R = 1/\gamma_R = 1/((d-1)D_R)$. $\boldsymbol{\Gamma}$ and $\boldsymbol{\xi}$ are Gaussian and Markovian stochastic processes, with zero mean and the moments

$$\langle \boldsymbol{\Gamma}(t) \cdot \boldsymbol{\Gamma}(t') \rangle = 2d\gamma_T^2 D_T \delta(t-t'), \tag{18}$$

$$\langle \boldsymbol{\xi}(t) \cdot \boldsymbol{\xi}(t') \rangle = 2(d-1) D_R v_0^2 \delta(t-t') \tag{19}$$

in $d > 1$ dimensions. Equations (16) – (19) yield the mean square displacement of the sphere center (Risken, 1989; Uhlenbeck and Ornstein, 1930)

$$\begin{aligned} \Delta \boldsymbol{r}^2 &= \langle (\boldsymbol{r}(t) - \boldsymbol{r}(0))^2 \rangle \\ &= 2dD_T t + 2\tau_R^2 v_0^2 \left[t/\tau_R + \exp(-t/\tau_R) - 1 \right], \end{aligned} \tag{20}$$

which implies $\Delta \boldsymbol{r}^2 = 2dD_T t + v_0^2 t^2$ for $t \ll \tau_R$ and $\Delta \boldsymbol{r}^2 = (2dD_T + 2v_0^2/[(d-1)D_R]t$ for $t \gg \tau_R$. The latter defines the effective translational diffusion coefficient

$$D_{T,eff} = D_T + v_0^2/[d(d-1)D_R], \tag{21}$$

which is much larger than D_T for $v_0 \gg \sqrt{D_T D_R}$. Note that for a sphere embedded in three-dimensional space, but confined in its translational motion to two dimensions, e.g., to a surface, the effective diffusion coefficient still has the same effective diffusion constant (21) with $d = 3$, but $\Delta \boldsymbol{r}^2 = 4D_{T,eff} t$. In particular, these results show that the Péclet number (15), which involves the rotational diffusion constant, remains appropriate to characterize the importance of noise for self-propelled particles.

The mean square displacement of self-propelled Janus-colloids on a surface has been measured as a function of fuel concentration by Howse *et al.* (2007) as well as by Volpe *et al.* (2011) for various illumination intensities. The extracted effective diffusion coefficients are well described by $D_{T,eff}$ of Eq. (21), indicating that diffusion is dominated by self-propulsion and rotational diffusion. The relevance of higher moments of the displacement distribution has been addressed by Zheng *et al.* (2013). In particular, a non-Gaussian character of the diffusiophoretic motion of self-propelled Janus spheres is theoretically predicted and experimentally confirmed.

For active systems, in general, fluctuations have no reason to be thermal (see Eqs. (18), (19)). While a Gaussian distribution of the noise is still a reasonable first order approximation, the amplitude can be much larger than that due to thermal fluctuations. An instructive example is the *E. coli* rotary motor. A motor rotation is typically driven by protons that generate torque by passing into the cell via the motor (Mora *et al.*, 2009). However, the flux of protons is not continuous, but rather determined by discrete events of proton translocation. The

stochasticity of this process creates a "shot noise". Modelling the motor in some detail, Mora *et al.* (2009) derive an expression for the effective diffusion coefficient of the flagellar rotation. At high load, the effective diffusion coefficient is thermal, but at low loads, diffusion increases and becomes dominated by the shot noise.

Measurements of the rotational diffusion coefficient of *Chlamydomonas* yield $D_R = 0.4\text{rad}^2/\text{s}$ (Drescher *et al.*, 2011). This value can be compared with that of a passive sphere of radius $R = 5\mu\text{m}$, which is $D_R = k_BT/(8\pi\eta R^3) \approx 3\times10^{-3}\text{rad}^2/\text{s}$, i.e., it is about two orders of magnitude smaller than the value of the active microorganism.

Similarly, for *E. coli* the values $D_R = 0.057\text{rad}^2/\text{s}$ (Drescher *et al.*, 2011) and $D_R \approx 2\text{rad}^2/\text{s}$ (Saragosti *et al.*, 2012) have been reported for non-tumbling and tumbling cells, respectively. A study of paralyzed *E. coli* (Tavaddod *et al.*, 2011) yields the rotational diffusion coefficient $D_R = 0.032\text{rad}^2/\text{s}$, which is only a factor two smaller than the value of swimming but non-tumbling cells. Thus, tumbling events evidently increase the rotational diffusion coefficient by more than an order of magnitude.

We conclude that noise and fluctuations in microswimmer motion can be much pronounced compared to that of the dynamics of respective passive objects, and that activity-based noise can be the dominant contribution to observed phenomena.

III. SWIMMING DUE TO FLAGELLAR MOTION

A. Anisotropic Hydrodynamic Friction of Slender Bodies

A microorganism is able to swim forward in a fluid by wiggling or rotating a flagellum, because the hydrodynamic friction of a long, slender body in a viscous environment is *anisotropic*. This can be demonstrated easily for a long and thin rod of radius a and length L: it experiences less friction when pulled along its axis than perpendicular to it.

We approximate the rod as a sequence of touching beads of radius a. In general, the equation of motion of the *i-th* bead is given by (Bird *et al.*, 1987; Winkler, 2007)

$$\zeta\left(\dot{\boldsymbol{r}}_i - \boldsymbol{v}(\boldsymbol{r}_i)\right) = \boldsymbol{F}_i, \tag{22}$$

i.e., the frictional force is equal to the applied force. Here, $\zeta = 6\pi\eta a$ is Stokes friction coefficient for a sphere with no-slip boundary conditions moving in a viscous fluid. The fluid velocity $\boldsymbol{v}(\boldsymbol{r}_i)$ is determined by the motion of all other beads $j \neq i$ and follows from Eq. (9). The force density on the fluid originates from the forces of the various beads

$$\boldsymbol{f}(\boldsymbol{r}) = \sum_i \boldsymbol{F}_i \delta(\boldsymbol{r} - \boldsymbol{r}_i(t)). \tag{23}$$

Thus, we obtain (Doi and Edwards, 1986)

$$\dot{\boldsymbol{r}}_i(t) = \frac{1}{\zeta}\boldsymbol{F}_i + \sum_{j\neq i} \mathbf{H}(\boldsymbol{r}_i(t) - \boldsymbol{r}_j(t)) \cdot \boldsymbol{F}_j, \tag{24}$$

which turns into (Harnau *et al.*, 1996)

$$\dot{\boldsymbol{r}}(s,t) = \frac{1}{3\pi\eta}\boldsymbol{f}(s) + \int \mathbf{H}(\boldsymbol{r}(s,t) - \boldsymbol{r}(s',t)) \cdot \boldsymbol{f}(s')\, ds' \tag{25}$$

in the continuum limit, where s (with $-L/2 < s < L/2$) is the contour coordinate along the centerline of the rod, and $\boldsymbol{f}(s)$ the linear force density.

The anisotropic friction coefficients of a rod are defined by the force-velocity relation

$$\boldsymbol{F} = \zeta_\parallel \boldsymbol{v}_\parallel + \zeta_\perp \boldsymbol{v}_\perp \tag{26}$$

for the motion parallel ($\boldsymbol{v}_\parallel$) and perpendicular ($\boldsymbol{v}_\perp$) to the rod axis. Calculations based on Eq. (26), with constant friction coefficients $\zeta_\parallel$ and $\zeta_\perp$, are denoted "resistive-force theory" (Gray and Hancock, 1955; Lighthill, 1976).

To calculate $\zeta_\parallel$ and $\zeta_\perp$, it is easiest to consider the special cases of a rod aligned along the x-axis of the reference frame and pulled parallel and perpendicular to its long axis, respectively, with the constant force $\boldsymbol{F} = F\hat{\boldsymbol{e}}$. Since, we consider a rigid body, the force density is $\boldsymbol{f}(s) = F\hat{\boldsymbol{e}}/L$, and the average rod velocity $\boldsymbol{v}_{rod} = \int \dot{\boldsymbol{r}}(s)ds/L$ becomes

$$\boldsymbol{v}_{rod} = F\left[\frac{\hat{\boldsymbol{e}}}{3\pi\eta L} + \frac{(\hat{\boldsymbol{e}} + (\hat{\boldsymbol{e}}_x\cdot\hat{\boldsymbol{e}})\hat{\boldsymbol{e}}_x)}{4\pi\eta L^2}\int_{2a}^{L}\frac{L-s}{s}\,ds\right]. \tag{27}$$

The lower cutoff of the integral excludes a region of the thickness of the rod and prevents self-interactions. Because $(\hat{\boldsymbol{e}}_x\cdot\hat{\boldsymbol{e}})\hat{\boldsymbol{e}}_x = 1$ and 0 for parallel and perpendicular orientation of the force, respectively, evaluation of the integral yields

$$\zeta_\perp = 2\zeta_\parallel\ , \qquad \zeta_\perp = \frac{4\pi\eta L}{\ln(L/2a)} \tag{28}$$

in the asymptotic limit of a long rod (Doi and Edwards, 1986). It is therefore easier to pull a long rod along its axis than perpendicular to it by a factor two. The logarithmic divergence is a result of the long-range nature of hydrodynamic interactions of different parts of the rod, which *reduce* the friction coefficient compared to that of a rod of non-interacting beads ($\sim L$). Corrections of the friction coefficients for a more precise hydrodynamic calculation for a cylinder are provided in Tirado *et al.* (1984) and Howard (2001).

B. Swimming Velocity of Beating Flagella and Sperm

The result (28) together with Eq. (26) can now be used to calculate the swimming velocity of a sinusoidally beating flagellum. In this case, the time-dependent shape is

given by

$$y(x,t) = A\sin(kx - \omega t), \tag{29}$$

where A is the beating amplitude, ω the frequency, and $k = 2\pi/\lambda$ the wave number with the wave length λ. The velocity of a segment of the flagellum at x is then

$$v_y(x,t) = \frac{\partial y}{\partial t} = -A\omega\cos(kx - \omega t), \tag{30}$$

where geometric nonlinearities are neglected. With the local tangent vector (not normalized)

$$\boldsymbol{t}(x,t) = (1, Ak\cos(kx - \omega t), 0)^T, \tag{31}$$

the velocity $\boldsymbol{v}(x,t) = (0, v_y(x,t), 0)$ can be decomposed into $\boldsymbol{v}_\parallel = (\boldsymbol{v}\cdot\boldsymbol{t})\boldsymbol{t}/\boldsymbol{t}^2$ and $\boldsymbol{v}_\perp = \boldsymbol{v} - \boldsymbol{v}_\parallel$, with

$$\boldsymbol{v}_\parallel = -\frac{A^2\omega k\cos^2(kx - \omega t)}{1 + A^2k^2\cos^2(kx - \omega t)}\,\boldsymbol{t}. \tag{32}$$

According to Eq. (26), this generates the force

$$F_x = (\zeta_\parallel - \zeta_\perp)\frac{1}{L}\int \frac{A^2\omega k\cos^2(kx - \omega t)}{1 + A^2k^2\cos^2(kx - \omega t)}\,dx \tag{33}$$

in the swimming direction, while the force in the perpendicular direction vanishes when averaged over the whole flagellum. For small beating amplitudes, Eq. (33) can easily be integrated, which yields the average propulsion force

$$F_x = \frac{1}{2}(\zeta_\parallel - \zeta_\perp)A^2\omega k. \tag{34}$$

The swimming velocity then follows from $v_x \simeq F_x/\zeta_\parallel$ as

$$v_{flag} = -\frac{1}{2}\left(\frac{\zeta_\perp}{\zeta_\parallel} - 1\right)A^2\omega k\ . \tag{35}$$

This simplified calculation shows several important aspects of flagellar propulsion. First, swimming is only possible due to the frictional anisotropy, i.e. $\zeta_\parallel \neq \zeta_\perp$. Second, for a travelling wave in the positive x-direction, the flagellum moves in the negative x-direction, i.e., movement is opposite to the direction of the travelling wave. Third, the swimming velocity increases linearly with the beating frequency ω and the wave vector k, but quadratically with the beating amplitude A. And finally, the swimming velocity is independent of the fluid viscosity.

A more refined calculation has been performed by Gray and Hancock (1955), also employing resistive force theory, to determine the swimming velocity of sperm. For the sinusoidal beating pattern (29) and $\zeta_\perp/\zeta_\parallel = 2$, they find

$$v_{sperm} = \frac{1}{2}A^2\omega k\left[1 + A^2k^2\right. \tag{36}$$

$$\left. + \sqrt{1 + \frac{1}{2}A^2k^2}\frac{3R_h}{L}\left(\ln\left(\frac{kd}{4\pi}\right) - \frac{1}{2}\right)\right]^{-1}. \tag{37}$$

Here, L is the length of the flagellum and R_h is the radius of the head. The general conclusions wit respect to Eq. (35) remain valid, but additional effects appear. The second term in the brackets of Eq. (36)—its origin is already recognizable in Eq. (32)—arises from the finite beating amplitude and implies a *saturation* of the velocity for large beating amplitudes. The last term in the brackets describes the reduction of velocity due the drag of the passive head.

Friedrich *et al.* (2010) employed a wave form with increasing amplitude of the flagellar beat with increasing distance from the head to describe the beat geometry of bull sperm, and use direct experimental input for the beat amplitude and frequency. In this way, experimental trajectories can be reproduced quite accurately by resistive force theory, when the friction anisotropy is chosen appropriately. This yields the friction anisotropy $\zeta_\perp/\zeta_\parallel = 1.81 \pm 0.07$.

The swimming of sperm has also been analyzed by slender-body theory (Hancock, 1953; Johnson and Brokaw, 1979; Lighthill, 1976) (taking into account the hydrodynamic interactions of different parts of the deformed flagellum as in Sec.III.A for slender rods) by Higdon (1979). Results agree with the resistive-force approach by Gray and Hancock (1955) within about 10%.

A higher order solution, taking into account the full hydrodynamics, is possible for an infinitely long flagellum in *two* spatial dimensions (where hydrodynamics is of longer range than in three dimensions) — corresponding to an infinite sheet with a laterally propagating wave and transverse oscillations in three dimensions. Here, the swimming velocity

$$v_{sperm} = \frac{1}{2}A^2\omega k\left(1 - \frac{19}{16}A^2k^2\right) \tag{38}$$

has already been obtained by Taylor (1951) in his pioneering work. This result confirms all qualitative features discussed above, but shows somewhat different numerical coefficients (which is in part due to the different dimensionality).

The sperm structure or beating pattern is typically not completely symmetric, but has some chirality. In this case, sperm swim on helical trajectories (Crenshaw, 1989; Elgeti and Gompper, 2008). In particular, the helicity of the swimming trajectories is very pronounced for sea urchin sperm (Böhmer *et al.*, 2005; Crenshaw, 1996; Kaupp *et al.*, 2003).

C. Propulsion by Helical Flagella

Resistive force theory (Gray and Hancock, 1955; Lighthill, 1976) as well as slender body theory (Hancock, 1953; Johnson and Brokaw, 1979; Lighthill, 1976) have been applied to describe propulsion of rotating helical flagella. Various aspect of the approaches have been

summarized by Lauga and Powers (2009) in their review. Here, we briefly address slender-body results in the light of recent experiments on macroscopic helices at low Reynolds numbers (Rodenborn *et al.*, 2013).

As shown by Lighthill (1976), the velocity of a point at s along the contour of a flagellum of finite thickness can be described as

$$\boldsymbol{v}(s) = \frac{1}{4\pi\eta}\boldsymbol{f}_\perp(s) + \int \mathbf{H}(\boldsymbol{r}(s)-\boldsymbol{r}(s'))\cdot\boldsymbol{f}(s')\,\Theta(|\boldsymbol{r}(s)-\boldsymbol{r}(s')|-\delta)\,ds' \tag{39}$$

within the far-field approximation (as in Eq. (25)). Here, $\delta = a\sqrt{e}/2$ is the cutoff to avoid self-interactions, $\Theta(x)$ is Heaviside's step function, and $\boldsymbol{f}_\perp$ is the normal component of the Stokeslet strength (Eq. 10), i.e.,

$$\boldsymbol{f}_\perp = \left(\mathbf{I} - \hat{\boldsymbol{t}}\hat{\boldsymbol{t}}\right)\cdot\boldsymbol{f}, \tag{40}$$

where $\hat{\boldsymbol{t}}$ is the local tangent vector to the filament and $\mathbf{I}$ the unit matrix (Lauga and Powers, 2009; Rodenborn *et al.*, 2013).

A helix oriented along the z-axis can be parameterized as

$$\boldsymbol{r}(s) = (R_h\cos\varphi, R_h\sin\varphi, \varphi P/(2\pi))^T. \tag{41}$$

Here, $\varphi = 2\pi s\cos\vartheta/P$ is the helical phase, P the pitch of the helix, ϑ the pitch angle, and R_h the helix radius. From Eq. (41), we obtain the tangent vector and the force (40). Assuming a very long helix $L/P \gg 1$, we can neglect end effects and approximate the local force density by

$$\boldsymbol{f}(s) = (-f_\varphi\sin\varphi, f_\varphi\cos\varphi, f_z)^T \tag{42}$$

and the local velocity by

$$\boldsymbol{v}(s) = (-\Omega R_h\sin\varphi, \Omega R_h\cos\varphi, v_z)^T. \tag{43}$$

Inserting Eqs. (41), (42), and (43) in Eqs. (39) and (40), respectively, the translational velocity v_z and rotational frequency Ω can be represented as

$$\begin{pmatrix} v_z \\ \Omega \end{pmatrix} = \begin{pmatrix} A_{11} & A_{12} \\ A_{12} & A_{22} \end{pmatrix}\begin{pmatrix} f_z \\ m_z \end{pmatrix} \tag{44}$$

by the pulling force density f_z and the moment density $m_z = R_h f_\varphi$. Note that we assume the helix to remain aligned along the z-axis, i.e., other torques are compensated by additional external forces. Neglecting end effects, the matrix elements are given by

$$\begin{aligned}
A_{11} &= \frac{1}{4\pi\eta}\left(\sin^2\vartheta + \frac{1}{\sin\vartheta}\int_{\varphi_0}^{\varphi_L}\left(\frac{1}{\Phi} + \frac{\varphi^2\cot^2\vartheta}{\Phi^3}\right)d\varphi\right),\\
A_{12} &= \frac{1}{4\pi\eta R_h}\left(-\frac{1}{2}\sin 2\vartheta + \frac{1}{\sin\vartheta}\int_{\varphi_0}^{\varphi_L}\frac{\varphi\sin\varphi\cot\vartheta}{\Phi^3}d\varphi\right),\\
A_{22} &= \frac{1}{4\pi\eta R_h^2}\left(\cos^2\vartheta + \frac{1}{\sin\vartheta}\int_{\varphi_0}^{\varphi_L}\left(\frac{\cos\varphi}{\Phi} + \frac{\sin^2\varphi}{\Phi^3}\right)d\varphi\right),
\end{aligned} \tag{45}$$

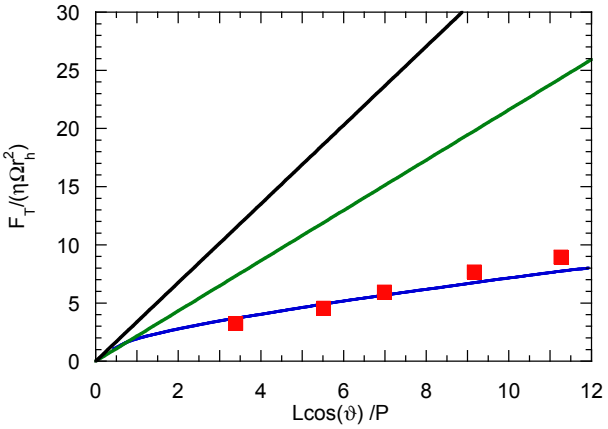

FIG. 19 Thrust of a helical flagellum as function of its length according to Rodenborn *et al.* (2013). The experimental data (squares) agree well with the slender body theory by Lighthill (1976) (blue), the regularized Stokeslet theory by Cortez *et al.* (2005), and the slender body theory by Johnson (1980). The black and green lines are obtained by resistive force theory according to Lighthill (1976) and Gray and Hancock (1955), respectively.

with the abbreviations $\varphi_0 = 2\pi\delta\cos\vartheta/P$, $\varphi_L = \pi L\cos\vartheta/P$, and $\Phi(\varphi) = [4\sin^2(\varphi/2) + \varphi^2\cot^2\vartheta]^{1/2}$ (Rodenborn *et al.*, 2013). Inversion of Eq. (44) yields the thrust, torque, and drag as function of helix length and driving frequency Ω or velocity v_z. In the asymptotic limit $L\to\infty$, the thrust $F_T = Lf$ obeys (Rodenborn *et al.*, 2013)

$$F_T \sim -\frac{L}{\ln(L\cos\vartheta/R_h)}\Omega, \tag{46}$$

i.e., shows a logarithmic dependence on the total helix height $L\cos\vartheta$. The proportionality factors follow from Eqs. (45). In particular, a logarithmic dependence is obtained for A_{11}, since $\Phi\to\varphi\cot\vartheta$ as $\varphi\to\varphi_L\to\infty$ ($L\to\infty$). The other terms converge to finite values. As before, the logarithm appears due to hydrodynamic interactions.

As an example, Fig. 19 shows experimental results for the thrust of helical flagella of various lengths obtained in experiments on macroscopic scale models at low Reynolds numbers by Rodenborn *et al.* (2013). The data compare very well with the slender body theories by Lighthill (1976) and Johnson (1980), respectively, and the regularized Stokeslet approach by Cortez *et al.* (2005). The above asymptotic calculations apply for $L/P > 10^3$. Over the range of ratios L/P relevant for bacteria ($3 \lesssim L\cos\vartheta/P \lesssim 11$), there is a quantitative difference between the full theory and the asymptotic approximation. However, the qualitative length dependence is well captured. More results are presented by Rodenborn *et al.* (2013).

In order to determine the swimming properties of a

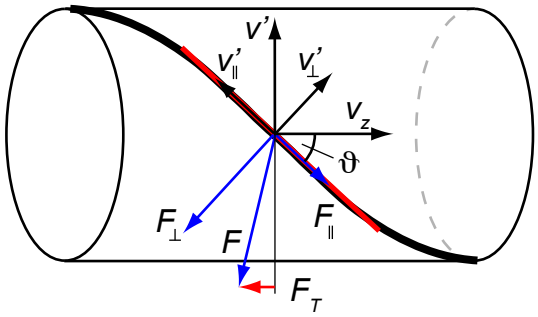

FIG. 20 Helical segment moving in a viscous fluid. Only half of a helical pitch is shown. The drag-based thrust force F_T appears by the motion of the red rodlike segment in the direction v' (see also Lauga and Powers (2009)).

bacterium, we have to consider both, the flagellum bundle as well as the body. For simplicity, we adopt resistive force theory to illustrate the dependence of the swimming velocity on the motor torque rotating a single flagellum (Lauga and Powers, 2009). Inversion of Eq. (44) yields the force and torque on a flagellum due to translation and rotation. Considering the limit of small pitch angles $\vartheta \ll 1$, elimination of rotation by external torques yields $F_z \approx \zeta_\parallel v_z$. Preventing translation, rotation with the velocity $v' = R_h\Omega$ yields the thrust force $F_z = F_T = (\zeta_\parallel - \zeta_\perp)\theta v' = (\zeta_\parallel - \zeta_\perp)R_h\Omega$ (cf. Fig. 20) and the momentum $M_z = \gamma_\perp R_h v' = \gamma_\perp R_h^2\Omega$ with the friction coefficients (28) (Lauga and Powers, 2009). Hence, we obtain

$$\begin{pmatrix} F_z \\ M_z \end{pmatrix} = \begin{pmatrix} \zeta_\parallel & -(\zeta_\perp - \zeta_\parallel) - \vartheta R_h \\ -(\zeta_\perp - \zeta_\parallel)\vartheta R_h & \zeta_\perp R_h^2 \end{pmatrix} \begin{pmatrix} v_z \\ \Omega \end{pmatrix}. \tag{47}$$

More precise resistive force theory results have been presented by Chattopadhyay *et al.* (2006), Magariyama *et al.* (1995), and Purcell (1997). Alternatively, the inverse matrix of Eq. (44), with the elements of Eq. (45), yields a more precise description within slender-body theory.

Approximating the cell body by a sphere of radius R_b and assuming $R_b \ll L$, the frictional body force F_b and the body torque M_b are

$$\begin{aligned} F_b &= -\zeta_b v_z \ , \\ M_b &= -\zeta_r^b \Omega_b \ , \end{aligned} \tag{48}$$

where $\zeta_b = 6\pi\eta R_b$ and $\zeta_r^b = 8\pi\eta R_b^3$ are the translation and rotational friction coefficients. The helix is driven by a rotary motor with the frequency Ω_m relative to the body. In response, the helix and body rotate with the frequencies Ω and Ω_b. These frequencies are related by $\Omega + \Omega_b = \Omega_m$. Since the whole bacterium is force and torque free, i.e., $F_z + F_b = 0$ and $M_z + M_b = 0$, its swimming velocity is given by (Lauga and Powers, 2009)

$$v_z \approx \vartheta \frac{(\zeta_\perp - \zeta_\parallel)\zeta_r^b}{\zeta_\parallel \zeta_\perp R_h}\Omega_m. \tag{49}$$

The friction coefficient ζ_b does not appear, since we assume $\zeta_\parallel \gg \zeta_b$ ($L \gg R_b$). Evidently, swimming is again—as in the sperm case—only possible due to frictional anisotropy. Moreover, v_z depends linearly on the body rotational friction coefficient. Hence, without body, the bacterium could not swim. Due to the approximation $\vartheta \ll 1$, v_z depends linearly on the pitch angle. Changing the handedness of the helix leads to a change of the swimming direction.

We like to mention that a helix driven by an external torque also swims (Ghosh and Fischer, 2009). However, it is not torque free and therefore is not an autonomes swimmer. Under the same assumptions as above, the swimming velocity is $v_h \approx \vartheta\Omega[(\zeta_\perp - \zeta_\parallel)\zeta_r^h]/[\zeta_\parallel\zeta_\perp R_h]$, very similar to Eq. (49), but now with the helix frequency $\Omega = M/\zeta_r^h$, determined by the applied torque M, and the overall helix rotational friction coefficient ζ_r^h.

IV. SWIMMING NEAR SURFACES

Surfaces, interfaces, and confinement are ubiquitous in the microswimmer world. Microswimmers being small, they might be expected to be typically far away from surfaces. There are three important points to remember, however. First, many biological microswimmers regularly encounter surfaces and confinement, from sperm cells in the reproductive tract to microorganisms in the soil (Foissner, 1998; Or *et al.*, 2007). Second, microorganisms often rely on the presence of surfaces for their function and survival; for example, bacteria form biofilms on surfaces for spreading, to enhance cell-cell exchange and nutrient uptake. Third, equally important is that modern microfluidic devices can be used to investigate, control, and manipulate microorganisms in many ways (Denissenko *et al.*, 2012; Kantsler *et al.*, 2013). In order to make predictions and to interpret and understand experimental results, it is thus crucial to account for effects of surfaces and confinement in theoretical models and descriptions.

A generic phenomenon of microswimmers near surfaces is an effective surface accumulation. Already in 1963, Rothschild discovered and quantified an accumulation of sperm cells near a glass cover slide (Rothschild, 1963). Other microswimmers like *E. coli* (Berke *et al.*, 2008) or *Chlamydomonas* (Kantsler *et al.*, 2013) also accumulate at walls. Two mechanisms have been suggested to explain this effect, hydrodynamic interactions and propulsion together with steric interactions. We will address these two mechanisms in the following sections.

Other surface induced phenomena include rectification of microswimmer motion by ratchets (Berdakin

et al., 2013; Kantsler *et al.*, 2013; Tailleur and Cates, 2009), rotation of microgears in bacterial suspensions (Di Leonardo *et al.*, 2010), collective surface adhesion in clusters (Wensink and Löwen, 2008) or geometric traps for microswimmers (Kaiser *et al.*, 2012).

A. Hydrodynamics of Surface Capturing

The far-field interactions of microswimmers can be understood in terms of a multipole expansion. For a force free swimmer, the dominant term is the dipole term, which distinguishes pushers from pullers, see Sec. II.C. A microswimmer at a distance z from a no-slip wall, with an orientation angle θ between the swimming direction and the surface normal vector (pointing into the fluid), experiences a angular velocity (Berke *et al.*, 2008)

$$\Omega_r(\theta, z) = -\frac{3P\cos\theta\sin\theta}{64\pi\eta z^3}\left[1 + \frac{(\gamma^2-1)}{2(\gamma^2+1)}(1+\cos^2\theta)\right] \tag{50}$$

and a drift velcoity (Berke *et al.*, 2008)

$$u_z(\theta, z) = -\frac{3P}{64\pi\eta z^2}\left(1 - 3\cos^2\theta\right) . \tag{51}$$

where P is the dipole strength and γ the aspect ratio of the swimmer shape.

Equation (51) allows several interesting predictions. First, the hydrodynamic interactions decay slowly as $1/z^2$ with increasing distance from the surface, as already explained in Sec. II.C. Second, for pushers (like sperm), the hydrodynamic interaction is attractive for orientations nearly parallel to the wall (with θ near 90°), but repulsive for orientations nearly perpendicular to the wall (with θ near 0°); for pullers (like *Chlamydomonas*), the hydrodynamic interaction is repulsive when they are swimming parallel to the surface. However, in these considerations, the rotation of the swimmer orientation due to hydrodynamics interactions has not yet been taken into account. Equation (50) shows that for the pusher, swimming parallel to the surface and being slowly attracted to it is indeed the stable state. On the other hand, for pushers the parallel orientation is unstable, a reorientation toward the surface occurs, and the microswimmer moves to the surface head-on (Berke *et al.*, 2008; Spagnolie and Lauga, 2012).

As both pushers and pullers come closer to the surface, higher orders in the multipole expansion become important. For spherical or ellipsoidal squirmers, the importance of higher order terms has been studied (Spagnolie and Lauga, 2012). The swimmers are driven by imposing a surface velocity on part of the particle, like in the squirmer model (see Sec. I.C). A boundary-integral formulation of the Stokes equation is used to generate numerically "exact" results for comparison. In the multipole expansion, a general axisymmetric swimmer is described as a linear combination of fundamental solutions to the Stokes equations: a Stokeslet dipole, a source dipole, a Stokeslet quadrupole, and a rotlet dipole. For spherical and ellipsoidal microswimmers, the multipole expansion is found to be surprisingly accurate, sometimes down to surface distances of a tenth of the swimmer length.

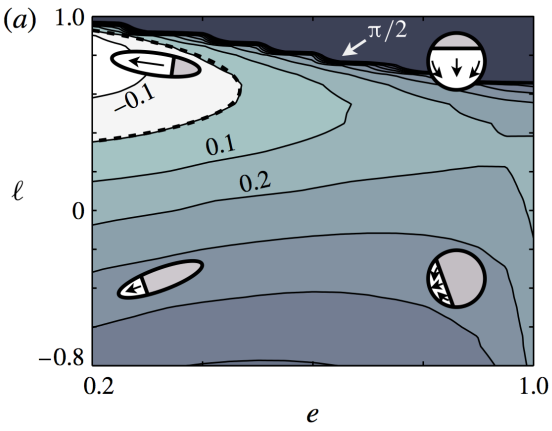

FIG. 21 Contour plot of stable equilibrium pitching angles of ellipsoidal microswimmers (pusher), at fixed distance (equal to the long axis of the ellipsoid) from a wall, as a function of the inverse aspect ratio e and the asymmetry parameter ℓ for the active part of the surface, as indicated by the swimmer shapes. Positive pitching angles are pointing away from the surface. The swimmers are driven by an active region of the rear end, as indicated by the arrows, where $(\ell+1)/2$ is the active fraction of length. From Spagnolie and Lauga (2012).

Physically, the main result is — see Fig. 21 — that microswimmers that are both slender and sufficiently active (but not completely active, $\ell \neq 1$) exhibit pitching equilibria with their noses down toward the wall, while microswimmers that are not sufficiently slender or not sufficiently active exhibit pitching equilibria with their noses turned up away from the wall (Spagnolie and Lauga, 2012). This has important consequences, because a swimmer which points away from the wall will usually not remain at the wall, but excape due to is forward motion. Furthermore, hydrodynamically caused rotation rates for microswimmers approaching a wall are found to be typically small, and for large impact angles not large enough to avoid a collision between the swimmer and the wall (Spagnolie and Lauga, 2012). Thus, eventually a more detailed, swimmer-specific modelling is required.

Ellipsoidal squirmers, with surface velocities given by a sum of Legendre polynomials (compare Eq. (1) for the spherical squirmer), were studied by Ishimoto and Gaffney (2013). A fixed-point analysis yields stable swimming positions for pushers and pullers over a wide range of aspect ratios and B_2- and B_3-amplitudes. However, when B_2 and B_3 are too small, no fixed point is found because hydrodynamic interactions are too weak. Pusher spheres show only unstable fixed points (unless B_3 is very strong), while puller spheres display stable

fixed points with a swimmer orientation toward the wall. As the aspect ratio increases, puller trajectories at a fixed distance from the wall become more unstable, and conversely pushers become stable. Pushers at a fixed point have an orientation away from the wall. Some of the unstable fixed points are found to be surrounded by stable limit cycles, which correspond to swimmers which change their distance from the wall periodically. For an elongated puller with aspect ratio $a = 2$, the distance from the wall is predicted to vary between its size and three times its size Ishimoto and Gaffney (2013). Furthermore, it is predicted that a change of boundary conditions from no-slip to slip significantly changes the location and characteristics of fixed points, and thereby of the swimming behavior near surfaces.

Another important aspect is the competition of hydrodynamic interactions with rotational diffusion (Drescher *et al.*, 2011; Elgeti and Gompper, 2009). When a pusher is deviating by a (small) angle $\delta\phi$ from parallel alignment with the wall due to rotational diffusion, then — in the far-field approximation — it takes a time of order $t_r = \delta\phi/\Omega_r$ (see Eq. (50)) to become aligned again due to hydrodynamic interactions. During this time, it can swim a distance $\Delta z_1 = v_0 \sin(\delta\phi) t_r$ away from the wall due to self-propulsion, but drifts toward the wall by a distance $\Delta z_1 = u_z t_r$ due to hydrodynamic interactions, see Eq. (51). This implies that for $\delta\phi \gtrsim (r_0/z)^2$, the effective swimmer velocity points away from the wall, where r_0 is the swimmer size and z is the distance from the wall, and in the time interval t_r travels a distance $\Delta_z \sim (z^3/r_0^2)\delta\phi$. For distances z a few times r_0, this implies $\Delta_z \sim z$. Thus, for small swimming velocities and large angular fluctuations, a microswimmer is expected to exhibit also large fluctuations in its distance from a wall. Here, the importance of orientational fluctuations can be quantified by the orientational Peclet number $Pe_\phi(z) = \Omega_r(z)/D_R$. Of course, very close to a wall, hydrodynamic interactions become more important, but also the dipole approximation breaks down.

A similar conclusion was reached by Drescher *et al.* (2011), who considered cell-cell scattering. By estimating the mean-square angular change of orientation in cell-cell encounters, both due to hydrodynamic interactions and to rotational diffusion, Drescher *et al.* (2011) estimated a hydrodynamic horizon r_H, beyond which hydrodynamic interactions become irrelevant. For non-tumbling *E. coli*, r_H is found to be comparable to the length of the cell body, about 3μm. However, other effects like flagellar interactions would become important at such short distances. Of course, rotational diffusion becomes less important with increasing microswimmer size.

B. Propulsion-Induced Surfaces Accumulation

Hydrodynamics is not the only mechanism that can explain accumulation of swimmers at surfaces. Indeed, it has to be realized that any self-propelled particle in confinement will eventually encounter a surface. Without a reorientation, the particle will just stay there. Therefore, rotational diffusion is required to induce a detachment from the wall. In order to elucidate this adhesion mechanism, and how noise drives a self-propelled particle away from a wall, it is interesting to consider the behavior of "Brownian" rods — in the absence of any hydrodynamic interactions. In this case, excluded-volume interactions favor parallel orientation near the wall, while the noise leads to fluctuations of the rod orientation and thereby an effective repulsion from the wall. The competition of these two effects gives rise to an interesting adsorption behavior (Elgeti and Gompper, 2009; Li and Tang, 2009).

Results of Brownian dynamics simulations (Elgeti and Gompper, 2009) are shown in Fig. 22. While passive rods are depleted from the surface (because their entropy is reduced near the surface due to restricted orientational fluctuations), active rods show an increased probability density near the surface, which grows with increasing propulsion force f_t, see Fig. 22(left). In addition, the surface accumulation of the rods strongly depends on the rod length l. The surface excess — the integrated probability density to find a rod near the surface relative to a uniform bulk density distribution — is shown in Fig. 22(right). The results show (i) that short rods show little or no surface aggregation for any propelling force, and (ii) that the surface excess initially increases with increasing f_t and L, but then saturates and becomes nearly independent of f_t and L for large propulsion forces and rod lengths (Elgeti and Gompper, 2009).

The physical mechanism behind this behavior is as follows. A rod hits the surface at some point in time, because swimming directions in the bulk are randomly distributed. After contact with the wall, it gets reoriented parallel to the wall. Then it moves parallel to the wall, slowly wiggling its trajectory from the wall again, until it is sufficiently far from the wall that frequent contacts no longer occur.

The surface accumulation of self-propelled rods can be understood more quantitatively by exploiting an analogy of the trajectories of rod-like microswimmers with the conformations of semi-flexible polymers. The self-propulsion of the rod, combined with rotational diffusion leads to a trajectory with a persistence length

$$\xi_p \sim v/D_R \sim \eta v l^3/k_B T \tag{52}$$

similar to a fluctuating polymer. The key difference is however, that the path is directed, and thus not forward-backward symmetric like a polymer. The trajectory of a rod colliding with the wall displays a sharp kink, impossible for a semi-flexible polymer. Leaving the wall, on

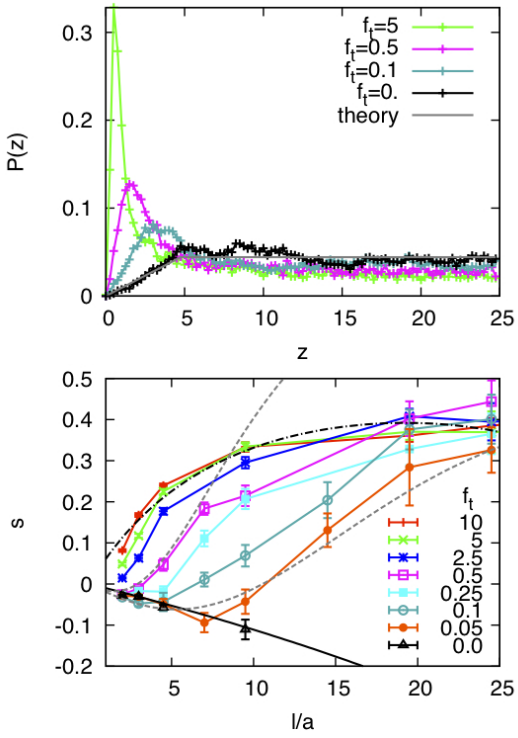

FIG. 22 (Top) Probability density $P(z)$ of self-propelled rods as function of the distance z from the surface, for various propelling forces f_t. The rod length is $l \simeq 10a$ (where a is the rod diameter), the walls are located at $z = 0$ and $z = 5l$. A solid gray line shows the density profile of passive rods. (Bottom) Surface excess s as a function of scaled rod length l/a, for various propelling forces f_t, as indicated. The (black) dashed-dotted line is the scaling result in the ballistic regime (see Eq. (53)), the (gray) dashed lines are scaling results in the diffusive regime for $f_t = 0.5$ and $f_t = 0.05$. From Elgeti and Gompper (2009).

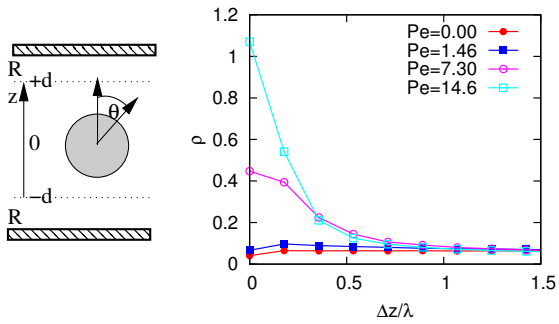

FIG. 23 (Left) A self-propelled Brownian sphere of radius R is confined between two solid walls at $z = \pm(d + R)$. The orientation of the propulsion direction relative to the z-axis, is denoted by θ. (Right) Probability density $\rho(\Delta z)$ to find a particle at a distance Δz from the wall. At zero Peclet number $Pe = v_0/\sqrt{D_r D}$, the probability density is uniform beyond the short range of the repulsive wall. With increasing Peclet number particles accumulate near the wall. Results are shown for a system with wall separation $d/\lambda = 15.6$. The curves correspond to a surface excess of $s = 0$, 0.05, 0.24, and 0.38 with increasing Peclet number, respectively. From Elgeti and Gompper (2013b).

the other hand, happens at a shallow angle, similar to a semi-flexible polymer attached parallel to the wall at one end. This difference in possible conformations leads to an effective attraction of rod-trajectories to the wall, and a repulsion of polymers. In the end, the polymer analogy predicts very well the scaling of the surface excess (Elgeti and Gompper, 2009). In particular, in the *ballistic regime*, with $\xi_p \gg d$, the scaling arguments predict the probability to find the rod near the wall

$$p = l/(l + a_B d), \tag{53}$$

where a_B is a fitting parameter. Note that in this regime Eq. (53) is independent of the propulsion velocity, as observed in simulations.

This effect of accumulation due to the combination of Brownian motion and self-propulsion has later been confirmed experimentally for *C. crecentus* and *E. coli* (Li and Tang, 2009).

An even simpler model microswimmer is a self-propelled Brownian sphere. The essential difference to the self-propelled rod is that the sphere has no alignment interaction with the wall (Elgeti and Gompper, 2013b). Again, self-propulsion leads to accumulation of particles near the wall. The simulation results shown in Fig. 23 demonstrate that the (normalized) probability density $\rho(\Delta z)$ to find a particle at a distance Δz from the wall is strongly peaked close to the wall for $Pe \gtrsim 5$. Figure 24 shows the surface excess s as a function of the Péclet number $Pe = v_0/\sqrt{D_R D_T}$ for different channel widths. Note that s does not saturate at a value $s_{max} < 1$ as is observed for self-propelled rods above, but approaches unity for large Pe (complete adhesion).

The large degree of symmetry allows for an analytic treatment via the Fokker-Planck equation

$$\partial_t \rho(z,\theta,t) = D_r \frac{1}{\sin(\theta)} \partial_\theta \left[\sin(\theta)\partial_\theta \rho(z,\theta,t)\right] - v_0 \cos(\theta)\partial_z \rho(z,\theta,t) + D\partial_z^2 \rho(z,\theta,t), \tag{54}$$

where the angle $\theta = 0$ corresponds to particles oriented in the positive z-direction. This equation already demonstrates the main origin of surface accumulation. The rotational diffusion is independent of the spatial position, but particles are driven to one of the chamber walls depending on their orientation. Thus particles oriented toward the top, accumulate at the top, those pointing down, accumulate at the bottom wall. Less particles remain in the center. Solutions for small Peclet number and narrow channels are depicted in Figure 24, and work well within their respective limits.

Within a concave confinement (i.e. a ring or an ellipse in two dimensions), slow rotational diffusion suppresses

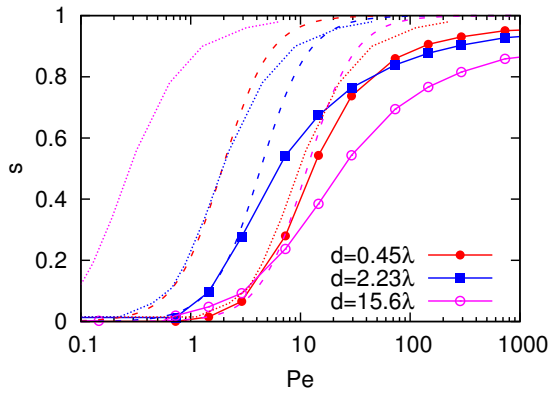

FIG. 24 Surface excess s of active Brownian spheres as a function of Péclet number Pe for various wall separations d, as indicated. Results from the analytic calculation for very narrow channels (dotted lines) match well the simulations for very narrow channels, but fail for wider channels. The approximation for small Péclet numbers (dashed lines) works well for large wall separations. It overestimates the surface excess for large Pe. All analytic expression have no adjustable parameters. From Elgeti and Gompper (2013b).

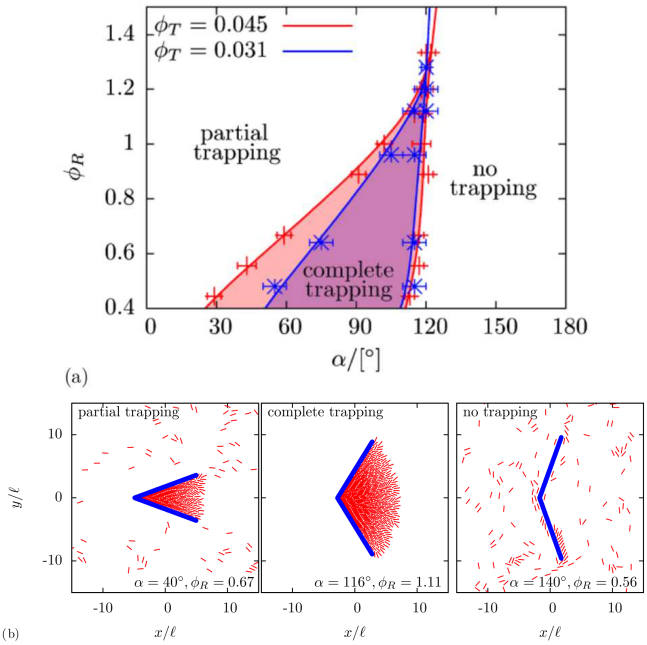

FIG. 25 (a) Phase diagram and (b) snapshots from simulations of many self-propelled rods with funnel-like traps. Active particles can be trapped in funnels, with an opening angle that would not trap single particles. Only due to collective effects does a complete-trapping transition occur at finite densities. From Kaiser *et al.* (2012).

surface detachment; the particle moves along the confinement wall, until it reaches a location where its orientation is perpendicular to the wall. This leads to complete adsorbtion of self-propelled particles in small enough closed environments, and to accumulation in regions of largest wall curvature (because here the largest reorientation by rotational diffusion is required to remove the particle) (Fily *et al.*, 2014a).

These approaches neglect interactions between several swimmers. However, in experiments, microswimmers often occur at finite concentration or even dense suspensions. In these cases, collective effects can play an important role. For example, in a system of many self-propelled Brownian rods between walls in two dimensions, the rods moving along the walls in opposite directions block each other and lead to the formation of "hedgehog-like" clusters (Wensink and Löwen, 2008). This effect can be exploited to capture active particles. As shown above, self-propelled rods accumulate already at walls at infinite dilution. However, combining the "hedgehog-effect" of swimmers blocking each other in a wedge-like geometry, very strong capture of swimmers can be achieved, up to the point of complete trapping. In complete trapping, the swimmers block each other in such a way that none can escape the trap, even at opening angles where single swimmers would escape again (Kaiser *et al.*, 2012) (see Fig. 25).

Capturing of many particles at interfaces can also be exploited to separarte different particle species. Self-propelled discs or rods of different size or velocity in confinement at high densities separate with small and fast particles favored at the interface (Costanzo *et al.*, 2014; Yang *et al.*, 2014a). For soft discs of differenr size and velocity, this segregation can be understood by considering the elastic-energy barrier for a particle to squeeze between two others (Yang *et al.*, 2014a). For hard rods of different velocity, the faster particles push the slower ones away from the wall (Costanzo *et al.*, 2014). External flows in a channel can be used to subsequentially separate the different particles into different compartments (Costanzo *et al.*, 2014).

C. Sperm Hydrodynamics near Surfaces

Sperm frequently encounter situations of swimming in confined geometry, for example in the female reproduction tract (Fauci and Dillon, 2006). The swimming behavior of sperm near walls and surfaces has been studied for sperm of bull (Friedrich *et al.*, 2010; Rothschild, 1963), human (Winet *et al.*, 1984), sea urchin (Böhmer *et al.*, 2005; Cosson *et al.*, 2003; Kaupp *et al.*, 2003), mouse, rat, and chinchilla (Woolley, 2003). All experiments reveal circular or curvilinear trajectories close to the surface. Such trajectories are relevant for the movement of sperm on the epithelial layer that lines the oviduct, and when sperm reach the surface of the much larger egg. For example, many fish eggs on their surface possess a small orifice, called pylum, that must be reached by the sperm for successful fertilization.

For sea urchin sperm, portions of the tail were observed to be outside of the focus plane of the microscope (Cosson *et al.*, 2003), suggesting an out-of-plane component of the beating pattern. Mouse sperm, which are characterized by a strongly curved midpiece, adhere to the wall only when the "left" side of the head faces the glass surface (Woolley, 2003). Chinchilla sperm undergo a rolling motion as they move along the surface, thereby touching the wall with different parts of their head (Woolley, 2003). Finally, the beating pattern of bull sperm seems to be nearly planar parallel to the wall (Friedrich *et al.*, 2010).

Several explanations have been proposed to account for the capture of sperm near a surface (Cosson *et al.*, 2003; Rothschild, 1963; Woolley, 2003). In his pioneering study of bull sperm near surfaces, Rothschild concluded that hydrodynamic interactions are the most likely origin of this effect (Rothschild, 1963). For rodent sperm, two mechanisms have been proposed (Woolley, 2003). For sperm that exhibit a three-dimensional beating pattern and display a rolling motion as they progress (like chinchilla sperm), it was argued that the conical shape of the flagellar envelope establishes a thrust toward the surface. Alternatively, for sperm that exhibit a two-dimensional beating pattern (like mouse sperm), the discoidal shape of the sperm head, which is slightly tilted with respect to the plane of the flagellar beat, may act as a hydrofoil (Woolley, 2003).

Since sperm is a pusher, far-field hydrodynamics predicts a parallel orientation with the wall and an effective hydrodynamic attraction. When the microswimmer comes closer to the wall, so that the dipole approximation is no longer justified, mesoscale simulations (see, e.g. reviews by Kapral (2008) and Gompper *et al.* (2009)) can be employed to elucidate the physical mechanism of attraction to the wall (Elgeti *et al.*, 2010). Alternatively, sperm motion near a wall can be studied by a numerical solution of the Navier-Stokes equations (Smith *et al.*, 2009).

The sperm model used in the simulations of Elgeti *et al.* (2010) is shown in Fig. 26. The main qualitative result is that sperm swims very close to the wall. Fig. 27 shows the flow field of a symmetric, non-chiral sperm near a surface, as obtained from the simulation. The influx of fluid in the midpiece region, which is characteristic for dipole swimmers in the bulk, becomes very asymmetric near the surface: the flow onto the midpiece from above relative to flow from below is greatly enhanced due to the presence of the wall (Fig. 27a). This imbalance of fluxes generates an attraction to the wall in the midpiece region, in qualitative agreement with the predictions by a force-dipole approximation for large distances from the wall (Berke *et al.*, 2008). The flow field near the end of the tail also has a component toward the wall (Fig. 27a); this component is responsible for a hydrodynamic repulsion of the tail from the wall, which induces a tilt of the

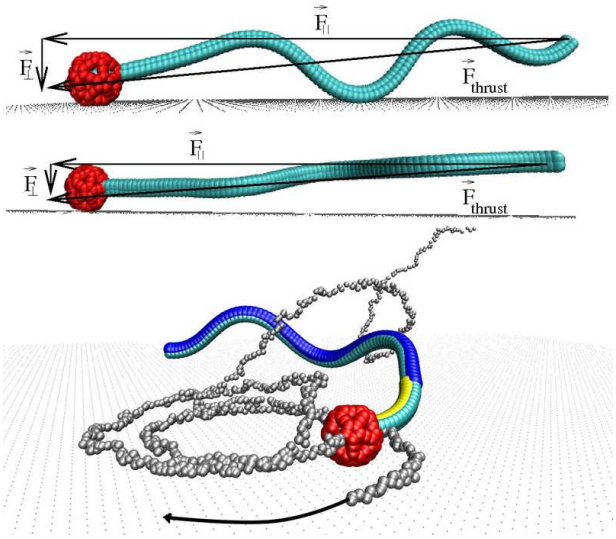

FIG. 26 Sperm model used in mesoscale hydrodynamics simulations of sperm adhesion. (a) Sketch of forces responsible for the adhesion of symmetric sperm at a surface. Top: Without hydrodynamic interactions, the beating-plane of adhering sperm is oriented perpendicular to the surface. Bottom: With hydrodynamic interactions, the beating-plane is oriented parallel to the surface. (b) Sperm with large preferred curvature $c_0^{(m)}$ of the midpiece at a surface (with $c_0^{(m)} L_m = 1$, where L_m is the midpiece length). The head touches the wall and blocks rolling. The beating plane is approximately perpendicular to the surface. From Elgeti *et al.* (2010).

sperm axis toward the surface (Fig. 26). Furthermore, due to the no-slip boundary conditions, the flow in the plane parallel to the wall is screened (Fig. 27b). The far-field approximation predicts the decay r^{-3} for large distances (Drescher *et al.*, 2011; Spagnolie and Lauga, 2012).

Thus, the simulations (Elgeti *et al.*, 2010) reveal that (i) the beating plane of sperm gets oriented parallel to the wall (in agreement with experimental observations (Friedrich *et al.*, 2010)), (ii) the sperm develops a small tilt angle toward the wall (compare Fig. 26a, which enhances the attraction compared to the pure dipole force, and (iii) the elongated shape of sperm contributes to the adhesion effect.

In contrast, on the basis of the numerical solution of the Navier-Stokes equations, Smith *et al.* (2009) predict that sperm swims nearly parallel to the wall, but with a distance comparable to the sperm length, and with a small angle *away* from the wall.

The trend of sperm to follow boundaries can than be exploited to create "one-way channels", recently realized for human sperm swimming in micro-fabricated channels (Denissenko *et al.*, 2012), see Fig. 28. The main idea here is to give the channel walls a "clover-leaf" structure, where sperm following the walls are redirected by 180^0, then leave the wall at a sharp corner. In the same exper-

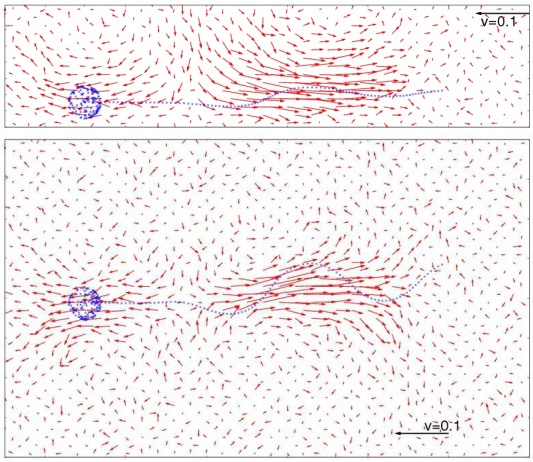

FIG. 27 Averaged flow field in the vicinity of a symmetric sperm cell adhering to a wall. (a) Plane perpendicular to the wall, and (b) plane parallel to the wall, with both planes containing the average sperm shape. A snapshot of a sperm is superimposed. The flow field generated by the beating tail is directed away from the sperm along their swimming direction and toward the sperm along its side. From Elgeti *et al.* (2010).

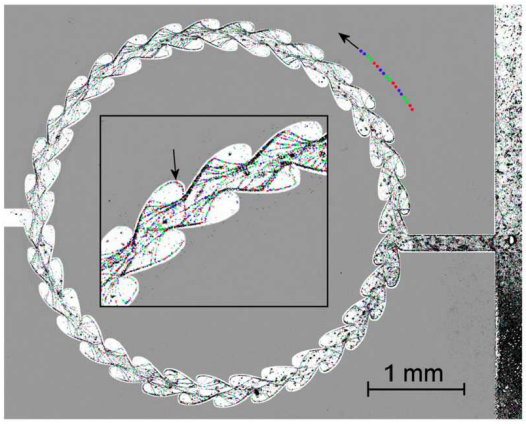

FIG. 28 A microfluidic device, micro-fabricated in PDMS, which presents a "one-way street" for swimming sperm . In this anisotropic channels sperm swim preferentially in a counter-clockwise fashion. Center: A magnification showing how sperm traveling in the wrong direction are forced to turn. The colors represent the time sequences red-green-blue. From Denissenko *et al.* (2012).

iments, it was found that sperm indeed seem to swim at interfaces with finite angle toward the surface confirming the predictions of Elgeti *et al.* (2010), but at variance with the results of Smith *et al.* (2009).

Chiral sperm also adhere to surfaces. In this case, sperm swim on helical trajectories in the bulk (Crenshaw, 1989, 1996; Gray and Hancock, 1955), and in circles at a wall, see Fig. 26b, in good agreement with the experiments mentioned above. The radius of the swimming circles decreases with increasing chirality. Weakly chiral sperm display a rolling motion, while strongly chiral

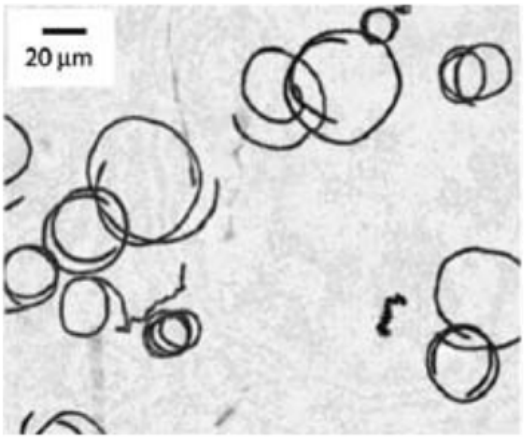

FIG. 29 Superimposed phase-contrast video microscopy images of non-tumbling *E. coli* bacteria (HCB437) swimming in circular trajectories near a glass surface. From Lauga *et al.* (2006).

sperm do not roll (Elgeti *et al.*, 2010). This effect can be understood from the steric hindrance of a strongly asymmetric shape.

D. Bacteria Swimming at Surfaces

The swimming behavior of bacteria close to surfaces differs from the "run-and-tumble" motion in free solution. Experiments show that individual *E. coli* bacteria swim in clockwise, circular trajectories near planar glass surfaces (Berg and Turner, 1990; DiLuzio *et al.*, 2005; Frymier *et al.*, 1995; Hill *et al.*, 2007; Kaya and Koser, 2012; Molaei *et al.*, 2014). In the following, individual cells at surfaces are considered, which could be swimmer or swarmer cells.

The direction of circular motion at a wall depends on the boundary conditions. Since the cell is force and torque free, the body and flagella bundle rotation imply a clockwise rotational motion for a no-slip boundary condition (Lauga *et al.*, 2006; Lemelle *et al.*, 2010; Li *et al.*, 2008; Lopez and Lauga, 2014), see Fig. 29. Hydrodynamics gives rise to an increased drag of the fluid confined between the cell and the surface and a torque appears on the swimmer, which turns the cell in clockwise direction for no-slip boundaries. In contrast, as shown by Lemelle *et al.* (2010) and Lopez and Lauga (2014), slip boundary conditions allow for counter-clockwise circular motion. As a consequence of the preferred circular swimming direction for no-slip boundary conditions, *E. coli* swim preferentially on the right-hand side of a microchannel, when it is confined to the bottom surface (DiLuzio *et al.*, 2005).

Recent experimental studies revealed the flow field near a swimming *E. coli* bacterium, in particular next to a surface (Drescher *et al.*, 2011), see Fig. 30. In this

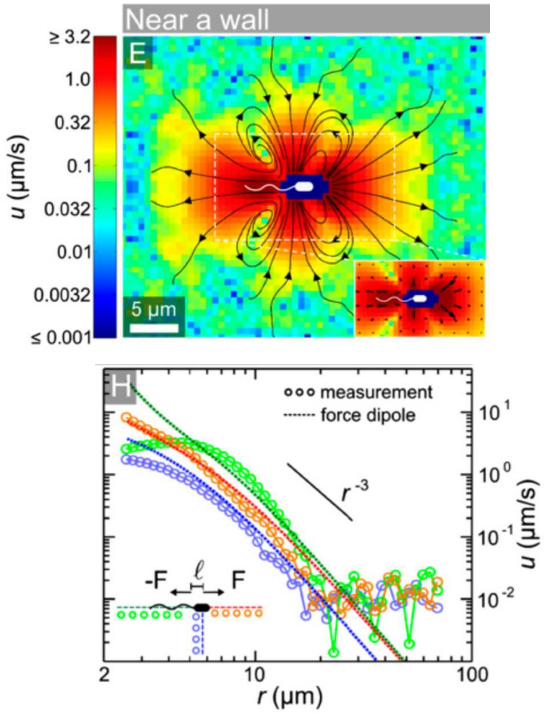

FIG. 30 (a) Experimentally determined flow field of an *E. coli* near a wall. (b) The distance dependence of the flow strength as a function of distance from the microswimmer follows the theoretically predicted power of a dipole swimmer, which decays like r^{-2} in the bulk, see Eq. (12), but like r^{-3} near a surface. From Drescher *et al.* (2011).

case, the flow field can be well described by a simple force dipole model, as discussed in Sec. II.C. Moreover, these studies support the argument that hydrodynamic effects contribute to the observed long residence times of bacteria close to no-slip surfaces (Berke *et al.*, 2008).

In contrast, the experiments of Drescher *et al.* (2011) suggest that cell-surface collisions determine the cell behavior next to surfaces, as proposed by Li and Tang (2009), Elgeti and Gompper (2009), and Hernadez-Ortiz *et al.* (2009), rather than long-range hydrodynamic interactions (Berke *et al.*, 2008). To arrive at the more complete picture of the cell-surface interactions, more precise measurements and more detailed theoretical considerations are necessary.

V. SYNCHRONIZATION

Synchronization of motion is a common phenomenon in nonlinear many-particle systems, and thus appears in a broad range of physical, biological, engineering, and social systems (Pikovsky *et al.*, 2002; Strogatz, 2004). The phenomenon appears at all length scales from atoms to macroscopic bodies. For microswimmers, synchronization is fundamental for coordinated cyclic motion of cilia and flagella. The synchronous beating of the two flagella of *Chlamydomonas* causes straight swimming, while asynchronous beating implies tumbling motion (Bennett and Golestanian, 2013a; Drescher *et al.*, 2010; Goldstein *et al.*, 2011; Guasto *et al.*, 2010; Lauga and Goldstein, 2012; Qian *et al.*, 2009). The helical flagella of bacteria, like *E. coli*, synchronize their rotational motion during bundling (Kim and Powers, 2004; Kim *et al.*, 2003; Reichert and Stark, 2005; Reigh *et al.*, 2012, 2013). Multiciliated and multi-flagellated microorganisms such as unicellular *Paramecia* (Knight-Jones, 1954) or *Volovoxes* (Brumley *et al.*, 2012) exhibit metachronal waves (MCW) (Sleigh, 1962). Here, synchronization is essential for microswimmer motility. Furthermore, coordinated flagellar motion plays a major role in eukaryotes (Polin *et al.*, 2009; Stocker and Durham, 2009), where they transport fluid in the respiratory system in form of cilia (Afzelius, 1976), are involved in cellular communications (Wang *et al.*, 2006), and even determine the morphological left-right asymmetry in the embryo (Cartwright *et al.*, 2004).

As early as 1951, Taylor (1951) suggested that hydrodynamic interactions lead to synchronization of nearby swimming spermatozoa. Since then, the hydrodynamic interactions of active systems at low Reynolds numbers has become a subject of major interest. A recent review by Golestanian *et al.* (2011) addresses a number of important aspects of hydrodynamical induced synchronized motions. Here, we will present and discuss the most important aspects and address recent developments.

Synchronization is not easily achieved for systems governed by low-Reynolds number hydrodynamics and thus described by the Stokes equation (7). The presence of kinematic reversibility of this equation combined with swimmer symmetries may prevent synchronization (Elfring and Lauga, 2009; Kim and Powers, 2004; Reichert and Stark, 2005; Theers and Winkler, 2013). To overcome this fundamental limitation of life at low Reynolds numbers and to generate a time-irreversible dynamics, various alternatives have been suggested. This comprises inclusion of additional degrees of freedom such as system flexibility (Kim and Powers, 2004; Niedermayer *et al.*, 2008; Qian *et al.*, 2009; Reichert and Stark, 2005; Reigh *et al.*, 2012, 2013; Uchida and Golestanian, 2012), or specific, non-reversible driving forces (Bennett and Golestanian, 2013a,b; Uchida and Golestanian, 2011, 2012). In addition, specific system designs combined with hydrodynamic interactions lead to synchronization, as has been shown for models of undulating sheets (Elfring and Lauga, 2009, 2011) and for the flagellar beat of *Chlamydomonas* (Bennett and Golestanian, 2013a,b; Geyer *et al.*, 2013). For the latter, it has been shown that synchronization of flagella beating can be achieved even without hydrodynamic interactions (Friedrich and Jülicher, 2012; Polotzek and Friedrich, 2013). Alternatively, a more general linear unsteady Stokes equation can be adopted to describe the fluid properties (Lauga, 2011; Theers and Winkler, 2013). Here, the time-reversal

symmetry of the fluid-dynamical equation is broken by inertial terms, see Eq. (6).

A. Basic Concepts

Minimalistic models are useful to shed light on the mechanisms of hydrodynamic synchronization. An example is the rigid rotor model of Lenz and Ryskin (2006), where each rotor possesses a single degree of freedom only. Hence, it is particularly useful for analytical studies of fluid mediated interactions between several rotors. Adopting this model, we consider two beads of radius a moving along circles of radius R. The circles are centered at $\boldsymbol{r}_i^0 = (-1)^i \boldsymbol{d}/2$ $(i = 1, 2)$, where $\boldsymbol{d} = d\hat{\boldsymbol{e}}_x$ and d is the center-to-center distance; both beads are confined in the xy-plane. The trajectories of the bead centers can be expressed as

$$\boldsymbol{r}_i(t) = \boldsymbol{r}_i^0 + R\hat{\boldsymbol{e}}_{ri}(t), \tag{55}$$

with the radial unit vectors $\hat{\boldsymbol{e}}_{ri} = (\cos\varphi_i(t), \sin\varphi_i(t), 0)^T$, in terms of the phase angles $\varphi_i(t)$. The driving forces

$$\boldsymbol{F}_i^d(t) = F_i(\varphi_i)\hat{\boldsymbol{t}}_i(t) \tag{56}$$

point along the tangents $\hat{\boldsymbol{t}}_i(t) = (-\sin\varphi_i(t), \cos\varphi_i(t), 0)^T$ of the trajectories. The equations of motion of the particles are given by

$$\dot{\boldsymbol{r}}_i = \frac{1}{\zeta}\boldsymbol{F}_i + \boldsymbol{v}(\boldsymbol{r}_i) = \frac{1}{\zeta}\boldsymbol{F}_i + \sum_{j\neq i} \mathbf{H}_{ij}\cdot\boldsymbol{F}_j \tag{57}$$

within the Stokes description (7) of the fluid, with the hydrodynamic tensor $\mathbf{H}_{ij} = \mathbf{H}(\boldsymbol{r}_i - \boldsymbol{r}_j)$ (10), and the total force $\boldsymbol{F}_i$ on a particle. Since the flow field $\boldsymbol{v}(\boldsymbol{r}_i)$ at the position of particle i, induced by the motion of other particles, is typically not aligned with the tangent vector $\hat{\boldsymbol{t}}_i$, a constraining force $\boldsymbol{F}_i^c$ is necessary to enforce a circular trajectory ($\boldsymbol{F}_i = \boldsymbol{F}_i^d + \boldsymbol{F}_i^c$). However, within the far-field approximation of the hydrodynamic tensor, the constraining force yields corrections of the order $O((a/d)^2)$ to the flow field $\boldsymbol{v}(\boldsymbol{r}_i)$. Hence, for $a/d \ll 1$, we can neglect such contributions and the equations of motion of the phase angles are ($\boldsymbol{F}\cdot\hat{\boldsymbol{t}} = \boldsymbol{F}_i^d\cdot\hat{\boldsymbol{t}} = F_i$)

$$\dot{\varphi}_i(t) = \omega_i + \frac{1}{R}\sum_{j\neq i} F_j\hat{\boldsymbol{t}}_i(t)\cdot\mathbf{H}_{ij}\cdot\hat{\boldsymbol{t}}_j(t), \tag{58}$$

with the frequencies $\omega_i = F_i/(6\pi\eta aR)$. As pointed out by Lenz and Ryskin (2006), Golestanian *et al.* (2011), Uchida and Golestanian (2011), and Theers and Winkler (2013), for constant forces $F_1 = F_2 = F$, the symmetry of the Oseen tensor $\mathbf{H}(\boldsymbol{r}) = \mathbf{H}(-\boldsymbol{r})$ implies a constant phase difference $\Delta\varphi = \varphi_2(t) - \varphi_1(t)$ — so no synchronization occurs.

The same conclusion has been reached by Kim and Powers (2004) and Reichert and Stark (2005) for rigid rotating helices. An extra degree of freedom can be introduced by adding some flexibility in the model. The flexibility can arise from different origins, such as intrinsic flexibility of a filament or flexibility of the anchoring point. Indeed, as shown by Flores *et al.* (2005), Reichert and Stark (2005), Janssen and Graham (2011), and Reigh *et al.* (2012), flexible filaments exhibit synchronized motion.

As far as rotors are concerned, various models for elastic deformation have been investigated. Niedermayer *et al.* (2008) allowed for radial fluctuations of a harmonically bound particle. Qian *et al.* (2009) considered a sphere attached to a rigid rod with its other end confined in a harmonic potential. Uchida and Golestanian (2012) investigated a bead driven by an optical tweezer, whose focus is dragged along a prescribed trajectory. We will adopt the latter approach to illustrate the consequences of elastic deformations on the synchronization of rotors. The position of the bead i is given by $\boldsymbol{r}_i(t) = \boldsymbol{r}_i^0 + R\hat{\boldsymbol{e}}_{ri}(t) + \boldsymbol{u}_i(t)$ for a circular trajectory of the tweezer focus $R\hat{\boldsymbol{e}}_{ri}(t)$ and the displacement $\boldsymbol{u}_i$ in the potential. With the approximation of the tweezer field by a harmonic potential, the equations of motion (57) again apply, with the force balance $\boldsymbol{F}_i + k\boldsymbol{u}_i = 0$, where k is the trap stiffness. For an isolated rotor, i.e, in the absence of fluid flow due to other rotors, $\boldsymbol{v}(\boldsymbol{r}) = 0$, and in the stationary state the force $\boldsymbol{F}_i$ obeys the relation

$$\boldsymbol{F}_i = \zeta\omega_i R\left(\hat{\boldsymbol{t}}_i - \frac{1}{kR}\frac{d\boldsymbol{F}_i}{d\varphi_i}\right), \tag{59}$$

with $\omega_i = \dot{\varphi}_i$. For a constant driving force, this yields the relation $\omega_i = F_i/(\zeta R)$ between the force and intrinsic frequency ω_i. Multiplication of Eq. (57) by $\hat{\boldsymbol{e}}_{ri}$ yields

$$\boldsymbol{u}_i\cdot\hat{\boldsymbol{e}}_{ri} = \frac{\zeta}{k}\hat{\boldsymbol{e}}_{ri}\cdot\boldsymbol{v}(\boldsymbol{r}_i) \tag{60}$$

to $O(k^{-1})$. Similarly, multiplication of Eq. (57) by $\hat{\boldsymbol{t}}_i$ yields the equation of motion for the angles φ_i

$$\dot{\varphi}_i = \omega_i\left(1 - \frac{\zeta}{kR}\sum_j \hat{\boldsymbol{e}}_{ri}\cdot\mathbf{H}_{ij}\cdot\hat{\boldsymbol{t}}_j F_j\right) + \zeta\sum_j \omega_j\hat{\boldsymbol{t}}_i\cdot\mathbf{H}_{ij}\cdot\left[\hat{\boldsymbol{t}}_j + \frac{F_j}{kR}\hat{\boldsymbol{e}}_{rj}\right] \tag{61}$$

to $O(k^{-1})$. By assuming circular trajectories, the far field approximation for the Oseen tensor, and equal forces $F_1 = F_2 = F$, we finally obtain the equation of motion for the phase difference $\Delta\varphi = \varphi_2 - \varphi_1$

$$\frac{d\Delta\varphi}{dt} = -\frac{9a}{2d}\frac{\omega F}{kR}\sin\Delta\varphi. \tag{62}$$

For $\Delta\varphi \ll 1$, we find an exponentially decaying phase difference $\Delta\varphi \sim \exp(-t/\tau_s)$, with the characteristic synchronization time (Qian *et al.*, 2009; Uchida and Golestanian, 2012)

$$\tau_s = T\frac{kdR}{9\pi aF}. \tag{63}$$

The two beads synchronize their rotational motion on a time scale, which is proportional to the trap stiffness k. In the limit $k \to \infty$, i.e., the rotation on the circle discussed above, the synchronization time diverges. The same linear dependence on the constant of the harmonic potential has been obtained by Niedermayer *et al.* (2008).

In addition, Qian *et al.* (2009) considered dumbbell-like rotors with harmonically bound centers as models for symmetric paddles. Here, also a linear dependence of the synchronization time on k is obtained, but with the much stronger dependence $\tau_s \sim kd^5/(a^3RF)$ on the rotor distance.

Flexibility of rotors is not a necessary requirement for synchronization (Theers and Winkler, 2013; Uchida and Golestanian, 2011, 2012). Alternatively, synchronization can be achieved for rigid trajectories by a particular, phase-angle dependent driving forces and/or for trajectories of certain non-circular shapes (Uchida and Golestanian, 2011, 2012). For cilia or the flagella of *Chlamydomonas*, significant force modulations can be expected due to the asymmetry between power and recovery strokes. Uchida and Golestanian (2011) and Uchida and Golestanian (2012) analyzed the necessary conditions for in-phase synchronization for phase-dependent driving forces $\boldsymbol{F}_i^d = F(\varphi_i)\hat{\boldsymbol{t}}_i$, where now $\hat{\boldsymbol{t}}_i = \boldsymbol{r}_i'/|\boldsymbol{r}_i'|$ with the abbreviation $\boldsymbol{r}_i' = d\boldsymbol{r}_i/d\varphi_i$. For circular trajectories, the equations of motion (57) yield

$$\frac{d\Delta\varphi}{dt} = \omega_2 - \omega_1 + \frac{1}{R}\left[F(\varphi_1) - F(\varphi_2)\right]\hat{\boldsymbol{t}}_1 \cdot \mathbf{H}_{12} \cdot \hat{\boldsymbol{t}}_2 \tag{64}$$

for the phase difference. For small phase differences $\Delta\varphi$, linearization leads to

$$\frac{d\Delta\varphi}{dt} = \left(\omega'(\varphi_1) - \frac{1}{R}F'(\varphi_1)\hat{\boldsymbol{t}}(\varphi_1) \cdot \mathbf{H}(\boldsymbol{d}) \cdot \hat{\boldsymbol{t}}(\varphi_1)\right)\Delta\varphi\ . \tag{65}$$

Integration of the ratio $\dot{\Delta\varphi}/\Delta\varphi$ over one time period T yields the cycle-averaged characteristic time (Uchida and Golestanian, 2011, 2012)

$$\tau_s^{-1} = -\frac{2}{T}\int_0^{2\pi}\frac{d\ln F}{d\varphi}\hat{\boldsymbol{t}}(\varphi) \cdot \mathbf{H}(\boldsymbol{d}) \cdot \hat{\boldsymbol{t}}(\varphi)\ d\varphi \tag{66}$$

in the limit $a/d \ll 1$. Uchida and Golestanian (2012) analyzed and identified force profiles which lead to synchronization. Here, we mention and consider the relation

$$F(\varphi) = F[1 - A\sin(2\varphi)] \tag{67}$$

only, where A $(0 < A < 1)$ is a constant. Up to $O(A^2)$, integration results in

$$\tau_s = \frac{2d}{3\pi aA}T, \tag{68}$$

i.e., a characteristic synchronization time which depends on the rotor distance d and the bead diameter a only as far as the rotor geometry is concerned.

It is interesting to note that in this description, synchronization is caused by the tensorial character of the hydrodynamic interactions. The contribution of the diagonal part of the Oseen vanishes by the integration (66) (Uchida and Golestanian, 2011, 2012). In contrast, for the harmonically bound beads, all parts of the hydrodynamic tensor contribute to the time τ_s.

More details of the phase-angle dependent driving forces and different trajectory shapes are discussed by Uchida and Golestanian (2012). In particular, the combined effect of harmonically bound beads, driven by phase-angle dependent forces are addressed. The characteristic decay rate τ_s^{-1} of the combined effects is the sum of the contributions of the individual contributions Eq. (63) and (68).

Kotar *et al.* (2013) recently presented experimental results for the synchronization of two colloids, which are driven by feedback-controlled optical tweezers. Both, the elasticity of the trajectory and a phase-angle dependent driving force was implemented, as discussed above. The colloids exhibit strong synchronization within a few cycles, even in the presence of noise, consistent with the considerations described above.

The relevance of the various contributions depends on the actual parameters, e.g., the stiffness of the radial (harmonic) potential and amplitude of the force modulations along the trajectory. These values have been chosen by Kotar *et al.* (2013) such that both contributions are important. As pointed out by Uchida and Golestanian (2012), however, for small disturbance of a trajectory by hydrodynamic interactions, compared to the size of a trajectory, flexibility has only a weak effect in establishing synchronization. Although this may apply to certain systems only, it reflects a shift in paradigm from a flexibility dominated synchronization mechanism to driving-force governed processes.

A different hydrodynamic route was adopted by Theers and Winkler (2013), who started from the linearized Navier-Stokes equations (6). In this case, the hydrodynamic tensor is time dependent. This leads to the equations of motion

$$\dot{\varphi}_i = \omega + \frac{F}{R}\sum_{j\neq i}\int_0^t \hat{\boldsymbol{t}}_i(t) \cdot \mathbf{H}(\boldsymbol{r}_i(t) - \boldsymbol{r}_j(t'), t - t') \cdot \hat{\boldsymbol{t}}_j(t')dt' \tag{69}$$

for the phase angles of circular rotors driven by the constant force $F_1 = F_2 = F$, with the intrinsic frequency

$\omega = F/(\zeta R)$. Here, the whole time history contributes to the dynamical behavior. In the limit $a/d \ll 1$ and for times $t \gg \tau_\nu = d^2/\nu$, an approximate expression for the integral can be derived, which becomes

$$\frac{d\Delta\varphi}{dt} = -\frac{2\sqrt{\pi}a\nu}{d^3 T}\int_0^t \left(\frac{d^2}{\nu t'}\right)^{3/2} \sin(\omega t')\; dt'\; \Delta\varphi(t) \quad (70)$$

for small phase differences. In the long-time limit, the phase difference decays exponentially with the characteristic time (Theers and Winkler, 2013)

$$\tau_s = \frac{d}{4\pi^{3/2}a}\sqrt{\frac{T}{\tau_\nu}}T. \quad (71)$$

Compared to the other mechanisms described above, τ_s depends on the square-root of the ratio T/τ_ν of the rotation period T and the shear-wave propagation time τ_ν. This ratio can be identified with the oscillatory Reynolds number Re_T (5). Hence, the synchronization time (71) is determined by the oscillatory Reynolds number, but with a square-root dependence.

For typical parameters of *E. coli* bacteria, the time-dependent hydrodynamic correlations have a weak effect on synchronization only. Studies of the combined effect of phase-angle dependent driving forces and time-dependent hydrodynamic interactions yield a faster synchronization dynamics than the individual mechanisms only.

Various other concepts have been put forward to study synchronization of two rotors and, in particular, the appearance of a phase lag as a prerequisite for the formation of metachronal waves. For the latter, in addition, hydrodynamic interactions with a surface are taken into account by employing the Blake tensor (Blake, 1971a) for hydrodynamic interactions near a no-slip wall. Among the first to study this phenomenon were Lenz and Ryskin (2006), Vilfan and Jülicher (2006), and Niedermayer *et al.* (2008). As discussed above (Eq. (63)), synchronization is obtained for beads confined in radially harmonic potentials and equal driving forces. A phase-locked motion has been found for different driving forces by Niedermayer *et al.* (2008). In contrast, Brumley *et al.* (2012) found a stable phase lag even for equal driving forces. They considered the equation of motion of a bead

$$\dot{\boldsymbol{r}}_i = \boldsymbol{\zeta}^{-1}\cdot\boldsymbol{F}_i + \sum_{j\neq i}\hat{\mathbf{H}}_{ij}\cdot\boldsymbol{F}_j, \quad (72)$$

where $\boldsymbol{\zeta} = \zeta[\mathbf{I} + 9a(\mathbf{I} + \hat{\boldsymbol{e}}_z\hat{\boldsymbol{e}}_z)/(16z)]$ is the friction tensor and $\hat{\mathbf{H}}_{ij}$ is Blake's tensor, which take into account the no-slip boundary condition at the wall at $z = 0$. The force is given by $\boldsymbol{F}_i = -k(|\boldsymbol{r}_i| - R)\hat{\boldsymbol{e}}_{ri} + F\hat{\boldsymbol{t}}_i$. As pointed out by Brumley *et al.* (2012), a numerical solution of the equation yields a stable phase lag $\Delta\varphi \neq 0$. A numerical solution of Eq. (72) is shown in Fig. 31 for bead trajectories perpendicular to the surface. Due to the boundary

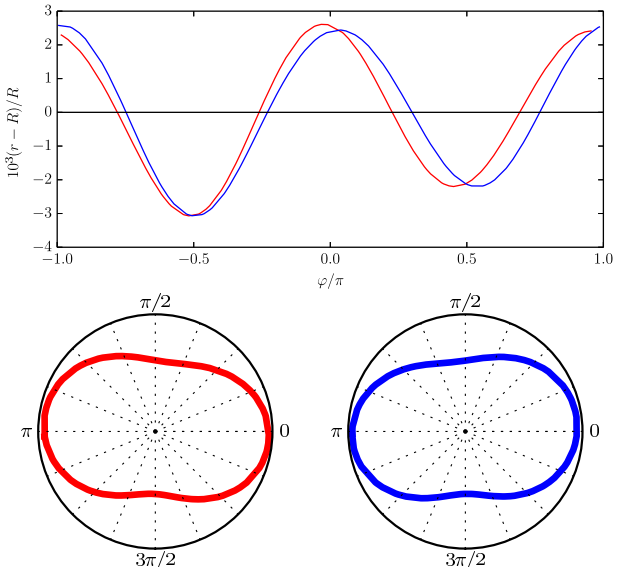

FIG. 31 Deviation of the radial distance r from a circle of radius R for beads of two hydrodynamically coupled rotors in the vicinity of a surface at $z = 0$. The trajectory is confined in a plane perpendicular to the surface. The phase angle $\varphi = 0$ corresponds to the unit vector $\hat{\boldsymbol{e}}_r = (1, 0, 0)^T$. In the polar representations (bottom), the deviation $(r - R)/R$ is multiplied by 100 for better visibility.

condition, the flow properties are different for the motion toward and away from the surface. This shifts the phase difference from perfect synchronization to a finite phase lag (Brumley *et al.*, 2012). Interestingly, $\Delta\varphi$ is independent of the initial condition and the strength k of the potential. Phase-locking seems to be a consequence of nonlinear interactions in the system, because Niedermayer *et al.* (2008) found synchronization rather then phase-locking for their approximate description. As indicated in Fig. 31, the trajectory is ellipse-like, with the long axis along the x-axis and the short axis along the z-axis (perpendicular to surface), with a somewhat smaller deviation $|r - R|/R$ on the side further away from the surface than close to it.

B. Experimental Results: Microrotors and Colloidal Oscillators

As an experimental realization of driven rotors, chiral propellers have been designed, which are driven by radiation pressure (Di Leonardo *et al.*, 2012). In the light of the discussions of Sec. V.A, the symmetry-breaking mechanism is provided by the flexibility of the optical trap, which is used to provide stable alignment and the driving torque. As shown by Di Leonardo *et al.* (2012), two such rotors synchronize their rotational dynamics by hydrodynamic interactions. However, the coupling is very weak, and requires a fine-tuning of the relative

torque within a resolution of 10^{-3}. Even then, phase slips occur, where one of the rotors moves faster than the other until a stable phase-locked state may appear again.

In contrast, strong static correlations are obtained through hydrodynamic interactions between colloidal particles in rotating energy landscapes (Koumakis and Di Leonardo, 2013). Thereby, the particles are driven periodically around a circle by rotating energy landscapes with a variable number of minima. In the co-moving, rotating frame, a colloid experiences a tilted periodic potential due to the hydrodynamic interaction with the other colloids. This enhances the probability to overcome the barriers and allows the different colloids to synchronize their rotational motion.

Another strategy to synchronize the dynamics of beads has been proposed by Gueron and Levit-Gurevich (1998); Gueron *et al.* (1997). It is based on the difference between the power stroke and the recovery stroke of cilia, or, more generally, the presence of two phases with broken symmetry. The latter concept has been applied to colloidal systems by Lagomarsino *et al.* (2003), Kotar *et al.* (2010), Bruot *et al.* (2011), Damet *et al.* (2012), and Lhermerout *et al.* (2012). Here, the periodic motion of colloids is controlled by a configuration-dependent external input. Thereby, various properties can be switched from one state to another upon a particular geometry being assumed by the colloids. Examples are different effective drags (Lagomarsino *et al.*, 2003), or harmonic potentials with different equilibrium positions (Kotar *et al.*, 2010). The latter can be realized by optical traps. These strategies lead to a synchronized motion by hydrodynamic interactions (Bruot *et al.*, 2011; Damet *et al.*, 2012; Kotar *et al.*, 2010; Lagomarsino *et al.*, 2003; Lhermerout *et al.*, 2012; Wollin and Stark, 2011).

C. Synchronization of *Chlamydomonas* Beating

Chlamydomonas with its two beating flagella (see Sec. I.A) has become a model system for experimental studies of synchronization (Polotzek and Friedrich, 2013). When the flagella beat synchronously, the alga swims along a straight path, while dephasing leads to reorientation in a run-and-tumble-like manner (Goldstein *et al.*, 2009; Lauga and Goldstein, 2012; Polin *et al.*, 2009).

The measured flow field of a swimming *Chlamydomonas* (Drescher *et al.*, 2010; Guasto *et al.*, 2010) is well described by three Stokeslets (see Fig. 32). This finding has stimulated a more detailed theoretical modeling of *Chlamydomonas* by three spheres — two spheres driven on circular orbits, which are mimicking the flagellar beat (see Sec. V.A), are linked by a frictionless scaffold to a third sphere representing the cell body (Bennett and Golestanian, 2013a,b; Friedrich and Jülicher, 2012; Polotzek and Friedrich, 2013).

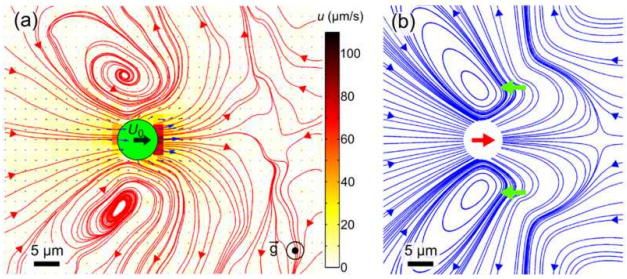

FIG. 32 Time- and azimuthally-averaged flow field of *Chlamydomonas*. (a) Streamlines computed from the experimentally measured velocity vectors (blue). (b) Streamlines of the azimuthally-averaged flow of an assumed three-Stokeslet model: flagellar thrust is distributed between two Stokeslets located at the approximate flagellar position (green arrows), whose sum balances drag on the cell body (central red arrow). From Drescher *et al.* (2010).

The extra translational and overall rotational degrees of freedom, compared to the two degrees of freedom of the rotors of the systems of Sec. V.A, combined with nonlinearities, give rise to additional features. As shown by Bennett and Golestanian (2013b); Friedrich and Jülicher (2012); Polotzek and Friedrich (2013), force and momentum balance predominantly couple the phases of the rotors via translation and rotation of the cell body. This coupling suggest the possibility of flagella synchronization by local hydrodynamic friction even in the absence of hydrodynamic interactions. The efficiency of synchronization naturally depends on the geometry. It is weaker than hydrodynamic coupling, when the cell body is much larger than the distance between the neighboring flagella or cilia (Uchida and Golestanian, 2012).

The three-sphere model exhibits a very rich dynamical swimming behavior, when a phase-angle dependent driving force and noise is added. Without hydrodynamic interactions, the cell just moves forward and backward and there is no net motion. However, in the presence of hydrodynamic interactions, which vary in strength during a beating cycle, the broken symmetry between the power and recovery stroke leads to a net propulsion (Bennett and Golestanian, 2013b). Interestingly, a run-and-tumbling motion is obtained in the presence of noise. The threshold-like run-and-tumble behavior displayed by bacteria like *E. coli* and believed to be controlled by a sophisticated biochemical feedback mechanism, emerges here naturally from nonlinearities in the propulsion mechanism and could be triggered even by white noise. Moreover, the same model could describe the experimentally observed antiphase beating pattern of a *Chlamydomonas* mutant (Bennett and Golestanian, 2013b; Leptos *et al.*, 2013).

An experimental and theoretical study of the effect of the hydrodynamic coupling on the synchronization of the flagella beating is presented by Geyer *et al.* (2013). The

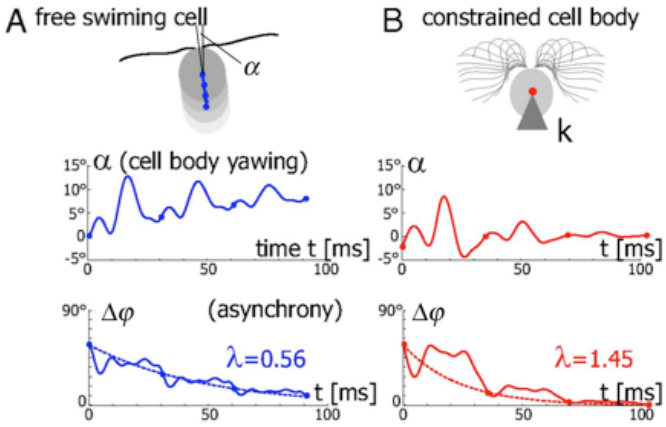

FIG. 33 Flagella synchronization by cell-body yawing. (A) For a free-swimming cell, the cell body exhibits a yawing motion characterized by the angle $\alpha(t)$, when the two flagella beat initially asynchronously. The flagellar phase difference $\Delta\varphi$ between the left and right phase (see Sec. V.A) decreases with time approximately exponentially, $\exp(-\lambda t/T)$, where $\lambda(\approx 0.5-0.6)$ defines a dimensionless synchronization strength. Dots indicate the completion of a full beat cycle of the left flagellum. (B) Trapped cell body to prevent translation. Cell-body yawing is restricted by an elastic restoring torque that acts at the cell body center. The two flagella synchronize with a synchronization strength λ that can become even larger than in the case of a free swimming cell. For very large clamping stiffness, the cell body cannot move and the synchronization strength attenuates to a basal value $\lambda \approx 0.03$, which arises solely from direct hydrodynamic interactions between the two flagella. From Geyer *et al.* (2013).

central mechanism of an efficient synchronization is the adaptation of the flagellar beat velocity to environmental conditions — the flagella beat speeds up or slows down in response to the exerted hydrodynamic friction forces. A perturbation of the synchronized beating leads to a yawing motion of the cell, which is reminiscent to rocking of the cell body (see Fig. 33) (Geyer *et al.*, 2013). This rotational motion confers different hydrodynamic forces on the flagella, with the consequence that one of them beats faster and the other slows down. The coupling between cell-body rotation and flagellar beating speed leads to a rapid reestablishment of a synchronized motion.

The studies by Geyer *et al.* (2013) suggest that cell rocking is an important mechanism for flagella synchronization. However, synchronized beating was also observed for *Chlamydomonas* cells with their bodies restrained by a micropipette (Goldstein *et al.*, 2009; Polin *et al.*, 2009; Rüffer and Nultsch, 1998). A rather fast synchronization has been obtained, faster than pure hydrodynamic interactions would suggest (Geyer *et al.*, 2013). Rotational motion with a small amplitude of a few degrees only, which may result from either a residual rotational compliance of the clamped cell or an elastic anchorage of the flagellar pair, provides a possible mechanism for rapid synchronization, which is analogous to synchronization by cell-body rocking in free-swimming cells (see Fig. 33).

These results lead to the conclusion that hydrodynamic interactions are an integral part of the synchronization mechanism of flagella beating. However, additional degrees of freedom of a specific system may enhance synchronization. In this context, we like to point out that purely hydrodynamic synchronization of the motion of two flagella has recently been documented by Brumley *et al.* (2014).

D. Synchronization of Rotating Bacterial Flagella and Bundle Formation

Synchronization of the rotational motion of helical flagella of bacteria is essential for bundle formation and hence their swimming motion. Theoretical (Reichert and Stark, 2005) and simulation (Kim and Powers, 2004) studies show that rigid helices rotated by stationary motors do not synchronize their rotational motion. However, addition of certain flexibility, e.g., for helices with their ends confined in harmonic traps, combined with hydrodynamic interactions lead to a synchronized rotation even for separated and mechanically not interacting helices (Reichert and Stark, 2005) as already suggested by macroscopic-scale model experiments (Kim *et al.*, 2003; Macnab, 1977).

A more detailed picture of bundle formation has been achieved by computer simulations of model flagella (Flores *et al.*, 2005; Janssen and Graham, 2011; Reigh *et al.*, 2012, 2013). In particular, the role of fluid dynamics has been elucidated. Considering two parallel helices composed of mass points (see Fig. 34) with bending and torsional elastic energy, and using a mesoscale hydrodynamics simulation technique (Gompper *et al.*, 2009; Kapral, 2008), Reigh *et al.* (2012) calculated the hydrodynamic forces on each helix due to their rotation motion. The simulations reveal a zero force along the radial distance, consistent with the results for macroscopic helices of Kim and Powers (2004). However, there are large transverse forces in opposite directions. The rotation of a helix creates a flow field, which tries to drag the other helix in the transverse direction. A "tipping" momentum has been determined by Kim and Powers (2004), which expresses the same effect. Hence, there is no simple attraction between helices by hydrodynamic interactions, as has been speculated. Bundling is rather induced by the common flow field created by the rotation of the individual helices. This expresses the importance of the rotational flow field as suggested by Flores *et al.* (2005).

Releasing the constraints on the orientation provides insight into the full bundling process (Janssen and Graham, 2011; Reigh *et al.*, 2012), as illustrated in Fig. 34. Starting from an aligned initial state, the tangential hy-

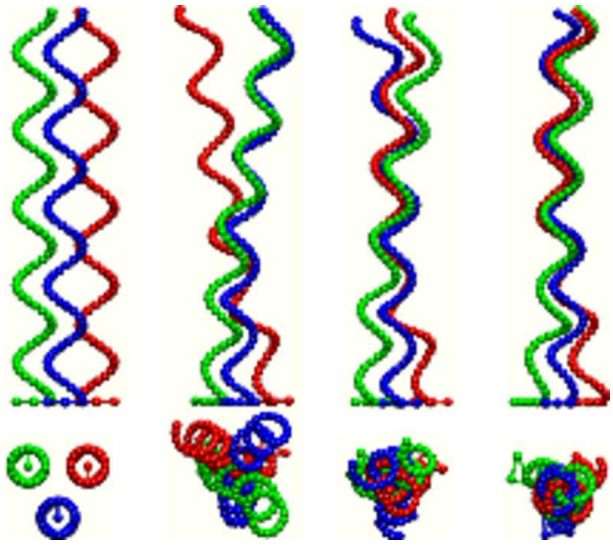

FIG. 34 Snapshots, side views (top) and top views (bottom), of various stages of the bundling process for $d/R_h = 3.5$. (i) Initial state, the red helix is out of phase. (ii) The helices synchronized their rotation and start to bundle. (iii) Parts of the helices are bundled. (iv) Final, bundled state. From Ref. (Reigh *et al.*, 2012).

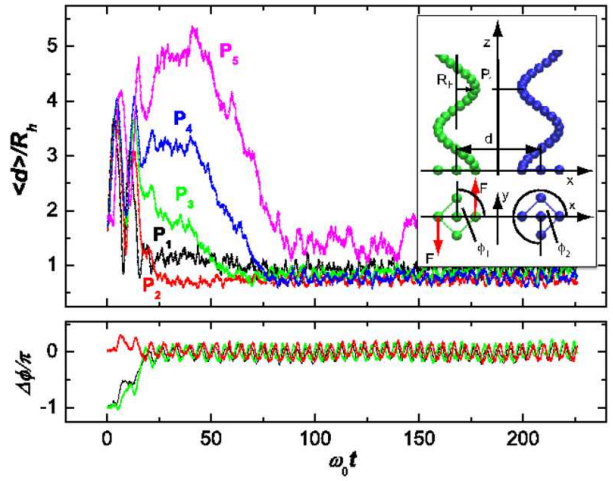

FIG. 35 Phase angle difference $\Delta\phi$ (bottom) and average distances $\langle d \rangle$ (top) between equivalent points $P_i = iP$ along the helix contour as a function of time for the separation $d/R_h = 2.5$. The three helices have the initial phase differences $\Delta\phi_{12} = -\pi$ (black), $\Delta\phi_{13} = 0$ (red), and $\Delta\phi_{12} = -\pi$ (green). From Ref. (Reigh *et al.*, 2012).

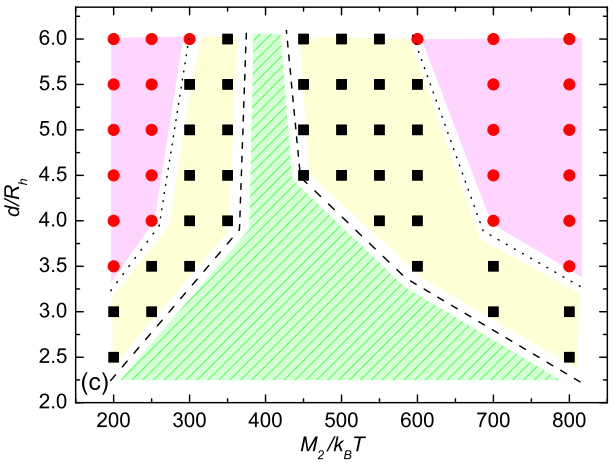

FIG. 36 Phase diagram indicating stable bundles (green), intermittent slippage (yellow), and drifting states (red) of a system of three helices exposed to different torques and for various helix-base separations d. Two helices $(1, 3)$ experience the torque $M_1 = M_3 = 400 k_B T$, whereas the torque M_2 is varied (Reigh *et al.*, 2013).

drodynamic forces cause a tilt of the individual helices, which brings them in closer contact near their fixed ends and simultaneously separates their free ends. Such a spatial approach was already assumed to be necessary by Macnab (1977). The whole mechanism is quantitatively reflected in the time dependence of the helix separations shown in Fig. 35, where the mean distance at P_2 rapidly approaches its stationary-state value, while P_5 increases initially and only slowly reaches its stationary-state value. Naturally, the details depend on the separation d between the anchoring points (Reigh *et al.*, 2012). In the stationary state, a compact bundle is formed, where the helices are wrapped around each other. The stationary-state distances are assumed in sequence from P_1 to P_5, which implies that bundling occurs from the anchoring plane to the tail. Figure 35 shows that, starting from an initial phase mismatch, the helices first synchronize their rotational motion and then subsequently form a bundle. Thereby, synchronization by hydrodynamic interactions is achieved within a few rotations. The simulations predict a synchronization time proportional to $d^2/(R_h^2\omega_0)$ and a bunding time proportional to $d/(R_h\omega_0)$, where ω_0 is the helix rotation frequency (Reigh *et al.*, 2012). The scaling of the synchronization time can be understood by estimating the time needed for the helices to come close to each other in the rotational flow field $v(r) \sim R_h^2/(\omega_0 r)$ generated by the other helices,

$$\omega_0 t_{syn} \sim \omega_0 \int_0^\pi d\phi \;\; d/v(d) \sim (d/R_h)^2. \qquad (73)$$

Bundling is a rich phenomenon, with a multitude of bundling states depending on the elastic properties of a flagellum. For example, it has been shown by Janssen and Graham (2011) that for certain flagellum flexibilities and depending on the initial condition, either rather tight bundles, with the flagella in mechanical contact, or loose bundles, with intertwined, non-touching flagella can be found.

This raises the question of the stability of a flagellar bundle. There are various sources, which give rise to fluctuations and variations in the torque of a flagellum, such as an intrinsic noise in the motor torque, or the

inequality of motors (Chen and Berg, 2000; Xing *et al.*, 2006). Variations may even be induced on purpose, as for bacteria such as *R. lupini*, which control the motor torque to induce tumbling (Scharf, 2002). Simulations of three flagella, in which one helix is driven by a different torque than the other two, yield the following qualitative classification of the bundling dynamics (see Fig. 36) (Reigh *et al.*, 2013). At small torque differences, the bundle remains stable with a phase lag between the various flagella. For very large torque differences, the bundle disintegrates and the flagella rotate asynchronous and independently, i.e., the phase differences of neighboring helices are drifting. In between, there is an intermittent regime, where phase slippage occurs, i.e., the synchronized rotational motion is interrupted by events, where the flagellum with the larger torque leaves the bundle, rotates faster, and rejoins the bundle. The time interval between individual slippages decreases with increasing torque difference and ultimately drifting is obtained. This is quantitatively shown in Fig. 36. It is important to note that bundle formation is rather robust over a wide range of torques and separations, so that bundles are able to sustain considerable torque differences. Even for distances as large as $d/R_h = 4$, phase locking occurs for torque differences as large as $\Delta M/M_1 \approx 1/3$. Both, the high bundle stability and the asymmetry of the phase diagram with respect to the reference torque $M_{1,3}/k_BT = 400$ is a consequence of the flagellar flexibility, which allows the helices to partially wrap around each other — which happens differently for smaller and larger torques M_2/k_BT due to the chiral structure and the different hydrodynamic interactions. This can be compared with the synchronization of rigid, three-arm colloidal micro-rotators discussed by Di Leonardo *et al.* (2012), which can tolerate only very small torque differences on the order of $\Delta M/M_1 \approx 10^{-4}$ at much smaller distances of $d/R_h = 2.0$ to 2.5. The largely enhanced bundle stability is due to the flexibility of the bacterial flagella; thus, intertwisting stabilizes a bundle and ensures a coordinated and synchronized motion, which cannot be provided solely by hydrodynamic interactions.

E. Synchronization of Sperm and Flagella

When two sperm swim close to each other, at distances smaller than the sperm length, then the dipole approximation does not apply and the full hydrodynamic interactions between two time-dependent flagellar shapes have to be taken into account. An particularly interesting aspect of this interaction is that the flagellar beats of the two sperm can now affect each other. What typically happens is phase locking, *i.e.*, the two flagella adjust such as to beat in synchrony.

This synchronization of the beat of swimming sperm has been studied by mesoscale simulations in two dimensions (Yang *et al.*, 2008). Two sperm, S1 and S2, are placed inside a fluid, initially with straight and parallel tails at a small distance with touching heads. They start to beat at $t = 0$ with fixed frequency ω, but with different initial phases φ_1 and φ_2. Here, the beat is driven by the local time-dependent preferred curvature $c_0(s,t) = A\sin(\omega t - ks + \varphi)$ at position s along the flagellum. The flagellar shapes and the relative positions can adjust due to hydrodynamic interactions.

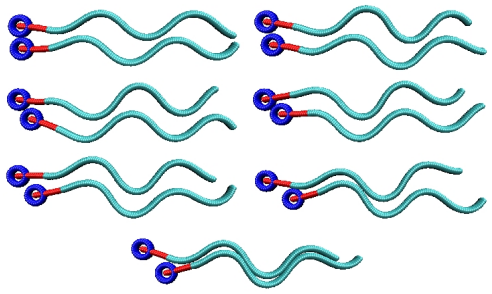

FIG. 37 Snapshots of two sperm in two dimensions, with phases φ_1 (upper), φ_2 (lower), and phase difference $\Delta\varphi = \varphi_2 - \varphi_1 = 0.5\pi$. (a) $t\omega = \pi/3$ initial position; (b) $t\omega = 4\pi/3$; (c) $t\omega = 7\pi/3$; (d) $t\omega = 10\pi/3$; (e) $t\omega = 13\pi/3$; (f) $t\omega = 61\pi/3$; (g) $t\omega = 601\pi/3$ (from top left to bottom). From (a) to (e), the synchronization process takes place. The tails are already beating in phase in (e). From (e) to (g), two synchronized sperm form a tight pair due to hydrodynamic attraction. From Yang *et al.* (2008).

In the dynamical behavior of these hydrodynamically interacting sperm, two effects can be distinguished, a short time "synchronization" and a longer time "attraction" (Yang *et al.*, 2008). If the initial phase difference $\Delta\varphi = \varphi_2 - \varphi_1$ is not too large, "synchronization" is accomplished within a few beats. This process is illustrated by snapshots at different simulation times in Fig. 37. The synchronization time depends on the phase difference, and varies from about two beats for $\Delta\varphi = 0.5\pi$ (see Fig. 37) to about five beats for $\Delta\varphi = \pi$. A difference in swimming velocities adjusts the relative positions of the sperm. After a rapid transition, the velocities of two cells become identical once their flagella beat in phase.

The synchronization and attraction of sperm has also been observed experimentally (Woolley *et al.*, 2009; Yang *et al.*, 2008). Figure 38 shows two human sperm with synchronized beats, which swim together for a while, but then depart again due to somewhat different beat frequencies and thus different swimming velocities. On the other hand, for bull sperm, persistent synchrony of the flagellar beats has been observed only when the heads are tightly coupled mechanically (Woolley *et al.*, 2009).

Symmetry arguments show that synchronization is *not* possible for two co-swimming flagella with a prescribed, *reflection-symmetric* wave form (Elfring and Lauga, 2009), described in the spirit of Taylor (Taylor, 1951) by two infinite parallel two-dimensional sheets with

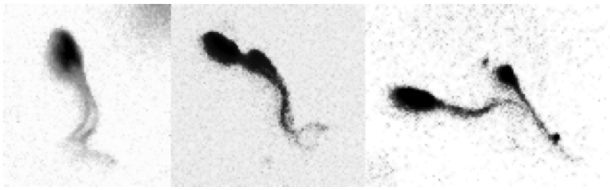

FIG. 38 Experimental snapshots of two human sperm swimming together at different times. (Left) Two sperm with initially well synchronized tails and very small phase difference; (Middle) the sperm are still swimming together and are well synchronized after 4 seconds; a phase difference has developed; (Right) the sperm begin to depart after 7 seconds. From Yang *et al.* (2008). Pictures courtesy of Luis Alvarez, Luru Dai and U. Benjamin Kaupp (Forschungszentrum caesar, Bonn).

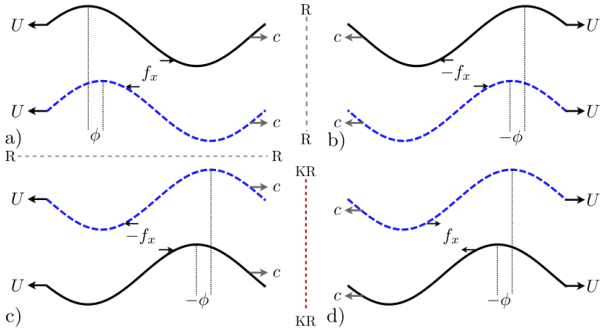

FIG. 39 Swimmers with reflection symmetries by the horizontal and vertical axes cannot phase lock: If a relative force exists in (a), we obtain the forces in (b) and (c) by reflection symmetries (R planes). Applying kinematic reversibility to (c) (KR plane) leads to a force in (d) which is minus the one in (b), indicating that both must be zero. From Elfring and Lauga (2009).

propagating lateral waves with the same wave vector $\boldsymbol{k}$ but a phase shift ϕ, as illustrated in Fig. 39 — and thus corresponding to the two-dimensional system described above, except that the flagella are infinitely long. Suppose that the force f_x between the swimmers acts to decrease the phase difference ϕ, as shown in Fig. 39a. This setup can be reflected at the vertical plane to obtain Fig. 39b, or first at the horizontal plane and then by kinematic reversal to obtain Fig. 39d. Obviously, Figs. 39b and 39d describe exactly the same physical situation. However, the force f_x is reducing the phase difference in Fig. 39b while it is increasing ϕ in Fig. 39d, indicating that $f_x \equiv 0$. Thus, flagella with pure sine waves cannot synchronize.

On the other hand, wave forms which are not front-back symmetric, such as wave forms of sperm with increasing amplitude of the flagellar beat with increasing distance from the head (Friedrich *et al.*, 2010), or flagella which can respond elastically to hydrodynamic forces (Llopis *et al.*, 2013; Yang *et al.*, 2008) (compare Fig. 37), this symmetry argument does not apply, and non-zero forces can appear. A more detailed calculation by Elfring and Lauga (2009) — based on the lubrication approximation valid for small distances between the oscillating sheets — shows that the time evolution of the phase difference between co-swimming cells depends on the nature of the geometrical asymmetry, and that microorganisms can phase-lock into conformations which either minimize (in-phase mode) or maximize (peristaltic mode) energy dissipation. However, the relative arrangement of the two sperm also plays an important role (Llopis *et al.*, 2013). For two sperm with parallel beating planes, even the sign of the interaction can change depending on whether the beating planes are co-planar or are stacked on top of each other.

F. Cilia Synchronization

Motile cilia are abundant in eucaryotic microswimmers to generate propulsion. From *Paramecium* over *Volvox*, cilia are used from unicellular to multicellular organisms to propel fluid across their surface (Afzelius, 1976). In higher organisms and humans, cilia are not only involved in moving mucus in the lungs, but also in embryonic development, e.g. in breaking the left-right symmetry (Cartwright *et al.*, 2004), and in cell signaling (Wang *et al.*, 2006). Already in the 1960s (Sleigh, 1962), it was observed that arrays of cilia beat neither randomly nor synchronously, but in a wave pattern called metachronal wave (MCW).

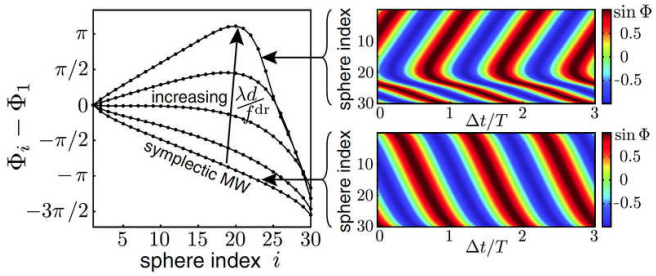

FIG. 40 Phase profile of an array of 30 spheres after 1200 beats. Results are shown for different driving forces f_{dr}, spring constants λ, and distances from the surface d. From Brumley *et al.* (2012).

Several theoretical models have been proposed to explain the hydrodynamic origin of this phenomenon. One approach is to focus on highly simplified systems similar to those presented in Sec. V.A. Either the rotating spheres are placed near a no-slip wall (Brumley *et al.*, 2012; Golestanian *et al.*, 2011; Niedermayer *et al.*, 2008; Uchida and Golestanian, 2010; Vilfan and Jülicher, 2006), or spheres oscillate on a line with different hydrodynamic radii in the two directions of motion (Lagomarsino *et al.*, 2003; Wollin and Stark, 2011). One-dimensional chains of such simplified cilia, can show

metachronal waves under special conditions (Brumley *et al.*, 2012; Lagomarsino *et al.*, 2003; Wollin and Stark, 2011). For *Volvox*, such a rotating-sphere model has been compared in detail with the experimental situation (Brumley *et al.*, 2012). By choosing the right orbit parameters, the experimentally observed metachronal wave pattern can be reproduced. Hence, the simple theoretical approach can help to understand the origin of the nontrivial synchronization with finite phase lag. As it turns out, the presence of a surface already suffices to create a non-zero phase lag (see Sec. V.A).

A second approach uses efficiency arguments. The idea is that the cilia beat has been optimized during evolution to attain maximum efficiency (Eloy and Lauga, 2012; Osterman and Vilfan, 2011). Here, efficiency is defined as minimal power needed to actuate the cilium along a certain path to generate the fluid transport with a velocity v. By simple dimensional analysis (Eloy and Lauga, 2012; Osterman and Vilfan, 2011), or by comparison with a reference flow driven by a constant force density parallel to a wall in a slab of thickness L (the cilium length) (Elgeti and Gompper, 2013a), it has been shown that the efficiency should scale as

$$\epsilon = \frac{Q^2}{P}. \tag{74}$$

where Q is the average volumetric flux and P the average power consumption. This approach yields a well defined cilia stroke (Eloy and Lauga, 2012; Osterman and Vilfan, 2011) that looks very similar to observed cilia strokes, see Fig. 5. This mechanism can be understood as follows. In the fast power stroke, the cilium is nearly fully extended, to reach as far out from the wall as possible, where the fluid flow is least restricted by the presence of the no-slip wall; in contrast, in the slow recovery stroke, the cilium curves and bends sideways to move closely to the wall to generate as little backflow as possible, and at the same time not to bend too much to avoid damage of the microtubule structure. This efficiency argument can be taken one step further to provide a potential explanation of metachronal waves. If all cilia beat synchronously, the whole fluid body flows back and forth with every stroke, which implies a high energy dissipation. Thus the synchronous beat is highly inefficient. By numerically calculating the dissipation for different wave vectors, Osterman and Vilfan (2011) predict antiplectic metachronal waves, see Fig. 41. However, it is not obvious whether global efficiency optimization can be a criterion for the evolution of a collective cilia beat in a system, which should perform well under a variety of environmental conditions.

A third approach is to model cilia as semiflexible filaments with a pre-defined beating mode, and to allow for self-organized metachronal waves by hydrodynamic interactions. This approach has been followed for one-dimensional chains of cilia (Gueron and Levit-Gurevich, 1999; Gueron *et al.*, 1997), for small two-dimensional patches of cilia (Gueron and Levit-Gurevich, 2001), and in a mean-field approach (Guirao and Joanny, 2007). Elgeti and Gompper (2013a) were able to extend this type of approach recently to much larger two-dimensional arrays (up to 60×60 cilia) in a three-dimensional fluid with noise. The beat pattern of a single cilium looks like that of a cilium of paramecium. The beat pattern of an individual cilium can react to the surrounding fluid flow, because the model only imposes time-dependent curvature forces, and employs geometric thresholds for the switch between power and recovery stroke, and *vice versa* (Lindemann and Lesich, 2010). Here, metachronal waves emerge autonomously despite the presence of strong noise (see Fig. 42). Furthermore, this approach allows the study of the appearance of defects, transport efficiency, and wave vectors. In particular, it predicts a large increase in efficiency and propulsion velocity due to metachronal coordination — without the assumption that the system has evolved to optimal efficiency. This efficiency gain is due to the rectification of fluid flow across a ciliated surface, which avoids the oscillatory back-and-forth motion of a perfectly synchonized beat with large viscous energy loss. This result indicates that the efficiency gain by metachronal coordination is a rather universal feature, and does not require an evolutionary optimization strategy. Elgeti and Gompper (2013a) could also demonstrate the presence of defects in the wave pattern of MCWs and characterize some of their properties. It seems that defects assume a form similar to dislocations in two-dimensional crystals (see Fig. 43). However, the defects do not travel with the wave, but remain stationary while the wave passes over them. More detailed studies are needed to fully elucidate the defect dynamics in MCWs.

VI. COLLECTIVE AND COOPERATIVE MOTION

Microswimmers hardly ever swim alone. In nature, the density of microswimmers can reach astonishing densities. Sperm cells are released by the millions to compete in the run for the egg. Coordinated motion is exploited, for example, by spermatozoa of the wood mouse *Apodemus sylvaticusi*, which self-assemble into unique train-like aggregates of hundreds or thousands of cells and thereby significantly increased sperm motility (Hayashi, 1996, 1998; Immler *et al.*, 2007; Moore *et al.*, 2002; Moore and Taggart, 1995; Sivinski, 1984). Bacteria grow by dividing and invading their surroundings together. Artificial microswimmers will only be able to deliver useful quantities of pharmaceuticals or modify material properties when present in large numbers.

In assemblies of motile microorganisms, cooperativity reaches a new level as they exhibit highly organized movements with remarkable large-scale patterns such as

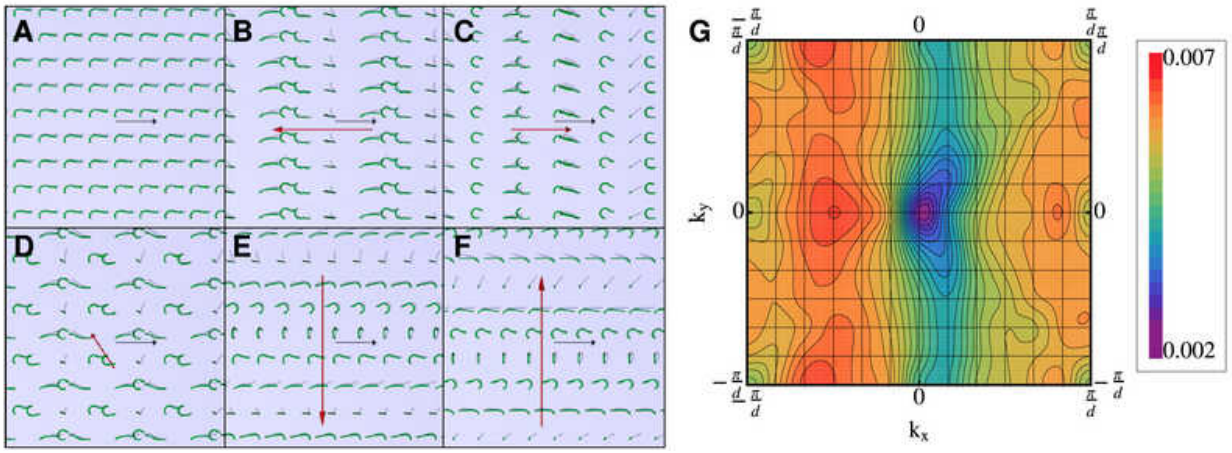

FIG. 41 Optimal solutions at fixed wave vectors for inter-ciliary distance $d = 1.0L$, $N = 20$, where L is the cilium length. (A-F) Optimal solutions for wave vectors (A) $(k_x, k_y) = (0, 0)$, (B) $(-\pi/(2d), 0)$, (C) $(5\pi/(6d), 0)$, (D) $(-2\pi/(3d), \pi/d)$, (E) $(0, -\pi/(3d))$, and (F) $(0, \pi/3d)$. The blue arrow (x-axis) denotes the direction of pumping and the red arrow the wave length and direction of metachronal-wave propagation. (G) Efficiency ϵ_c' (red color represents high efficiency) as a function of the wave vector (k_x, k_y). The maximum efficiency in this case is achieved for $k = (\pi/(2d), 0)$, and antiplectic waves are generally more efficient than symplectic ones. The synchronous solution $(k_x, k_y) = (0, 0)$ represents the global minimum of efficiency. From Osterman and Vilfan (2011).

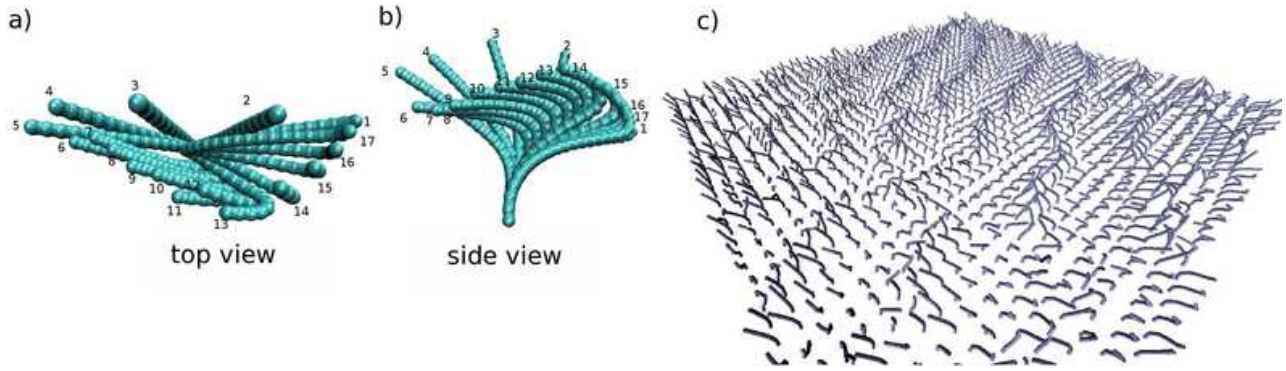

FIG. 42 (a) Side and (b) top view of the beat pattern of the computational cilia model. Subsequent conformations are equally spaced in time. The simulated beat pattern is, for example, similar to the beat pattern of rabbit tracheal cilia in culture medium (Sanderson and Sleigh, 1981). The fast, planar power stroke (frames 1 to 5) continues until a positive curvature threshold in the lower part of the cilium is reached. The cilium then switches to a slow, out-of-plane recovery stroke (frames 6 to 17), which ends when a negative curvature threshold is exceeded. (c) Simulation snapshot of an array of 40×40 beating cilia. Cilia are placed on a square lattice, with lattice constant d_c. The metachronal wave can easily recognized by the lines of fully extended cilia during the power stroke. From Elgeti and Gompper (2013a).

networks, complex vortices, or swarms (Gachelin *et al.*, 2014; Heinrichsen, 1978; Kearns, 2010; Wensink *et al.*, 2012). Such patters are typically displayed by bacteria confined to two dimensions, e.g., *E. coli* or *Bacillus subtilis* involving hundreds to billions of cells (Avron *et al.*, 2004; Darnton *et al.*, 2010; Harshey, 1994; Liu *et al.*, 2000). Flagella are an essential ingredient in swarming of biological cells, as is evident for, e.g., *E. coli*, which produce more flagella and, in addition, elongate and become multinucleate (Copeland and Weibel, 2009; Daniels *et al.*, 2004; Darnton *et al.*, 2010; Harshey, 2003; Kaiser, 2007), which underlines the complexity of the interactions in such assemblies.

The full characterization of the complex dynamical behavior requires an understanding of the underlying (physical) cooperative mechanism on various levels, starting from the interactions of individual cells, fluid-mediated interactions, up to the generic principles of the formation of large-scale patterns.

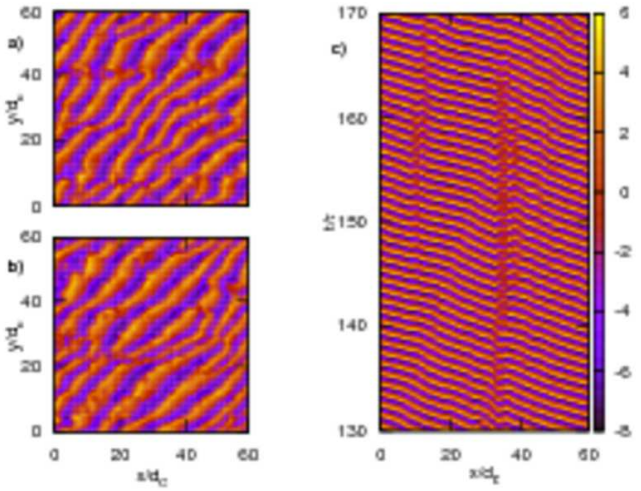

FIG. 43 (a),(b) Phase-field representations of a metachronal wave, for an array of 60 60 cilia, at two times separated by about 40 beats. The color denotes the projected displacement of the tip of a cilium from its base in the direction of the power stroke. (c) Time dependence of a selected line of cilia along the x axis. As a function of time, defects in the metachronal wave pattern appear and disappear. From Elgeti and Gompper (2013a).

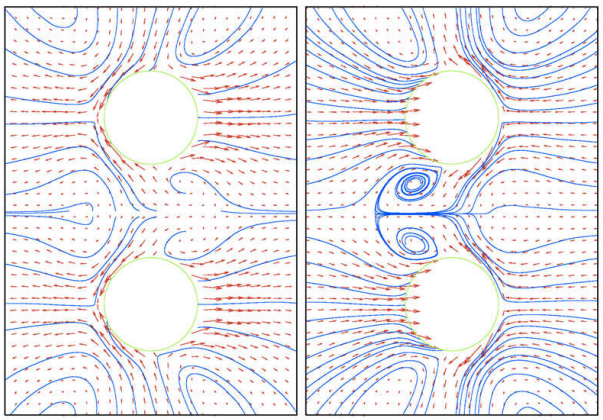

FIG. 44 Velocity fields for fixed parallel pairs of squirmers, for (a) pusher (with $B_2/B_1 = -3$) and (b) puller (with $B_2/B_1 = +3$), with Péclet number Pe = 1155. For definition of mode amplitudes B_1 and B_2 see Eq. 1 in Sec. I. Swimmers move to the right. Streamlines serve as a guide to the eye. Only a fraction of the simulation box is shown. (Due to the finite resolution of the measured velocity field, some streamlines end on the squirmers' surfaces.) From Götze and Gompper (2010).

A. Hydrodynamic Interactions between Microswimmers

Similar as the interactions of microswimmers with a surface, the interaction of two microswimmers at long distances is determined by their dipole flow fields. The dipole approximation predicts that the interactions of microswimmers depends on their relative orientation, and

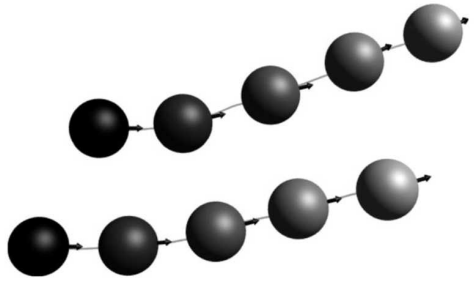

FIG. 45 Trajectories of a pair of initially parallel squirmers (pushers) with Péclet number $Pe = 1155$. Snapshots are shown at fixed time intervals $\Delta tv/\sigma = 1.67$. The initial offset is $\Delta z = 2\sigma$ (perpendicular to direction of motion) and $\Delta x = \sigma$ (parallel), where σ is the squirmer diameter. The instantaneous squirmer orientations are indicated by the arrows. From Götze and Gompper (2010).

that pushers and pullers in equivalent positions and orientations have interactions equal in magnitude and opposite in sign, because their dipole strengths P have opposite signs, see Sec. II.C. This behavior can be understood easily by considering the flow fields of two parallel-swimming pushers or pullers, where pushers attract and pullers repel each other. This effect is also present for shorter distances between the swimmers; the results of mesoscale hydrodynamics simulations of two squirmers (Götze and Gompper, 2010) shown in Fig. 44 demonstrate that for *pushers*, the fast backward flow velocity in the rear part extracts fluid from the gap between the swimmers, and thereby induces attraction (Fig. 44a); in contrast, for *pullers*, the fast backward flow velocity in the front part injects fluid into the gap, and thereby induces repulsion (Fig. 44b).

However, the hydrodynamic interaction between microswimmers is much more complex, because they will usually meet at different relative positions and orientations, and possibly different relative phases of their internal propulsion mechanisms. This gives rise to a rich behavior of attraction, repulsion, or entrainment depending on these parameters (Alexander *et al.*, 2008; Götze and Gompper, 2010; Ishikawa *et al.*, 2006). An example is shown in Fig. 45, which shows the trajectories of two initially parallel oriented pushers, which have a small offset in the forward direction. As a result of this offset, the two squirmers do not attract each other, but rather change their direction of motion together toward the pusher in front. Pullers show the opposite trend and change their direction of motion toward the puller in the back.

B. Generic Model of Flocking

Collective behavior of active bodies is frequently found in microscopic systems such as bacteria (Ben-Jacob *et al.*, 2000; Chen *et al.*, 2012; Gachelin *et al.*, 2013a; Peru-

ani *et al.*, 2012; Sokolov *et al.*, 2007) and synthetic microswimmers (Buttinoni *et al.*, 2013; Ibele *et al.*, 2009; Palacci *et al.*, 2013; Theurkauff *et al.*, 2012; Wang *et al.*, 2013), but also in macroscopic systems such as flocks of birds and schools of fish (Cavagna *et al.*, 2010; Vicsek and Zafeiris, 2012). Despite the very different propulsion mechanisms and interactions in these systems, they all favor alignment of neighboring bodies, thus leading to similar forms of collective behavior.

Therefore, it is natural to look for a model, which is able to capture the generic collective properties of all the various systems of self-propelled particles and organisms. Such a model was proposed in a pioneering work by Vicsek *et al.* (1995b). In this model, now often called the "Vicsek model", N polar point particles move in space with constant magnitude of velocity v_0. The dynamics proceeds in two steps, a streaming step of duration Δt, in which particles move ballistically, and a interaction step, in which particles align their velocity direction with the average direction of motion of their neighbors. In two spatial dimensions, this implies the dynamics for the position $\boldsymbol{r}_i$ and velocity $\boldsymbol{v}_i$ of particle i,

$$\boldsymbol{r}_i(t+\Delta t) = \boldsymbol{r}_i(t) + \boldsymbol{v}_i(t)\Delta t, \tag{75}$$

$$\theta_i(t+\Delta t) \;\; = \langle\theta(t)\rangle_\sigma + \Delta\theta, \tag{76}$$

where θ_i is the angle between $\boldsymbol{v}_i$ and the x-axis of a Cartesian coordinate system, $\langle\theta(t)\rangle_\sigma$ is the average orientation of all particles within a circle of diameter σ. and $\Delta\theta$ is a random noise uniformly distributed in the interval $[-\eta/2, +\eta/2]$. The essential control parameters of the Vicsek model are the particle density ρ, the noise strength η, and the propulsion velocity v_0 in units of $\sigma/\Delta t$.

A numerical investigation of this model by Vicsek *et al.* (1995b) shows a phase transiton with increasing density or decreasing noise strength from a random isotropic phase to an aligned phase, in which particles move collectively in a spontaneously selected direction. This observation of a non-equilibrium phase transition in a system of self-propelled point particles has led to numerous analytical (Baskaran and Marchetti, 2009; Bertin *et al.*, 2009; Golestanian, 2009; Peruani *et al.*, 2008; Ramaswamy *et al.*, 2003; Simha and Ramaswamy, 2002; Toner and Tu, 1995; Toner *et al.*, 2005b) as well as computational (Aldana *et al.*, 2007; Chaté *et al.*, 2008; D'Orsogna *et al.*, 2006; Ginelli *et al.*, 2010; Grégoire and Chaté, 2004; Huepe and Aldana, 2004; Redner *et al.*, 2013; Szabó *et al.*, 2006) studies. A review is provided by Vicsek and Zafeiris (2012).

C. Self-Propelled Rods

When we consider a system of self-propelled particles beyond the phenomenological description of interactions as in the Vicsek model (Vicsek *et al.*, 1995b), the simplest physical interaction which leads to alignment is volume exclusion of rod-like microswimmers and self-propelled rods. Here polar interactions, with alignment in the swimming directions, have to be distinguished from nematic interactions, with aligment independent of the direction of motion. Of particular interest are experiments with elongated self-propelled particles on the microscopic scale in two dimensions, such as motility assays where actin filaments are propelled on a carpet of myosin motor proteins (Harada *et al.*, 1987; Schaller *et al.*, 2010), microtubules propelled by surface-bound dyneins (Sumino *et al.*, 2012), and microswimmers that are attracted to surfaces (as described in Sec. IV).

Self-propelled rods (SPRs) in two dimensions are often modelled as linear chains of (overlapping) beads (Abkenar *et al.*, 2013; Wensink and Löwen, 2008; Yang *et al.*, 2010). Both, models with strict excluded-volume interactions and with a finite overlap energy, which allows rods to cross, have been employed. In the latter case, rod crossing is included to mimic in a two-dimensional simulation the possible escape of rods into the third dimension when two rods collide (like actin filaments or microtubules in a motility assay) (Abkenar *et al.*, 2013).

In such models, self-propulsion of rods leads to enhanced aggregation and cluster formation, as well as to various kinds of ordered phases in Brownian Dynamics simulations (Abkenar *et al.*, 2013; Kraikivski *et al.*, 2006; McCandlish *et al.*, 2012; Peruani *et al.*, 2006; Wensink *et al.*, 2012; Wensink and Löwen, 2008; Yang *et al.*, 2010), as well as in theoretical approaches based on the Smoluchowski equation (Baskaran and Marchetti, 2008a,b; Peruani *et al.*, 2010) and on continuum models in the "hydrodynamic limit" (Baskaran and Marchetti, 2008a,b).

A few simulation snapshots of a two-dimensional system, with different rod number densities ρ, propulsion velocities v_0, and noise levels are shown in Fig. 46, and a corresponding phase diagram in Fig. 47. Here, the importance of propulsion compared to noise is characterized by the Péclet number $Pe = L_{rod}v_0/D_\parallel$, where L_{rod} is the rod length, v_0 the swimming velocity of an isolated swimmer, and $D_\parallel$ the diffusion coefficient in the direction of the instantaneous rod orientation. The phase diagram of Fig. 47 describes a system in which rods interact with a "soft" interaction potential, so that the rods are penetrable at high Péclet numbers (Abkenar *et al.*, 2013). Disordered states, motile clusters, nematic phases, and lane formation are observed. In particular, Fig. 46 displays a phase with a single polar cluster, which is formed at intermediate rod density and not too large Péclet numbers, and a phase with both nematic order and a lane structure where rods moving in opposite directions, which is formed at high rod densities (Abkenar *et al.*, 2013; McCandlish *et al.*, 2012). Near the transition from a disordered state of small- and intermediate-size clusters to an ordered state, the cluster-size distribution obeys a power-law decay, $P(n) \sim n^{-\gamma}$, with an exponent $\gamma \simeq 2$ (Abkenar *et al.*, 2013; Huepe and Aldana, 2004, 2008; Peruani

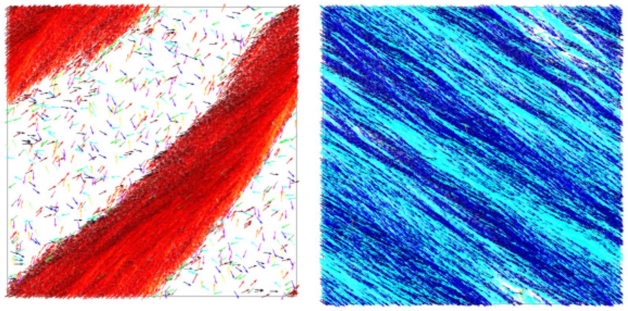

FIG. 46 Simulation snapshots of a system of self-propelled soft rods (with aspect ratio 18) display (left) a giant polar cluster coexisting with a very dilute phase of single swimmers at intermediate density $\rho L_{rod}^2 = 10.2$ and Péclet number $Pe = 25$, and (right) a phase of nematic aligment, in which rods moving in opposite directions self-organize in lanes at high rod density $\rho L_{rod}^2 = 25.5$ and Péclet number $Pe = 75$. Colors indicate rod orientation. From Abkenar *et al.* (2013).

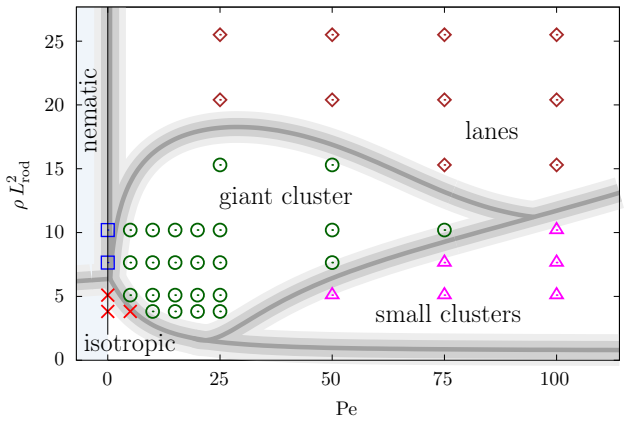

FIG. 47 Phase diagram for self-propelled rods (with aspect ratio 18) as a function of density ρ and Péclet number Pe. The energy barrier is $E = 1.5\, k_B T$; the gray lines are guides to the eye. The region $Pe < 0$ has no physical meaning; it only indicates the presence of isotropic and nematic states for passive rods (with $Pe = 0$). From Abkenar *et al.* (2013).

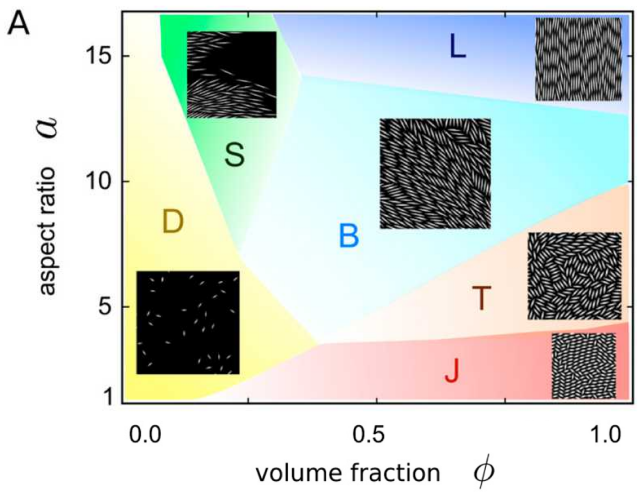

FIG. 48 Phase diagram of self-propelled rods as a function of aspect ratio a and volume fraction ϕ, as obtained from simulations in the absence of noise. Snapshots indicate the phases D-dilute, J-jamming, S-swarming, B-bionematic, T-turbulence, and L-laning. From Wensink *et al.* (2012).

et al., 2006; Yang *et al.*, 2010). This prediction has been compared in detail with experimental results for the clustering of myxobacteria on surfaces (for a mutant which shows polar motion), and very good agreement has been found (Peruani *et al.*, 2012).

The simulation results for systems of self-propelled rods can also be compared with the results of simulations and analytical calculations for the Vicsek model and continuum hydrodynamic models (Peshkov *et al.*, 2012). In the Vicsek and continuum models, polar and nematic interactions have to be distinguished. For polar interactions, moving density waves are predicted (Bertin *et al.*, 2009; Ginelli *et al.*, 2010), while for nematic interactions, high-density bands with rods moving parallel to the band in both directions are expected (Peshkov *et al.*, 2012). Because rods in the simulations are constructed as chains of beads, the dominant contribution of the interaction is nematic, but there is also a polar component (i.e. a somewhat larger probability for parallel than antiparallel alignment after collisions) due to an effective friction resulting from the (weakly) corrugated interaction potential (Abkenar *et al.*, 2013). However, neither with polar nor with nematic interactions do Vicsek and continuum hydrodynamic models predict the polar bands with rod orientation parallel to the band, as shown in Fig. 46a. Thus, clearly more work is needed to elucidate the origin of the differences in the results of models of rod-like particles and with anisotropic interaction potentials and of effective continuum descriptions.

Self-propelled hard rods show also interesting structures in the absence of noise. A phase diagram as a function of aspect ratio a and volume fraction ϕ as obtained from simulations (Wensink *et al.*, 2012) is shown in Fig. 48. At small volume fractions, a dilute phase of single rods is observed for all aspect ratios. For higher volume fractions, several phases of densely packed rods are found, which differ in their internal structure. With increasing aspect ratio, this is a jammed phase of very short rods, a tubulent phase for intermediate aspect ratios, local nematic alignment for somewhat larger aspects ratios, and a swarming phase — which is reminiscent of the giant cluster of noisy rods in Figs. 46(a) and 47 —, and finally a laning phase for long rods with aspect ratio $a \gtrsim 12$ — again similar to the corresponding phase of noisy rods in Figs. 46(b) and 47.

A phase of particular interest is here the "turbulent" phase. This phase is denoted turbulent, because it velocity field displays the typical random swirls and vortices,

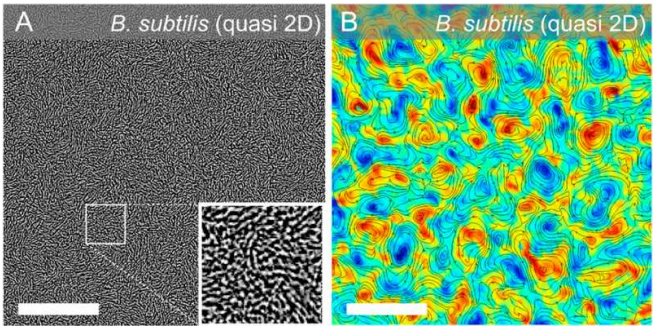

FIG. 49 Snapshots of (A) bacteria arrangements and (B) the extracted vorticity field in the turbulent state of a dense bacterial population on a surface. From Wensink *et al.* (2012).

which are characteristic for high-Reynolds-number turbulence. Such a phase has indeed been observed in dense populations of *Bacillus subtilis*, both at surfaces and in three-dimensional bulk suspensions (Cisneros *et al.*, 2011; Mendelson *et al.*, 1999; Sokolov *et al.*, 2007; Wensink *et al.*, 2012), see Fig. 49a. This phase has also been studied in some detail theoretically and in simulations (Aranson *et al.*, 2007; Dunkel *et al.*, 2013; Wensink *et al.*, 2012; Wolgemuth, 2008). The structure and dynamics of the turbulent phase can be characterized by velocity distributions, velocity increment distributions, and spatial correlation functions (or equivalently structure functions). The results of such an analysis is a typical vortex size R_v, see Fig. 49b, which in two dimensions is about three times the bacterial length L. A comparison with high-Reynolds-number turbulence can be made by calculating the energy spectrum $E(k)$ as a function of the wave vector k, which is closely related to the Fourier transform of the spatial velocity correlation function $\langle \boldsymbol{v}(t,\boldsymbol{r})\cdot\boldsymbol{v}(t,\boldsymbol{r}+R)\rangle$. The main difference between classical and bacterial turbulence is that the energy input occurs in the former case on large length scales, but in the latter case on small scales of the bacterium size L. This has important consequences for the behavior of $E(k)$. In classical turbulence, the famous Kolmogorov-Kraichnan scaling (Kraichnan and Montgomery, 1980) predicts in three dimensions an energy-inertial downward cascade with $E(k) \sim k^{-5/3}$. In two dimensions, there can be both an energy-inertial upward cascade with $E(k) \sim k^{-5/3}$ and an enstrophy-transfer downward cascade with $E(k) \sim k^{-3}$. For bacterial turbulence, similar power-law regimes are found, but the exponents are different. Here, $E(k) \sim k^{+5/3}$ for small k, and $E(k) \sim k^{-8/3}$ for large k (Wensink *et al.*, 2012). Thus, self-sustained bacterial turbulence shares some properties with classical turbulence on small scales, but differs on large scales (Wensink *et al.*, 2012).

D. Active Brownian Spheres

The collective phenomena of Sec. VI.C above and Secs. VI.E and VI.G below are affected by the anisotropic shape and specific interactions between individual cells. These specificities give rise to particular phenomena but may be masked by more general underlying organization principles of microswimmers. Indeed, studies of Brownian, spherical self-propelled colloidal particles without any alignment rule reveal a rich structural and dynamical collective behavior (Bialké *et al.*, 2012; Buttinoni *et al.*, 2013, 2012; Deseigne *et al.*, 2010; Fily *et al.*, 2014b; Fily and Marchetti, 2012; Palacci *et al.*, 2013; Redner *et al.*, 2013; Stenhammar *et al.*, 2014; Theurkauff *et al.*, 2012; Wysocki *et al.*, 2014).

Experiments using either spherical gold/platinum Janus particles (Theurkauff *et al.*, 2012) and polymer spheres with an encapsulated hematite cube (Palacci *et al.*, 2013) in a hydrogen peroxide solution, or carbon-coated colloidal Janus particles dissolved in a near-critical mixture of water and lutidine (Buttinoni *et al.*, 2013) and heated by laser light, yield well-ordered crystalline aggregates at low densities and a phase-transition into large clusters and a dilute gas phase at higher densities in two dimensions. Thereby, the clusters are highly dynamic. Colloids adsorb and evaporate from a cluster, and clusters continuously merge and dissociate (Buttinoni *et al.*, 2013; Theurkauff *et al.*, 2012). The mean cluster size itself depends linearly on the swimming speed (Buttinoni *et al.*, 2013). Large clusters exhibit a well-ordered, crystalline internal structure, which dynamically changes mainly due to movements of dislocations.

In order to elucidate the mechanism governing the aggregation of the active colloids, computer simulations have been performed of a minimal model. Every colloid is described as a point-particle, which is propelled with constant velocity along a body-fixed direction. In addition, it is exposed to a random, white-noise force and the colloid-colloid interaction force, e.g., arising from a Yukawa-like potential. The orientation of the colloid performs a random walk with the respective rotational diffusion coefficient. Hence, no alignment forces or hydrodynamic interactions are taken into account (Bialké *et al.*, 2013, 2012; Buttinoni *et al.*, 2013; Fily *et al.*, 2014b; Fily and Marchetti, 2012; Palacci *et al.*, 2013; Redner *et al.*, 2013; Stenhammar *et al.*, 2014; Wysocki *et al.*, 2014). These simulations indeed yield cluster formation and phase separation solely by propulsion and excluded-volume interactions.

For two-dimensional systems, simulation results are in qualitative agreement with experiments. For monodisperse spheres, clusters are formed with pronounced crystalline order. For polydisperse spheres (Fily *et al.*, 2014b), the high-density phase remains fluid-like, with very little collective dynamics.

Simulations reveal a far richer behavior of selfpro-

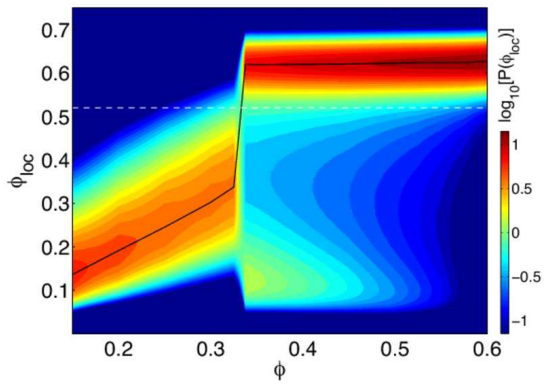

FIG. 50 Probability distribution $P(\phi_l)$ of the local packing fraction ϕ_{loc} as a function of the global packing fraction ϕ for $Pe = 272$. The most probable ϕ_{loc} is indicated by the solid black line. Redrawn from Wysocki *et al.* (2014).

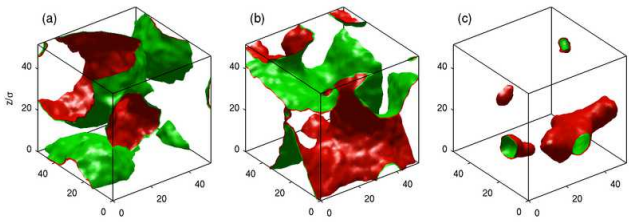

FIG. 51 Snapshots of the gas-liquid interfaces of systems (a,b) just above the clustering transition ($\phi = 0.3375$ and $\phi = 0.4$) and (c) at a high density ($\phi = 0.6$). The red isodensity surfaces corresponds to $\phi_l = 0.54$ and the green to $\phi_l = 0.5$. From Wysocki *et al.* (2014).

pelled spheres in three-dimensions (Stenhammar *et al.*, 2014; Wysocki *et al.*, 2014). As for two-dimensional systems, the system phase separates into a dilute gas-like and dense fluid-like phase above a critical density at a given swimming velocity, or more precisely, Péclet number $Pe = v_0/(\sigma D_r)$, where v_0 is the swimming velocity, σ the colloid diameter, and D_r the rotational diffusion coefficient. Figure 50 presents the probability distribution $P(\phi_l)$ of the local packing fraction ϕ_l as a function of the average density ϕ, where ϕ_l is obtained by Voronoi construction (Rycroft, 2009). Below a critical volume fraction $\phi_c \approx 0.3375$, the system is essentially homogeneous and $P(\phi_l)$ is unimodal. While approaching ϕ_c with increasing ϕ, $P(\phi_l)$ broadens (by formation of transient clusters) and becomes bimodal above ϕ_c. The appearing structures are illustrated in Fig. 51. At low overall density, transient spherical clusters are formed, which turn into a bicontinous structure, whose surfaces is reminiscent of the Schwarz P surface, and finally at high Φ, gas-phase droplets float in a dense matrix (Stenhammar *et al.*, 2014; Wysocki *et al.*, 2014).

The phase diagram for various Péclet numbers and densities is displayed in Fig. 52 (Wysocki *et al.*, 2014). Similar results were obtained by Stenhammar *et al.* (2014). The gray line indicates the spinodal line separating the two-phase region from the one-phase region. Binodal lines are predicted by Stenhammar *et al.* (2014). The existence of the spinodal (and binodal) lines in the phase diagram are in analogy with equilibrium phase diagrams, despite the non-equilibrium character of the present phase separation (Stenhammar *et al.*, 2014). Speck *et al.* (2014) derived an effective Cahn-Hilliard equation for repulsive active Brownian particles on large length and time scales, which underlines the similarities in the phase behavior between passive and active systems.

The phase separation at the higher densities can be understood as follows. The pressure of a hard sphere fluid increases with ϕ and diverges at random close packing for the metastable branch as

$$p_{HS} = -\frac{6k_BT}{\pi\sigma^3}\phi^2\frac{\mathrm{d}}{\mathrm{d}\phi}\ln\left\{\left[(\phi_{RCP}/\phi)^{1/3}-1\right]^3\right\}, \quad (77)$$

according to free volume theory (Kamien and Liu, 2007). Self-propelled particles at low ϕ easily overcome this pressure, coagulate due to their slow-down during collisions (overdamped dynamics) and hence form clusters. The density within the cluster, ϕ_{liq}, adjusts such that $p_{HS}(\phi_{liq})$ balances the active pressure p_a. An initially homogenous system can only phase separate if the active pressure $p_a \sim \gamma_t V_0/\sigma^2$ exceeds $p_{HS}(\phi)$, which leads to a critical line $Pe_c(\phi)$ (spinodal) between the liquid-gas coexistence and the homogenous liquid phase at high ϕ, (cf. Fig. 52); a similar argument has been put forward by Fily *et al.* (2014b) in the context of soft disks.

Remarkably, the local packing fraction in the liquid phase can assume rather large values, deep within the glassy region ($\phi_G \approx 0.58 \leq \phi_{liq} \leq \phi_{RCP} \approx 0.64$) of passive hard spheres (Brambilla *et al.*, 2009; Kamien and Liu, 2007; Pusey and van Megen, 1986). Nevertheless, particles remain mobile and no long-range crystalline order is detected. This indicates a activity-induced shift of the glass-transition point toward higher concentrations, as also discussed by Ni *et al.* (2013), Fily *et al.* (2014b), and Berthier and Kurchan (2013).

Another remarkable aspect is the intriguing dynamics within the liquid phase of the phase-separated system (cf. Fig. 53). Large-scale coherent displacement patterns emerge, with amplitudes and directions strongly varying spatially. In addition, transient swirl- and jet-like structures appear frequently. This is in contrast to two-dimensional systems, which exhibit far less coherent motions. Figure 53(a) shows a swirl spanning the whole cluster while Fig. 53(b) displays a large mobile region moving between the gas-phase regions of the system. Thereby, the fluid density is above the glass transition density $\phi_{liq} \approx 0.62 > \phi_G \approx 0.58$. Spatio-temporal correlation functions for the colloid displacements indicate the existence of a universal finite-size scaling function, which

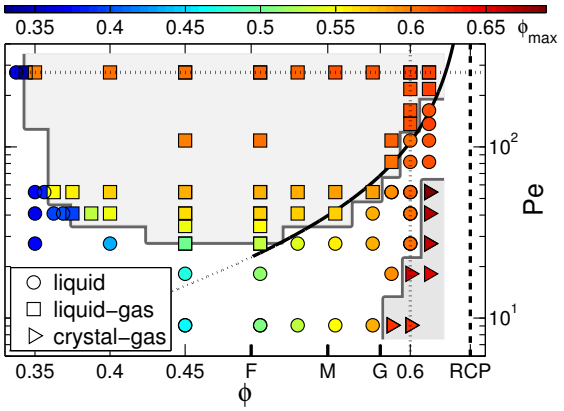

FIG. 52 Phase diagram of an suspension of active Brownian particles. Symbols denote the homogenous liquid phase (○), the gas-liquid coexistence (□) and the crystal-gas coexistence (▷). The equilibrium transition points of hard-spheres for freezing ($\phi_F = 0.494$), melting ($\phi_M = 0.545$), glass-transition point ($\phi_G \approx 0.58$), and random close packing ($\phi_{RCP} \approx 0.64$), are indicated by F, M, G, RCP, respectively. The most probable ϕ_l is color-coded, i.e., in the two-phase region one can read off the density of the dense liquid phase ϕ_{liq}. The solid line marks $Pe_c(\phi)$ which is proportional to Eq. (77). From Wysocki *et al.* (2014).

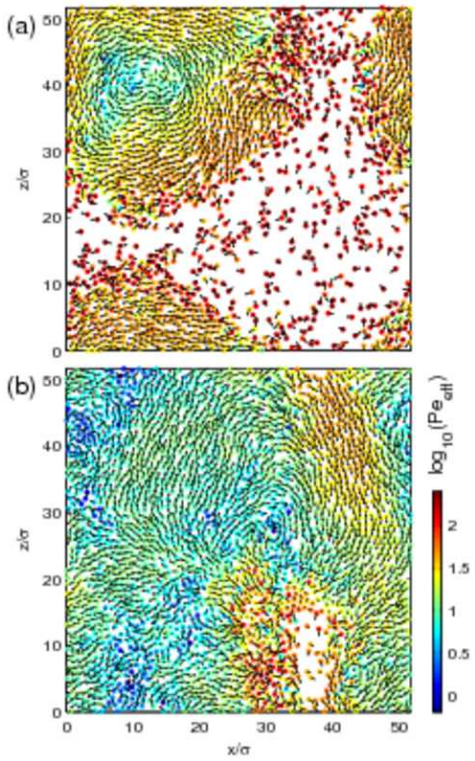

FIG. 53 Collective motion of active Brownian spheres, in the steady state at $Pe = 272$. Snapshots (slices of thickness σ) of a system (a) just above the clustering transition ($\phi = 0.3375$) and (b) at a high concentration ($\phi = 0.6$). Arrows indicate the direction of the displacements over a short lag time. The magnitude is color-coded and is expressed by the effective Péclet number Pe_{eff}. From Wysocki *et al.* (2014).

suggests that the system becomes scale invariant with large-scale correlated fluid flow pattern in the asymptotic limit of large systems (Wysocki *et al.*, 2014). A similar behavior has been discussed in other active systems, however, with a notable polar alignment mechanisms, such as starling flocks (Cavagna *et al.*, 2010) and motile bacteria colonies (Chen *et al.*, 2012).

Various analytical calculations have been performed to achieve a theoretical understanding of the generic principles underneath the propulsion-induced phase transitions (Bialké *et al.*, 2013; Cates and Tailleur, 2013; Fily *et al.*, 2014b; Fily and Marchetti, 2012; Stenhammar *et al.*, 2014, 2013; Tailleur and Cates, 2008; Wittkowski *et al.*, 2014). Adopting an effective continuum theory with a density-dependent effective propulsion speed, Bialké *et al.* (2013) predicted an instability region in the density driving-speed diagram above a lower minimal velocity. A similar approach using the free energy, yields a dynamical equation for the colloid packing fraction. With suitable parameters, this equation qualitatively reproduces the colloid density distributions (see Fig. 51) found in simulations for two- and three-dimensional systems (Stenhammar *et al.*, 2014). Fily *et al.* (2014b) predicted the spinodal lines of their soft, polydisperse active colloids in two dimensions. The success of this approach suggest a remarkable analogy between non-equilibrium and equilibrium phase transitions (Stenhammar *et al.*, 2014).

Finally, we like to discuss the importance of hydrodynamic interactions for the phase behavior of spherical active colloids (Matas-Navarro *et al.*, 2014; Zöttl and Stark, 2014). The study of two-dimensional systems of active discs suggest that aggregation is strongly suppressed by hydrodynamic interactions. On the other hand, a simulation study of a quasi-two-dimensional system of squirmer suspensions confined between two parallel walls, separated by a distance comparable to the swimmer size, indicates that hydrodynamic near-field interactions determine the phase behavior of active particles (Zöttl and Stark, 2014). Near-field hydrodynamics implies an increase of the rotational diffusion, a slow-down of translational motion during collisions, and thereby leads to an enhanced self-trapping and the formation of crystalline clusters, see Fig. 54. This indicates that dimensionality strongly affects the appearing structures in the presence of hydrodynamic interactions, as reflected by the significantly more ordered structures of active particles in a 2D system compared to a quasi-2D system. However, Fig. 54 suggests that hydrodynamic interactions *enhance* phase separation and structure formation compared to bare Brownian interactions, in particular for pullers.

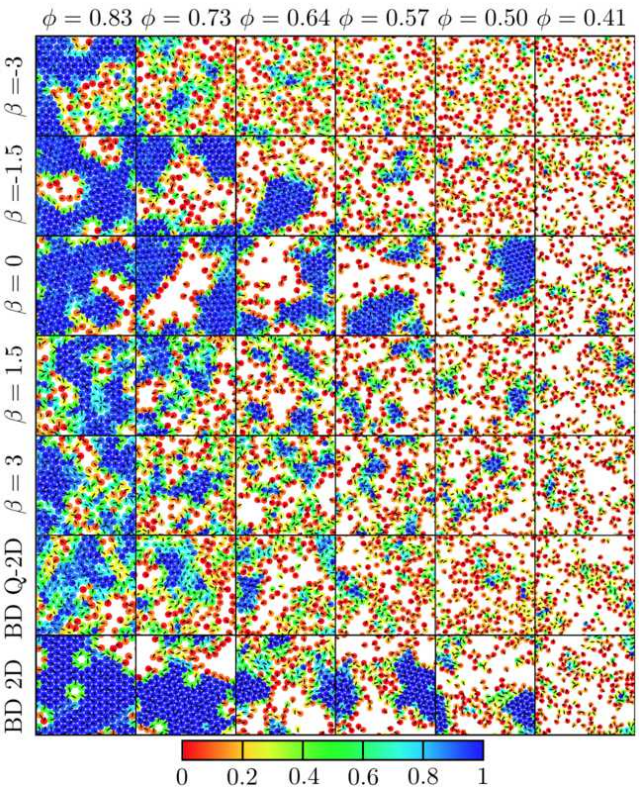

FIG. 54 Typical snapshots of the collective motion and aggregation of squirmers in a quasi-2D geometry, depending on the area fraction ϕ and the squirmer type ($\beta = B_2/B_1$, see Eq. (1). Also shown are snapshots for active Brownian spheres moving in quasi-2D (BD Q-2D), and active Brownian disks moving in 2D (BD 2D). The colors indicate the local bond-orientational order. From Zöttl and Stark (2014).

E. Spermatozoa and Flagella

Experiments in recent years (Hayashi, 1996, 1998; Immler *et al.*, 2007; Moore *et al.*, 2002; Moore and Taggart, 1995; Riedel *et al.*, 2005) have revealed an interesting swarm behavior of sperm at high concentration, for example the distinctive aggregations or "trains of hundreds of wood-mouse sperm (Immler *et al.*, 2007; Moore *et al.*, 2002) or the vortex arrays of swimming sea urchin sperm on a substrate (Riedel *et al.*, 2005). Thus, it is interesting to study the clustering, aggregation, and vortex formation of many sperm cells or flagella.

The results of Secs. VI.A and V.E show that when two sperm with the same beat frequency happen to get close together and swim in parallel, they synchronize and attract through hydrodynamic interactions. The collective behavior of sperm at finite concentrations has mainly been studied numerically so far (Yang *et al.*, 2008). Mesoscale simulations were performed for a two-dimensional system with a number density of about three sperm per squared sperm length. Considering that in real biological systems the beat frequency is not necessary the same for all sperm, beat frequencies ω were selected from a Gaussian distribution with variance $\delta_f = \langle(\Delta\omega)^2\rangle^{1/2}/\langle\omega\rangle$, where $\langle(\Delta\omega)^2\rangle$ is the mean square deviation of the frequency distribution.

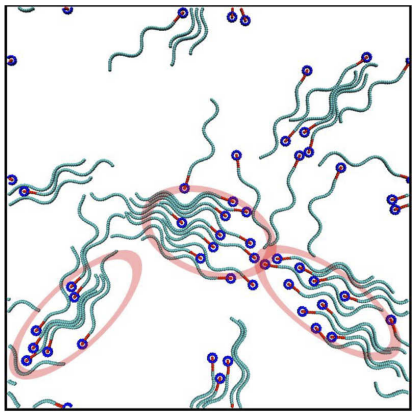

FIG. 55 Snapshot from simulations of 50 symmetric sperm with width $\delta_f = 0.9\%$ of a Gaussian distribution of beating frequencies. The red ellipses indicate large sperm clusters. The black frames show the simulation box. Periodic boundary conditions are employed. From Yang *et al.* (2008).

Fig. 55 shows some snapshots of systems of symmetric sperm with different width δ_f of the Gaussian frequency distribution. For $\delta_f = 0$, once a cluster has formed, it does not disintegrate without a strong external force. A possible way of break-up is by bumping head-on into another cluster. For $\delta_f > 0$, however, sperm cells can leave a cluster after sufficiently long time, since the phase difference to other cells in the cluster increases in time due to the different beat frequencies. At the same time, the cluster size can grow by collecting nearby free sperm or by merging with other clusters. Thus, there is a balance between cluster formation and break-up. Obviously, the average cluster size is smaller for large δ_f than for small δ_f (see Fig. 55).

For $\delta_f = 0$, the average cluster size continues to increase with time. Systems with $\delta_f > 0$ reach a stationary cluster size after about 50 beats. The stationary cluster size is plotted in Fig. 56 as a function of the width δ_f of the frequency distribution. We find a decay with a power law

$$\langle n_c\rangle \sim \delta_f^{-\gamma}, \tag{78}$$

where $\gamma = 0.20 \pm 0.01$. The negative exponent indicates that the cluster size diverges when $\delta_f \to 0$.

Similar power-law behaviors of the cluster size as a function of the noise level, or of the cluster-size distribution itself, have been found for many systems of interacting microswimmers, from self-propelled rods (see Sec. VI.C) to swimming flagella (Yang *et al.*, 2010). Such power laws reflect an underlying universal behavior of self-propelled systems. Indeed, much simpler models with a majority rule to align the velocity of a particle

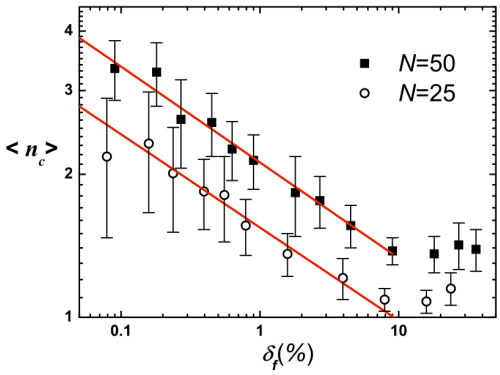

FIG. 56 Dependence of the average stationary cluster size, $\langle n_c \rangle$, on the width of the frequency distribution δ_f. Data are shown for a 50-sperm system (■) and a 25-sperm system (○). The lines indicate the power-law decays $\langle rran_c \rangle = 2.12\,\delta_f^{-0.201}$ (upper) and $\langle n_c \rangle = 1.55\,\delta_f^{-0.196}$ (lower). From Yang *et al.* (2008).

with its neighbors predict such behavior (Vicsek *et al.*, 1995a).

F. Sperm Vortices

Individual sperm cells of many species swim on helical trajectories in the bulk and on circular trajectories at surfaces, as described in Sec. IV.C. When the surface number density ρ_0 of sperm increases beyond a value of about $2000/mm^2$, a new phenomenon is observed (Riedel *et al.*, 2005), which is the formation of sperm vortices, in which several sperm cells together form ring-like arrangements with a diameter d_0 of about $25\mu m$. These vortices are themselves forming a fluid structure with a local hexagonal order, see Fig. 57. The onset of this structure formation corresponds to a dimensionless surface density of $\rho_0 d_0^2 \simeq 1$, which shows that this density is the overlap density of circular trajectories. With increasing surface density, the number of cells in each vortex increases.

The study of this intriguing phenomenon by an extension of the three-dimensional simulations for single sperm described in Sec. IV.C is quite difficult due to the large number of involved microswimmers. Therefore, Yang *et al.* (2014b) have resorted to a two-dimensional description, in which each flagellum is confined to the surface plane, and different flagella interact via excluded-volume interactions. Furthermore, hydrodynamics is either taken into account by resistive-force theory or by a two-dimensional mesoscale hydrodynamics approach. Snapshots and averaged trajectories are shown in Fig. 58.

Both, in experiments and simulations, the correlation function $G_{f,c}(r)$ of the instantaneous centers of the circular trajectories and the variance Δ of the spatial distribution of these centers have been determined (Riedel *et al.*, 2005; Yang *et al.*, 2014b). A comparison of the results leads to the following conclusions. First, the comparison of the simulation results with and without hydrodynamic interactions reveals much weaker correlations with hydrodynamic interactions, see Fig. 59b. The origin of this behavior is that hydrodynamic interactions lead to the synchronization and attraction of sperm swimming together, as discussed in Sec. V.E, but also disrupt the circular paths of sperm belonging to neighboring vortices, which

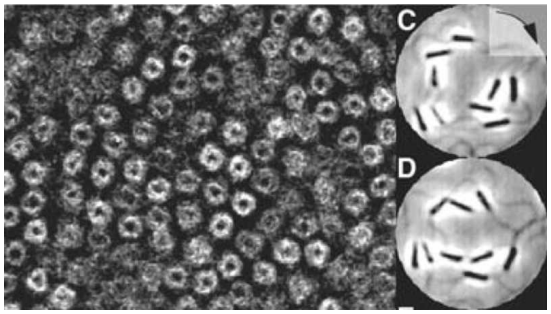

FIG. 57 Pattern of sperm vortices at a wall, which is observed experimentally at high sperm densities. The inset shows the structure of individual vortices, which consists of several sperm. The spatial arrangement of the vortices has local hexagonal order. From Riedel *et al.* (2005).

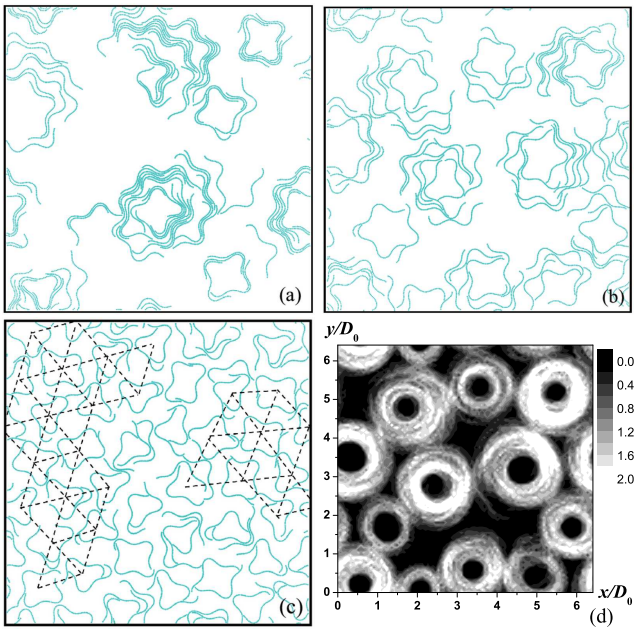

FIG. 58 Snapshots of self-organized vortices of flagella (a) in a mesoscopic fluid, and (b) with anisotropic friction, in both cases with $d_0 = 0.614 L_{fl}$ and $\rho_0 d_0^2 = 2.36$, and (c) with anisotropic friction, and $d_0 = 0.328 L_{fl}$ and $\rho_0 d_0^2 = 0.67$. The dashed lines indicate the local hexagonal order. Here, L_{fl} is the length of the flagellum, d_0 the diameter of the unperturbed circular motion, and ρ_0 the number density of flagella. (d) Normalized flagellum density $\overline{\rho}_f(\boldsymbol{r})$ averaged over a time interval of 30 flagellar beats of the system in (b). From Yang *et al.* (2014b).

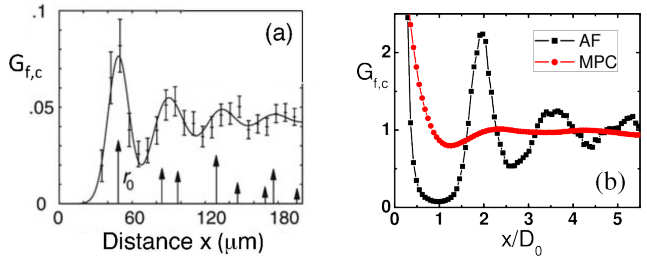

FIG. 59 Pair correlation function of centers of swimming trails of circling sperm near surfaces. (a) Experimental result for sperm number density of $6000/mm^2$, corresponding to about $\rho_0 d_0^2 = 3.75$. Redrawn from Riedel *et al.* (2005). (b) Simulation results for flagella for sperm density $\rho_0 d_0^2 = 2.36$, both with (multi-particle collision dynamics, MPC) and without (anisotropic friction, AF) two-dimensional hydrodynamic interactions. Redrawn from Yang *et al.* (2014b).

move in opposite directions. Second, since the agreement of the simulation results with anisotropic friction only with experimental data is quite reasonable, see Fig. 59a, we conclude that hydrodynamic interactions play a minor role in the vortex formation. However, it should be noticed that both hydrodynamic and excluded-volume interactions are stronger in two than in three spatial dimensions. Therefore, it is conceivable that when the fluid above the surface is taken into account, hydrodynamic interactions contribute significantly to the stabilization of vortex arrays. Third, the order parameter above the overlap concentration is found in simulations and experiments to increase linearly with increasing surface number density. This implies that the characteristic diameter of a vortex hardly changes, but that its mass increases by increasing the number of involved sperm or flagella.

A Vicsek-type model has been designed to capture the dynamics of structure formation of ensembles of circle swimmers in two dimensions (Yang *et al.*, 2014b). Many properties are found to be very similar as for the explicit flagella model described above. Thus, we expect a similar behavior for other circle swimmers in two dimensions, such as the L-shapes colloidal microswimmers of Wensink *et al.* (2014), or of other chiral microswimmers aggregating at surfaces.

G. Swarming of Bacteria

Flagellated microorganisms exhibit collective behavior at a moist surface or in a thin liquid film in form of swarming (Copeland and Weibel, 2009; Darnton *et al.*, 2010; Kearns, 2010; Partridge and Harshey, 2013b). Swarming bacteria show a distinctively different motile behavior than swimming cells (Darnton *et al.*, 2010; Heinrichsen, 1978; Kearns, 2010). Thereby flagella are the most important requirement, but cell-cell interactions also play a major role. Chemotaxis is considered to be of minor importance for swarming compared to physical interactions (Kearns, 2010; Partridge and Harshey, 2013b). During the transition from swimming to swarming cells, the number of flagella increase and the cells become often more elongated by suppression of cell division, i.e., cells become multi- or even hyperflagellated (Darnton *et al.*, 2010; Jones *et al.*, 2004; Kearns, 2010; Stahl *et al.*, 1983). *E. coli* and *Salmonella* bacteria double their length and increase the number of flagella, but the flagellar density remains approximately constant (Copeland *et al.*, 2010; Kearns, 2010; Partridge and Harshey, 2013a,b). The changes for *P. mirabilis* are even more dramatic; their length increases 10 to 50 times and an increase of their flagellum number from fewer than 10 to 5,000 is reported (Copeland and Weibel, 2009; McCarter, 2010; Tuson *et al.*, 2013). As stated by Kearns (2010), neither is the reason known why swarming requires multiple flagella on the cell surface nor is a significant cell elongation required for many bacteria. Aside from a possible amplification of swarming by shape-induced alignment of adjacent cells, elongation associated with the increase in the number of flagella may help to overcome surface friction (Partridge and Harshey, 2013b).

The particular swarming behavior, specifically the role played by flagella, seems to depend on the bacteria density and/or the number of flagella as suggested by experiments on *E. coli* (Copeland *et al.*, 2010; Darnton *et al.*, 2010; Turner *et al.*, 2010) and *B. mirabilis* cells (Jones *et al.*, 2004; Stahl *et al.*, 1983). Studies of systems of lower density *E. coli* bacteria reveal stable cohesive flagella bundles during frequent collisions between cells (Copeland *et al.*, 2010). Thereby, the bundles do not need to be aligned with the body (Turner *et al.*, 2010). Moreover, transient flagella bundles are formed with adjacent cells. For higher density *B. mirabilis* systems, strong bundles between adjacent cells are found.

Since the large-scale patterns in swarming bacteria colonies (Cisneros *et al.*, 2007; Wensink *et al.*, 2012) are determined by cell-cell interactions, it is of fundamental importance to unravel the interactions between flagellated bacteria on the level of individual cells.

VII. OTHER FORMS OF ACTIVE MATTER

A. Mixtures of Filaments and Motor Proteins — Active Gels

An active system, which shares many propeties with suspensions of microswimmers, are mixtures of polar biological filaments with motor proteins. The most prominent examples are actin-myosin and microtubule-kinesin or microtubule-dynein systems. In both cases, the filaments are polar, which means that the motor proteins are walking only in one direction along the filament. In the experiments (Nédélec *et al.*, 1997; Surrey *et al.*, 2001),

clusters of at least two motorproteins are used, which can connect to two filaments simultaneously. The motor proteins move along both filaments until they reach the ends, where they either get stuck or drop off. This leads to many interesting structures like asters, nematic phases, swirls, and vortices.

On the theoretical side, mixtures of filaments and motor proteins have been modeled both on the molecular and on the continuum level. On the molecular level, semiflexible polymers connected by motors with attachment, detachment, and forward-stepping rates have been considered (Gordon *et al.*, 2012; Head *et al.*, 2014, 2011a,b; Kruse *et al.*, 2001; Surrey *et al.*, 2001). On the continuum level, the starting point is the nearly parallel arrangement of long passive filaments in the nematic phase, for which a well-established liquid-crystal description exists (de Gennes and Prost, 1995); additional contributions are then added to this liquid-crytal model to capture the motor activity. These hydrodynamic theories of active gels are equally suited to describe suspensions of microswimmers. Phenomena like swirls and vortices, arrays of vortices and spontaneous collective orientation can all be interpreted in the framework of these continuum approaches (Elgeti *et al.*, 2011; Fuerthauer *et al.*, 2013; Giomi *et al.*, 2011; Kruse *et al.*, 2004; Voituriez *et al.*, 2006). For a comprehensice discussion, we refer to the review articles by Toner *et al.* (2005a), Ramaswamy (2010), and Marchetti *et al.* (2013).

B. Cellular Tissues

Another interesting form of active matter are migrating cellular tissues. A well-studied experimental model of such tissues are Madin-Darby canine kidney (MDCK) cells, as explained in Sec. I. Indeed, similar phenomena as in bacterial turbulence (see Sec. VI.C) can be observed in collectively migrating cellular tissues, however qualitatively different phenomena also emerge. In particular, the adhesion between cells and their active orientation strategy can lead to novel behavior.

When plated on adhesive substrates, the cells move and grow. Similar to the vortices observed in self-propelled rods or bacteria, these cells display swirl structures even when already forming a closed monolayer. As the density increases, this "active liquid" undergoes a glass-like transition, and eventually full dynamical arrest (Angelini *et al.*, 2010, 2011; Basan *et al.*, 2013).

A remarkable feature of growing cellular colonies is that they do not spread by a pressure pushing cells outword, but rather as closed monolayers under tension (Trepat *et al.*, 2009). This tensile state can only be understood if the motility forces against the substrate are considered. Indeed a simple mechanism of alignment of the motility force with the actual velocity can lead to tensile growing states (Basan *et al.*, 2013).

Another feature emerging from the adhesion between the "micro-crawlers" is the formation of growth fingers. A classic experiment is a wound-healing assay. Here, cells are plated confluently around a rubber block. When the block is removed, cells start to migrate into the newly available space. This leads to a fingering instability with the formation of distinct leader cells (Basan *et al.*, 2013; Petitjean *et al.*, 2010; Poujade *et al.*, 2007).

Thus, while not microswimmers, motile epithelial tissues are closely related in some aspects to swimming microorganisms. However, the adhesion among themselves and with the substrate also creates novel features not present in microswimmers.

VIII. SUMMARY AND CONCLUSIONS

In this review article, we have illustrated various physical aspects of locomotion of microswimmers. After an overview of the basic propulsion concepts exploited by biological cells and applied in synthetic systems, we have addressed low Reynolds number hydrodynamics and its implication for the coordinated and concerted motion of individual flagellated cells, and the interaction between cells and colloidal microswimmers, respectively. Alterations in the dynamical behavior due to restricting surfaces have been illuminated along with physical mechanism for surface-capturing. In addition, the complex collective behavior of assemblies of microswimmers has been addressed, which emerges from physical interactions such as hydrodynamics and volume-exclusion interactions due to shape anisotropies or even simply and foremost by their propulsion.

Active systems comprise an exciting and broad range of phenomena. Not all of the aspects could be addressed in this article. Some further characteristics are:

- Biological fluids are typically multicomponent systems containing polymers and other colloid-like objects, which renders them viscoelastic rather than Newtonian. The non-Newtonian environment strongly affects the behavior of the microswimmer and often leads to an enhanced swimming velocity (Chaudhury, 1979; Elfring *et al.*, 2010; Fu *et al.*, 2009; Fulford *et al.*, 1998; Lauga and Powers, 2009; Liu *et al.*, 2011; Miño *et al.*, 2011; Riley and Lauga, 2014; Spagnolie *et al.*, 2013; Zhu *et al.*, 2012).

  By the presence of nonlinear constituitve equations, locomotion in complex fluids overcomes limitations expressed by the scallop theorem (Lauga and Powers, 2009). This is achieved on the one hand by the rate (velocity) dependence by the nonlinear evolution equations, and on the other hand, by the nonlinear rheological properties of the fluid.

- Since microswimmers in the absence of external forces are force- and torque-free, their far-field flow

profile is well described by a force dipole. There are however, some notable exceptions, for example when a microswimmer is not neutrally buoyant or when it is magnetically actuated. The far field of such a swimmers is usually dominated by the Stokeslet. Examples include Volvox algae, which are heavier than water, and thus react to gravity. Their far field was indeed measured to be dominated by the Stockeslet (Drescher *et al.*, 2010). Paramecium is diamagnetic, and thus can be manipulated with magnetic fields, causing external forces and torques (Guevorkian and Valles, 2006a,b).

- Sedimentation in a gravitational field is also strongly affected by active propulsion (Enculescu and Stark, 2011; Tailleur and Cates, 2009). While the density profile is still exponential, the effective temperature is much larger than the real temperature (Tailleur and Cates, 2009), and the particles are polarized in the upwards direction (Enculescu and Stark, 2011) — even in the absence of any hydrodynamic interactions. Theoretical and experimental studies of L-shaped active colloids, i.e., of particles with a chiral shape, demonstrate that the presence of a gravitational field leads to different classes of trajectories, from straight downward and upward motion (gravitaxis) to trochoid-like trajectories (ten Hagen *et al.*, 2014). This suggests that gravitaxis of biological microswimmers opposite to the gravitational field can be entirely due to the interplay of self-propulsion and shape asymmetry, and requires no active steering.

- Exposure to an external flow and confinement, such as in microfluid channels, leads to particular, activity-induced effects. A paradigmatic example is *E. coli* bacteria, which exhibit positive rheotaxis in channel flow, i.e., a rapid and continuous upstream motility (Costanzo *et al.*, 2012, 2014; Fu *et al.*, 2012; Hill *et al.*, 2007; Kaya and Koser, 2012; Nash *et al.*, 2010). Recent measurements for microalgae indicate that they even swim along the vorticity direction in shear flow (Chengala *et al.*, 2013). Moreover, experiments indicate that flow gradients can lead to accumulation and layer formation of gyrotactic phytoplankton (Durham *et al.*, 2009). Strong shear flow can produce large spatial heterogeneities, characterized by cell depletion from low-shear regions due to "trapping" in high-shear regions (Rusconi *et al.*, 2014). This impacts bacterial behavior by hampering chemotaxis and promoting surface attachment.

- The effective viscosity of suspensions of microswimmers in shear or extensional flow depends on the swimming activity, and is therefore different from that of an suspensions of passive particles (Giomi *et al.*, 2010; Gyrya *et al.*, 2011; Hatwalne *et al.*, 2004; Mussler *et al.*, 2013; Rafaï *et al.*, 2010; Saintillan, 2010; Sokolov and Aranson, 2009). Typically, it is found that the effective viscosity increases for pullers and decreases for pushers.

Our understanding of the behavior of the "classical" biological microswimmers (such as sperm, bacteria and algae) dramatically advanced, and many novel microswimmers have been designed in recent years and decades. This opens a route for many new applications of microswimmers , e.g., as microgears (Di Leonardo *et al.*, 2010). What is universal about the swimming behavior (and can thus be described by the hydrodynamic far-field approximation), and what is specific for a certain class of swimmers (like the synchronization of different wave forms of flagella)? How can synthetic microswimmers be designed to react to external stimuli and find their targets? How can the "biological complications" be incorporated into theoretical models? The investigations of these and related questions are challenging and exciting research topics in the future.

Acknowledgement:

With thank Masoud Abkenar, Luis Alvarez, Thorsten Auth, Ingo Götze, Jinglei Hu, Jan Jikeli, U. Benjamin Kaupp, Kristian Marx, Shang Yik Reigh, Marisol Ripoll, Mario Theers, Adam Wysocki, and Yingzi Yang for enjoyable collaborations and stimulating discussions. This work was supported in part by the VW Foundation (VolkswagenStiftung) within the program *Computer Simulation of Molecular and Cellular Bio-Systems as well as Complex Soft Matter*, by the German Science Foundation (DFG) within the priority program *Microswimmers – from single particle motion to collective behavior* (SPP 1726), and by the National Science Foundation under Grant No. NSF PHY11-2515. GG thanks the Kavli Institute of Theoretical Physics (UCSB) for its hospitality during the program "Active Matter: Cytoskeleton, Cells, Tissues and Flocks", where this work was nearly completed.

REFERENCES

Abkenar, Masoud, Kristian Marx, Thorsten Auth, and Gerhard Gompper (2013), "Collective behavior of penetrable self-propelled rods in two dimensions," Phys. Rev. E **88**, 062314.

Afzelius, B A (1976), "A human syndrome caused by immotile cilia," Science **193**, 317.

Aldana, M, V. Dossetti, C. Huepe, V. M. Kenkre, and H. Larralde (2007), "Phase transitions in systems of self-propelled agents and related network models," Phys. Rev. Lett. **98**, 095702.

Alexander, G P, C. M. Pooley, and J. M. Yeomans (2008), "Scattering of low-reynolds-number swimmers," Phys. Rev. E **78**, 045302(R).

Alvarez, Luis, Benjamin M. Friedrich, Gerhard Gompper, and U. Benjamin Kaupp (2014), "The computational sperm cell," Trends Cell Biol. **24**, 198–207.

Angelini, Thomas E, Edouard Hannezo, Xavier Trepat, Jeffrey J. Fredberg, and David A. Weitz (2010), "Cell migration driven by cooperative substrate deformation patterns," Phys Rev Lett **104** (16), 168104.

Angelini, Thomas E, Edouard Hannezo, Xavier Trepat, Manuel Marquez, Jeffrey J. Fredberg, and David A. Weitz (2011), "Glass-like dynamics of collective cell migration," Proc. Natl. Acad. Sci. USA **108** (12), 4714–4719.

Aranson, Igor S, Andrey Sokolov, John O. Kessler, and Raymond E. Goldstein (2007), "Model for dynamical coherence in thin films of self-propelled microorganisms," Phys. Rev. E **75**, 040901(R).

Armitage, J P, and R. M. Macnab (1987), "Unidirectional, intermittent rotation of the flagellum of rhodobacter sphaeroides," J. Bacteriol. **169**, 514.

Avron, J E, O. Gat, and O. Kenneth (2004), "Optimal swimming at low Reynolds numbers," Phys. Rev. Lett. **93**, 186001.

Babu, S B, and H. Stark (2012), "Modeling the locomotion of the african trypanosome using multi-particle collision dynamics," New J. Phys. **14**, 085012.

Basan, Markus, Jens Elgeti, Edouard Hannezo, Wouter-Jan Rappel, and Herbert Levine (2013), "Alignment of cellular motility forces with tissue flow as a mechanism for efficient wound healing," Proc. Natl. Acad. Sci. USA **110**, 2452–2459.

Baskaran, Aparna, and M. Cristina Marchetti (2008a), "Enhanced diffusion and ordering of self-propelled rods," Phys. Rev. Lett. **101**, 268101.

Baskaran, Aparna, and M. Cristina Marchetti (2008b), "Hydrodynamics of self-propelled hard rods," Phys. Rev. E **77**, 011920.

Baskaran, Aparna, and M. Cristina Marchetti (2009), "Statistical mechanics and hydrodynamics of bacterial suspensions," Proc. Natl. Acad. of Sci. USA **106** (37), 15567–15572.

Bayly, Philip V, and Kate S. Wilson (2014), "Equations of interdoublet separation during flagella motion reveal mechanisms of wave propagation and instability," Biophys. J. **107**, 1756.

Bedeaux, D, and P. Mazur (1974), "Brownian motion and fluctuating hydrodynamics," Physica **76**, 247.

Ben-Jacob, Eshel, Inon Cohen, and Herbert Levine (2000), "Cooperative self-organization of microorganisms," Adv. Phys. **49** (4), 395–554.

Bennett, Rachel R, and Ramin Golestanian (2013a), "Emergent run-and-tumble behavior in a simple model of *Chlamydomonas* with intrinsic noise," Phys. Rev. Lett. **110**, 148102.

Bennett, Rachel R, and Ramin Golestanian (2013b), "Phase-dependent forcing and synchronization in the three-sphere model of *chlamydomonas*," New. J. Phys. **15**, 075028.

Berdakin, I, Y. Jeyaram, V. V. Moshchalkov, L. Venken, S. Dierckx, S. J. Vanderleyden, A. V. Silhanek, C. A. Condat, and V. I. Marconi (2013), "Influence of swimming strategy on microorganism separation by asymmetric obstacles," Physical Review E **87** (5), 052702.

Berg, H C, and L. Turner (1990), "Chemotaxis of bacteria in glass-capillary arrays," Biophys. J **58**, 919.

Berg, Howard C (2003), "The rotary motor of bacterial flagella," Annu. Rev. Biochem. **72**, 19–54.

Berg, Howard C (2004), *E. coli in Motion* (Springer, New York).

Berke, Allison P, Linda Turner, Howard C. Berg, and Eric Lauga (2008), "Hydrodynamic attraction of swimming microorganisms by surfaces," Phys. Rev. Lett. **101**, 038102.

Berthier, Ludovic, and Jorge Kurchan (2013), "Non-equilibrium glass transitions in driven and active matter," Nat. Phys. **9**, 310.

Bertin, Eric, Michel Droz, and Guillaume Grégoire (2009), "Hydrodynamic equations for self-propelled particles: microscopic derivation and stability analysis," J. Phys. A: Math. Theor. **42** (44), 445001.

Bialké, Julian, Hartmut Löwen, and Thomas Speck (2013), "Microscopic theory for the phase separation of self-propelled repulsive disks," EPL **103**, 30008.

Bialké, Julian, Thomas Speck, and Hartmut Löwen (2012), "Crystallization in a dense suspension of self-propelled particles," Phys. Rev. Lett. **108**, 168301.

Bird, R B, C. F. Curtiss, R. C. Armstrong, and O. Hassager (1987), *Dynamics of Polymer Liquids*, Vol. 2 (John Wiley & Sons, New York).

Blake, J R (1971a), "A note on the image system for a stokeslet in a no-slip boundary," Proc. Camb. Philos. Soc. **70**, 303–310.

Blake, J R (1971b), "A spherical envelope aproach to ciliary propulsion," J. Fluid Mech. **46**, 199–208.

Bleil, S, D. W. M. Marr, and C. Bechinger (2006), "Field-mediated self-assembly and actuation of highly parallel microfluidic devices," Appl. Phys. Lett. **88**, 263515.

Böhmer, M, Q. Van, I. Weyand, V. Hagen, M. Beyermann, M. Matsumoto, M. Hoshi, E. Hildebrand, and U. B. Kaupp (2005), "Ca^{2+} spikes in the flagellum control chemotactic behavior or sperm," EMBO J. **24**, 2741–2752.

Brambilla, G, D. El Masri, M. Pierno, L. Berthier, L. Cipelletti, G. Petekidis, and A. B. Schofield (2009), "Probing the equilibrium dynamics of colloidal hard spheres above the mode-coupling glass transition," Phys. Rev. Lett. **102**, 085703.

Brennen, C, and H. Winet (1977), "Fluid mechanivs of propulsion by cilia and flagella," Ann. Rev. Fluid Mech. **9**, 339–398.

Brumley, D R, K. Y. Wan, M. Polin, and R. E. Goldstein (2014), "Flagellar synchronization through direct hydrodynamic interactions," eLife **3**, e02750.

Brumley, Douglas R, Marco Polin, Timothy J. Pedley, and Raymond E. Goldstein (2012), "Hydrodynamic synchronization and metachronal waves on the surface of the colonial alga *Volvox carteri*," Phys. Rev. Lett. **109**, 268102.

Bruot, Nicolas, Loïc Damet, Jurij Kotar, Pietro Cicuta, and Marco Cosentino Lagomarsino (2011), "Noise and synchronization of a single active colloid," Phys. Rev. Lett. **107**, 094101.

Buttinoni, Ivo, Julian Bialké, Felix Kümmel, Hartmut Löwen, Clemens Bechinger, and Thomas Speck (2013), "Dynamical clustering and phase separation in suspensions of self-propelled colloidal particles," Phys. Rev. Lett. **110**, 238301.

Buttinoni, Ivo, Giovanni Volpe, Felix Kümmel, Giorgio Volpe, and Clemens Bechinger (2012), "Active brownian motion tunable by light," J. Phys.: Condens. Matter **24**, 284129.

Calladine, C R (1975), "Construction of bacterial flagella," Nature **255**, 121.

Calladine, C R, B. F. Luisi, and J. V. Pratap (2013), "A "mechanistic" explanation of the multiple helical forms adopted by bacterial flagellar filaments," J. Mol. Biol. **425**, 914.

Camalet, S, F. Jülicher, and J. Prost (1999), "Self-organized beating and swimming of internally driven filaments," Phys. Rev. Lett. **82**, 1590–1593.

Cartwright, J H E, O. Piro, and I. Tuval (2004), "Fluid-dynamical basis of the embryonic development of left-right asymmetry in vertebrates," Proc. Natl. Acad. Sci. USA **101**, 7234.

Cates, M E (2012), "Diffusive transport without detailed balance in motile bacteria: does microbiology need statistical physics?" Rep. Prog. Phys. **75**, 042601.

Cates, M E, and J. Tailleur (2013), "When are active Brownian particles and run-and-tumble particles equivalent? consequences for motility-induced phase separation," EPL **101**, 20010.

Cavagna, Andrea, Alessio Cimarelli, Irene Giardina, Giorgio Parisi, Raffaele Santagati, Fabio Stefanini, and Massimiliano Viale (2010), "Scale-free correlations in starling flocks," Proc. Natl. Acad. Sci. USA **107**, 11865–11870.

Chaté, Hugues, Francesco Ginelli, Guillaume Grégoire, and Franck Raynaud (2008), "Collective motion of self-propelled particles interacting without cohesion," Phys. Rev. E **77**, 046113.

Chattopadhyay, Suddhashil, Radu Moldovan, Chuck Yeung, and X. L. Wu (2006), "Swimming efficiency of bacterium *escherichia coli*," Proc. Natl. Acad. Sci. USA **103**, 13712.

Chaudhury, T K (1979), "On swimming in a visco-elastic liquid," J. Fluid Mech. **95**, 189.

Chen, Xiao, Xu Dong, Avraham Be'er, Harry L. Swinney, and H. P. Zhang (2012), "Scale-invariant correlations in dynamic bacterial clusters," Phys. Rev. Lett. **108**, 148101.

Chen, Xiaobing, and Howard C. Berg (2000), "Torque-speed relationship of the flagellar rotary motor of *escherichia coli*," Biophys. J. **78**, 1036.

Chengala, Anwar, Miki Hondzo, and Jian Sheng (2013), "Microalga propels along vorticity direction in a shear flow," Phys. Rev. E **87**, 052704.

Cisneros, L H, R. Cortez, C. Dombrowski, R. E. Goldstein, and J. O. Kessler (2007), "Fliud dynamics of self-propelled microorganisms, from individuals to concentrated populations," Exp. Fluids **73**, 737.

Cisneros, Luis H, John O. Kessler, Sujoy Ganguly, and Raymond E. Goldstein (2011), "Dynamics of swimming bacteria: Transition to directional order at high concentration," Phys. Rev. E **83**, 061907.

Copeland, M F, S. T. Flickinger, H. H. Tucson, and D. B. Weibel (2010), "Studying the dynamics of flagella in multicellular communities of *escherichia coli* by using biarsenical dyes," Appl. Environ. Microbiol. **76**, 1241.

Copeland, M F, and D. B. Weibel (2009), "Bacterial swarming: a model system for studying dynamic self-assembly," Soft Matter **5**, 1174.

Cortez, R, L. Fauci, and A. Medovikov (2005), "The method of regularized Stokeslets in three dimensions: Analysis, validation, and application to helical swimming," J. Fliud Mech. **17**, 031504.

Cosson, J, P. Huitorel, and C. Gagnon (2003), "How spermatozoa come to be confined to surfaces," Cell Motil. Cytoskel. **54**, 56–63.

Costanzo, A, R. Di Leonardo, G. Ruocco, and L. Angelani (2012), "Transport of self-propelling bacteria in microchannel flow," J. Phys.: Condens. Matter **24**, 065101.

Costanzo, Andrea, Jens Elgeti, Thorsten Auth, Gerhard Gompper, and Marisol Ripoll (2014), "Motility-sorting of self-propelled particles in microchannels," EPL **107**, 36003 [1–6].

Crenshaw, H C (1989), "Kinematics of helical motion of microorganisms capable of motion with four degrees of freedom," Biophys. J. **56**, 1029–1035.

Crenshaw, H C (1996), "A new look at locomotion in microorganisms: Rotating and translating," Am. Zool. **36**, 608–618.

Damet, Loic, Giovanni M. Cicuta, Jurij Kotar, Marco Cosentino Lagomarsino, and Pietro Cicuta (2012), "Hydrodynamically synchronized states in active colloidal arrays," Soft Matter **8**, 8672.

Daniels, R, J. Vanderleyden, and J. Michiels (2004), "Quorum sensing and swarming migration in bacteria," FEMS Microbiol. Rev. **28**, 262.

Darnton, N C, and H. C. Berg (2007), "Force-extension measurements on bacterial flagella: Triggering polymorphic transformations," Biophys. J. **92**, 2230.

Darnton, N C, L. Turner, S. Rojevsky, and H. C. Berg (2010), "Dynamics of bacterial swarming," Biophys. J. **98**, 2082.

Darnton, Nicholas C, Linda Turner, Svetlana Rojevsky, and Howard C. Berg (2007), "On torque and tumbling in swimming escherichia coli," J. Bacteriol. **189**, 1756–1764.

de Gennes, P-G, and J. Prost (1995), *The Physics of Liquid Crystals* (Clarendon Press, Oxford).

Denissenko, Petr, Vasily Kantsler, David J. Smith, and Jackson Kirkman-Brown (2012), "Human spermatozoa migration in microchannels reveals boundary-following navigation," Proc. Natl. Acad. Sci. USA **109**, 8007.

Deseigne, Julien, Olivier Dauchot, and Hugues Chaté (2010), "Collective motion of vibrated polar disks," Phys. Rev. Lett. **105**, 098001.

Dhont, J K G (1996), *An Introduction to Dynamics of Colloids* (Elsevier, Amsterdam).

Di Leonardo, R, L. Angelani, D. Dell'arciprete, G. Ruocco, V. Iebba, S. Schippa, M. P. Conte, F. Mecarini, F. De Angelis, and E. Di Fabrizio (2010), "Bacterial ratchet motors," Proc. Natl. Acad. Sci. USA **107**, 9541–9545.

Di Leonardo, R, A. Búzás, L. Kelemen, G. Vizsnyiczai, L. Oroszi, and P. Ormos (2012), "Hydrodynamic synchronization of light driven microrotors," Phys. Rev. Lett. **109**, 034104.

DiLuzio, W R, L. Turner, M. Mayer, P. Garstecki, D. B. Weibel, H. C. Berg, and G. M. Whitesides (2005), "*Escherichia coli* swim on the right-hand side," Nature **435**, 1271.

Doi, M, and S. F. Edwards (1986), *The Theory of Polymer Dynamics* (Clarendon Press, Oxford).

D'Orsogna, M R, Y. L. Chuang, A. L. Bertozzi, and L. S. Chayes (2006), "Self-propelled particles with soft-core interactions: Patterns, stability, and collapse," Phys. Rev. Lett. **96**, 104302.

Drescher, K, J. Dunkel, L. H. Cisneros, S. Ganguly, and R. E. Goldstein (2011), "Fluid dynamics and noise in bacterial cell-cell and cell-surface scattering," Proc. Natl. Acad. Sci. USA **108**, 10940.

Drescher, Knut, Raymond E. Goldstein, Nicolas Michel, Marco Polin, and Idan Tuval (2010), "Direct measurement of the flow field around swimming microorganisms," Phys. Rev. Lett. **105**, 168101.

Drescher, Knut, Kyriacos C. Leptos, Idan Tuval, Takuji Ishikawa, Timothy J. Pedley, and Raymond E. Goldstein (2009), "Dancing volvox: Hydrodynamic bound states of swimming algae," Phys. Rev. Lett. **102**, 168101.

Dreyfus, R, J. Baudry, M. L. Roper, M. Fermigier, H. A. Stone, and J. Bibette (2005), "Microscopic artificial swimmers," Nature **437**, 862–865.

Dunkel, Jörn, Sebastian Heidenreich, Knut Drescher, Henricus H. Wensink, Markus Bär, and Raymond E. Goldstein (2013), "Fluid dynamics of bacterial turbulence," Phys. Rev. Lett. **110**, 228102.

Durham, William M, John O. Kessler, and Roman Stocker (2009), "Disruption of vertical motility by shear triggers formation of thin phytoplankton layers," Science **323**, 1067.

Ebbens, Stephen J, and Jonathan R. Howse (2010), "In pursuit of propulsion at the nanoscale," Soft Matter **6**, 726–738.

Eisenbach, Michael, and Laura C. Giojalas (2006), "Sperm guidance in mammals – an unpaved road to the egg," Nat. Rev. Mol. Cell. Biol. **7**, 276–285.

Elfring, G J, and E. Lauga (2009), "Hydrodynamic phase locking of swimming microorganisms," Phys. Rev. Lett. **103**, 088101.

Elfring, Gwynn J, and Eric Lauga (2011), "Passive hydrodynamic synchronization of two-dimensional swimming cells," Phys. Fluids **23**, 011902.

Elfring, Gwynn J, Shun Pak, and Eric Lauga (2010), "Two-dimensional flagellar synchronization in viscoelastic fluids," J. Fluid Mech. **646**, 505–515.

Elgeti, J, M. E. Cates, and D. Marenduzzo (2011), "Defect hydrodynamics in 2d polar active fluids," Soft Matter **7**, 3177–3185.

Elgeti, J, and G. Gompper (2008), "Hydrodynamics of active mesoscopic systems," in *NIC Symposium 2008*, NIC series, Vol. 39, edited by G. Münster, D. Wolf, and M. Kremer (Neumann Institute for Computing, Jülich) p. 53.

Elgeti, J, and G. Gompper (2009), "Self-propelled rods near surfaces," EPL **85**, 38002 [1–6].

Elgeti, Jens, and Gerhard Gompper (2013a), "Emergence of metachronal waves in cilia arrays," Proc. Natl. Acad. Sci. USA **110**, 4470–4475.

Elgeti, Jens, and Gerhard Gompper (2013b), "Wall accumulation of self-propelled spheres," EPL **101**, 48003 [1–6].

Elgeti, Jens, U. Benjamin Kaupp, and Gerhard Gompper (2010), "Hydrodynamics of sperm cells near surfaces," Biophys. J. **99**, 1018–1026.

Eloy, Christophe, and Eric Lauga (2012), "Kinematics of the most efficient cilium," Phys Rev Lett **109**, 038101.

Enculescu, Mihaela, and Holger Stark (2011), "Active colloidal suspensions exhibit polar order under gravity," Phys. Rev. Lett. **107**, 058301.

Erbe, A, M. Zientara, L. Baraban, C. Kreidler, and P. Leiderer (2008), "Various driving mechanisms for generating motion of colloidal particles," J. Phys. Condens. Matter **20**, 404215.

Español, Pep, Miguel A. Rubio, and Ignacio Zúñiga (1995), "Scaling of the time-dependent self-diffusion coefficient and the propagation of hydrodynamic interactions," Phys. Rev. E **51**, 803.

Fauci, Lisa J, and Robert Dillon (2006), "Biofluidmechanics of reproduction," Annu. Rev. Fluid Mech. **38**, 371–394.

Fily, Yaouen, Aparna Baskaran, and Michael F. Hagan (2014a), "Dynamics of self-propelled particles under strong confinement," Soft Matter **10**, 5609.

Fily, Yaouen, Silke Henkes, and M. Cristina Marchetti (2014b), "Freezing and phase separation of self-propelled disks," Soft Matter **10**, 2132.

Fily, Yaouen, and M. Cristina Marchetti (2012), "Athermal phase separation of self-Propelled particles with no alignment," Phys. Rev. Lett. **108**, 235702.

Flores, H, E. Lobaton, S. Mendez-Diez, S. Tlupova, and R. Cortez (2005), "A study of bacterial flagellar bundling," Bull. Math. Biol. **67**, 137–168.

Foissner, Wilhelm (1998), "An updated compilation of world soil ciliates (protozoa, ciliophora), with ecological notes, new records, and descriptions of new species," European Journal of Protistology **34** (2), 195–235.

Fournier-Bidoz, A, A. C. Arsenault, I. Manners, and G. A. Ozin (2005), "Synthetic self-propelled nanorotors," Chem. Commun. , 441–443.

Friedrich, B M, and F. Jülicher (2012), "Flagellar synchronization independent of hydrodynamic interactions," Phys Rev. Lett. **109**, 138102.

Friedrich, B M, I. H. Riedel-Kruse, J. Howard, and F. Jülicher (2010), "High-precision tracking of sperm swimming fine structure provides strong test of resistive force theory," J. Exp. Biol. **213**, 1226–1234.

Friedrich, Benjamin M, and Frank Jülicher (2007), "Chemotaxis of sperm cells," Proc. Natl. Acad. Sci. **104**, 13256–13261.

Frymier, P D, R. M. Ford, H. C. Berg, and P. T. Cummings (1995), "Three-dimensional tracking of motile bacteria near a solid planar surface," Proc. Nat. Acad. Sci. USA **92**, 6195.

Fu, HC, T.R. Powers, and R. Stocker (2012), "Bacterial rheotaxis," Proc. Natl. Acad. Sci. USA **109**, 4780–4785.

Fu, Henry C, Charles W. Wolgemuth, and Thomas R. Powers (2009), "Swimming speeds of filaments in nonlinearly viscoelastic fluids," Phys. Fluids **21**, 033102.

Fuerthauer, S, M. Strempel, S. W. Grill, and F. Jülicher (2013), "Active Chiral Processes in Thin Films," Phys. Rev. Lett. **110** (4).

Fulford, Glenn R, David F. Katz, and Robert L. Powell (1998), "Swimming of spermatozoa in a linear viscoelastic fluid," Biorheology **35**, 295.

Gachelin, J, A Rousselet, A Lindner, and E Clement (2014), "Collective motion in an active suspension of escherichia coli bacteria," New J. Phys. **16**, 025003.

Gachelin, Jérémie, Gastón Miño, Hélène Berthet, Anke Lindner, Annie Rousselet, and Éric Clément (2013a), "Non-newtonian viscosity of *Escherichia coli* suspensions," Phys. Rev. Lett. **110**, 268103.

Gachelin, Jérémie, Gastón Miño, Hélène Berthet, Anke Lindner, Annie Rousselet, and Éric Clément (2013b), "Non-newtonian viscosity of *escherichia coli* suspensions," Phys. Rev. Lett. **110**, 268103.

Gejji, Richard, Pavel M. Lushnikov, and Mark Alber (2012),

"Macroscopic model of self-propelled bacteria swarming with regular reversals," Phys. Rev. E **85**, 021903.

Geyer, Veikko F, Frank Jülicher, Jonathon Howard, and Benjamin M. Friedrich (2013), "Cell-body rocking is a dominant mechanism for flagellar synchronization in a swimming alga," Proc. Natl. Acad. Sci. USA **110**, 18058–18063.

Ghosh, A, and P. Fischer (2009), "Controlled propulsion of artificial magnetic nanostructured propellers," Nano Lett. **9**, 2243.

Ginelli, Francesco, Fernando Peruani, Markus Bär, and Hugues Chaté (2010), "Large-scale collective properties of self-propelled rods," Phys. Rev. Lett. **104**, 184502.

Giomi, L, L. Mahadevan, B. Chakraborty, and M. F. Hagan (2011), "Excitable patterns in active nematics," Phys. Rev. Lett. **106**, 218101.

Giomi, Luca, Tanniemola B. Liverpool, and M. Cristina Marchetti (2010), "Sheared active fluids: Thickening, thinning, and vanishing viscosity," Phys. Rev. E **81**, 051908.

Goldstein, Raymond E, Marco Polin, and Idan Tuval (2009), "Noise and synchronization in pairs of beating eukaryotic flagella," Phys. Rev. Lett. **103**, 168103.

Goldstein, Raymond E, Marco Polin, and Idan Tuval (2011), "Emergence of synchronized beating during the regrowth of eukaryotic flagella," Phys. Rev. Lett. **107**, 148103.

Golestanian, R (2008), "Three-sphere low-Reynolds-number swimmer with a cargo container," Eur. Phys. J. E **25**, 1.

Golestanian, R (2009), "Anomalous diffusion of symmetric and asymmetric active colloids," Phys. Rev. Lett. **102**, 188305.

Golestanian, R, T. B. Liverpool, and A. Ajdari (2005), "Propulsion of a molecular machine by asymmetric distribution of reaction products," Phys. Rev. Lett. **94**, 220801.

Golestanian, Ramin, Julia M. Yeomans, and Nariya Uchida (2011), "Hydrodynamic synchronization at low reynolds number," Soft Matter **7**, 3074–3082.

Gompper, G, T. Ihle, D. M. Kroll, and R. G. Winkler (2009), "Multi-particle collision dynamics – a particle-based mesoscale simulation approach to the hydrodynamics of complex fluids," Adv. Polym. Sci. **221**, 1–87.

Gordon, Daniel, Anne Bernheim-Groswasser, Chen Keasar, and Oded Farago (2012), "Hierarchical self-organization of cytoskeletal active networks," Phys. Biol. **9**, 026005.

Götze, I O, and G. Gompper (2010), "Flow generation by rotating colloids in planar microchannels," EPL **92**, 64003.

Götze, I O, and G. Gompper (2011), "Dynamic self-assembly and directed flow of rotating colloids in microchannels," Phys. Rev. E **84**, 041921.

Götze, Ingo O, and Gerhard Gompper (2010), "Mesoscale simulations of hydrodynamic squirmer interactions," Phys. Rev. E **82**, 041921 [1–9].

Gray, J, and G. J. Hancock (1955), "The propulsion of sea-urchin spermatozoa," J. Exp. Biol. **32**, 802–814.

Grégoire, Guillaume, and Hugues Chaté (2004), "Onset of collective and cohesive motion," Phys. Rev. Lett. **92**, 025702.

Grzybowsk, Bartosz A, Howard A. Stone, and George M. Whitesides (2000), "Dynamic self-assembly of magnetized, millimetre-sized objects rotating at a liquid-air interface," Nature **405**, 1033–1036.

Guasto, Jeffrey S, Karl A. Johnson, and J. P. Gollub (2010), "Oscillatory flows induced by microorganisms swimming in two dimensions," Phys. Rev. Lett. **105**, 168102.

Gueron, S, and K. Levit-Gurevich (1998), "Computation of the internal forces in cilia: application to ciliary motion, the effects of viscosity, and cilia interactions," Biophys J. **74**, 1658.

Gueron, S, and K. Levit-Gurevich (1999), "Energetic considerations of ciliary beating and the advantage of metachronal coordination," Proc. Nat. Acad. Sci. USA **96** (22), 12240–12245.

Gueron, S, and K. Levit-Gurevich (2001), "A three-dimensional model for ciliary motion based on the internal 9+2 structure," Proc. Biol. Sci **268** (1467), 599–607.

Gueron, Shay, Konstantin Levit-Gurevich, Nadav Liron, and Jacob J. Blum (1997), "Cilia internal mechanism and metachronal coordination as the result of hydrodynamical coupling," Proc. Natl. Acad. Sci. USA **94** (12), 6001.

Guevorkian, Karine, and James M Valles, Jr (2006a), "Aligning paramecium caudatum with static magnetic fields." Biophys J **90**, 3004–3011.

Guevorkian, Karine, and James M Valles, Jr (2006b), "Swimming paramecium in magnetically simulated enhanced, reduced, and inverted gravity environments." Proc Natl Acad Sci U S A **103** (35), 13051–13056.

Guirao, B, and J.F. Joanny (2007), "Spontaneous creation of macroscopic flow and metachronal waves in an array of cilia," Biophys. J. **92**, 1900–1917.

Gyrya, V, K. Lipnikov, I. S. Aranson, and L. Berlyand (2011), "Effective shear viscosity and dynamics of suspensions of micro-swimmers from small to moderate concentrations," J. Math. Biol. **62**, 707–740.

ten Hagen, Borge, Felix Kümmel, Raphael Wittkowski, Daisuke Takagi, Hartmut Löwen, and Clemens Bechinger (2014), "Gravitaxis of asymmetric self-propelled colloidal particles," Nat. Commun. **5**, 4829.

Hancock, G J (1953), "The self-propulsion of microscopic organisms through liquids," Proc. R. Soc. Lond. A **217**, 96.

Harada, Yoshie, Akira Noguchi, Akiyoshi Kishino, and Toshio Yanagida (1987), "Sliding movement of single actin filaments on one-headed myosin filaments," Nature **326**, 805–808.

Harnau, L, R. G. Winkler, and P. Reineker (1996), "Dynamic structure factor of semiflexible macromolecules in dilute solution," J. Chem. Phys. **104**, 6355.

Harshey, R M (1994), "Bees aren't the only ones: swarming in gram-negative bacteria," Mol. Microbiol. **13**, 389.

Harshey, R M (2003), "Bacterial motility on a surface: many ways to a common goal," Annu. Rev. Microbiol. **57**, 249.

Harvey, Cameron W, Mark Alber, Lev S. Tsimring, and Igor S. Aranson (2013), "Continuum modeling of myxobacteria clustering," New J. Phys. **15**, 035029.

Harvey, Cameron W, Faruck Morcos, Christopher R. Sweet, Dale Kaiser, Santanu Chatterjee, Xiaomin Liu, Danny Z. Chen, and Mark Alber (2011), "Study of elastic collisions of *myxococcus xanthus* in swarms," Phys. Biol. **8**, 026016.

Hatwalne, Y, S. Ramaswamy, M. Rao, and R. A. Simha (2004), "Rheology of active-particle suspensions," Phys. Rev. Lett. **92**, 118101.

Hayashi, F (1996), "Insemination through an externally attached spermatophore: bundled sperm and post-copulatory mate guarding by male fishflies," J. Insect Physiol. **42**, 859–866.

Hayashi, F (1998), "Sperm co-operation in the fishfly," Funct. Ecol. **12**, 347–350.

Head, D A, W. J. Briels, and Gerhard Gompper (2014), "Non-equilibrium structure and dynamics in a microscopic model of thin-film active gels," Phys. Rev. E **89**, 032705 [1–11].

Head, David A, W. J. Briels, and Gerhard Gompper (2011a), "Spindles and active vortices in a model of confined filament-motor mixtures," BMC Biophys **4**, 18.

Head, David A, Gerhard Gompper, and Wim J. Briels (2011b), "Microscopic basis for pattern formation and anomalous transport in two-dimensional active gels," Soft Matter **7**, 3116–3126.

Heddergott, Niko, Timothy Krüger, Sujin B. Babu, Ai Wei, Erik Stellamanns, Sravanti Uppaluri, Thomas Pfohl, Holger Stark, and Markus Engstler (2012), "Trypanosome motion represents an adaptation to the crowded environment of the vertebrate bloodstream," PLoS Pathogens **8**, e1003023.

Heinrichsen, J (1978), "Bacterial surface translocation: a survey and a classification," Bacteriol. Rev. **36**, 478.

Hernadez-Ortiz, J P, P. T. Underhill, and M. D. Graham (2009), "Dynamics of confined suspensions of swimming particles," J. Phys.: Condens. Matter **21**, 204107.

Higdon, J J L (1979), "A hydrodynamic analysis of flagellar propulsion," J. Fluid Mech. **90**, 685–711.

Hilfinger, Andreas, Amit K. Chattopadhyay, and Frank Jülicher (2009), "Nonlinear dynamics of cilia and flagella," Phys Rev E Stat Nonlin Soft Matter Phys **79**, 051918.

Hill, J, O. Kalkanci, J. L. McMurry, and H. Koser (2007), "Hydrodynamic surface interactions enable *escherichia coli* to seek efficient routes to swim upstream," Phys. Rev. Lett. **98**, 068101.

Howard, J (2001), *Mechanics of Motor Proteins and the Cytoskeleton* (Sinauer Assoc., Sunderland).

Howse, Jonathan R, Richard A. L. Jones, Anthony J. Ryan, Tim Gough, Reza Vafabakhsh, and Ramin Golestanian (2007), "Self-motile colloidal particles: From directed propulsion to random walk," Phys. Rev. Lett. **99**, 048102.

Huang, C-C, G. Gompper, and R. G. Winkler (2012), "Hydrodynamic correlations in multiparticle collision dynamics fluids," Phys. Rev. E **86**, 056711.

Huang, C-C, G. Gompper, and R. G. Winkler (2013), "Effect of hydrodynamic correlations on the dynamics of polymers in dilute solution," J. Chem. Phys. **138**, 144902.

Huepe, Cristián, and Maximino Aldana (2004), "Intermittency and clustering in a system of self-driven particles," Phys. Rev. Lett. **92**, 168701.

Huepe, Cristián, and Maximino Aldana (2008), "New tools for characterizing swarming systems: a comparison of minimal models," Physica A **387** (12), 2809–2822.

Hyon, Y, T.R. Powers, R. Stocker, and H.C. Fu (2012), "The wiggling trajectories of bacteria," J. Fluid Mech. **705**, 58–76.

Ibele, M, T. E. Mallouk, and A. Sen (2009), "Schooling behavior of light-powered autonomous micromotors in water," Angew. Chem. Int. Ed. Engl. **48**, 3308–3312.

Immler, S, H. D. M. Moore, W. G. Breed, and T. R. Birkhead (2007), "By hook or by crook? morphometry, competition and cooperation in rodent sperm," PLoS ONE **2**, e170.

Ishikawa, T, and T. J. Pedley (2008), "Coherent structures in monolayers of swimming particles," Phys. Rev. Lett. **100**, 088103.

Ishikawa, T, G. Sekiya, Y. Imai, and T. Yamaguchi (2007), "Hydrodynamic interactions between two swimming bacteria," Biophys. J. **93**, 2217–2225.

Ishikawa, T, M. P. Simmonds, and T. J. Pedley (2006), "Hydrodynamic interaction of two swimming model microorganisms," J. Fluid Mech. **568**, 119–160.

Ishikawa, Takuji (2009), "Suspension biomechanics of swimming microbes," J. R. Soc. Interface **6**, 815–834.

Ishimoto, Kenta, and Eamonn A. Gaffney (2013), "Squirmer dynamics near a boundary," Phys. Rev. E **88**, 062702.

Janssen, P J A, and M. D. Graham (2011), "Coexistence of tight and loose bundled states in a model of bacterial flagellar dynamics," Phys. Rev. E **84**, 011910.

Jiang, H-R, N. Yoshinaga, and M. Sano (2010), "Active motion of janus particle by self-thermophoresis in defocused laser beam," Phys. Rev. Lett. **105**, 268302.

Johnson, R E (1980), "An improved slender-body theory for stokes flow," J. Fluid Mech. **99**, 411.

Johnson, R E, and C. J. Brokaw (1979), "Flagellar hydrodynamics—comparison between resistive-force theory and slender-body theory," Biophys. J. **25**, 113.

Jones, B V, R. Young, E. Mahenthiralingam, and D. J. Stickler (2004), "Ultrastructure of *proteus mirabilis* swarmer cell rafts and role of swarming in catheter-associated urinary tract infection," Infect. Immun. **72**, 3941.

Jones, Dan (2008), "Engines of evolution," New Scientist **197**, 40–43.

Jülicher, F, and J. Prost (1997), "Spontaneous oscillations of collective molecular motors," Phys. Rev. Lett. **78**, 4510–4513.

Kaiser, A, H. H. Wensink, and H. Löwen (2012), "How to capture active particles," Phys Rev Lett **108** (26), 268307.

Kaiser, D (2003), "Coupling cell movement to multicellular development in myxobacteria," Nat. Rev. Microbiol. **1**, 45–54.

Kaiser, D (2007), "Bacterial swarming: a re-examination of cell-movement patterns," Curr. Biol. **17**, R561.

Kamien, Randall D, and Andrea J. Liu (2007), "Why is random close packing reproducible?" Phys. Rev. Lett. **99**, 155501.

Kantsler, Vasily, Jrn Dunkel, Marco Polin, and Raymond E. Goldstein (2013), "Ciliary contact interactions dominate surface scattering of swimming eukaryotes," Proc. Natl. Acad. Sci. USA **110**, 1187.

Kapral, R (2008), "Multiparticle collision dynamics: Simulation of complex systems on mesoscales," Adv. Chem. Phys. **140**, 89–146.

Kaupp, U Benjamin, N. D. Kashikar, and Ingo Weyand (2008), "Mechanisms of sperm chemotaxis," Annu. Rev. Physiol. **70**, 93–117.

Kaupp, U Benjamin, Johannes Solzin, Eilo Hildebrand, Joel E. Brown, Annika Helbig, Volker Hagen, Michael Beyermann, Francesco Pampaloni, and Ingo Weyand (2003), "The signal flow and motor response controlling chemotaxis of sea urgin sperm," Nat. Cell Biol. **5**, 109–117.

Kawska, Agnieszka, Kévin Carvalho, John Manzi, Rajaa Boujemaa-Paterski, Laurent Blanchoin, Jean-Louis Martiel, and Cécile Sykes (2012), "How actin network dynamics control the onset of actin-based motility," Proc. Natl. Acad. Sci. USA **109** (36), 14440–14445.

Kaya, T, and H. Koser (2012), "Direct upstream motility in *escherichia coli*," Biophys. J. **102**, 1514.

Kearns, D B (2010), "A field guide to bacterial swarming motility," Nat. Rev. Microbiol. **8**, 634.

Kim, Areum, Chengxin Zhou, Neema Lakshman, and W. Matthew Petroll (2012), "Corneal stromal cells use both high- and low-contractility migration mechanisms in 3-d collagen matrices," Exp. Cell Res. **318**, 741–752.

Kim, M, and T. R. Powers (2004), "Hydrodynamic interactions between rotating helices," Phys. Rev. E **69**, 061910.

Kim, M J, J. C. Bird, A. J. Van Parys, K. S. Breuer, and

T. R. Powers (2003), "A macroscopic scale model of bacterial flagellar bundling," Proc. Natl. Acad. Sci. USA **100**, 15481.

Knight-Jones, E W (1954), "Relations between metachronism and the direction of the ciliary beat," Q. J. Microsc. Sci. **95**, 503.

Koch, Donald L, and Ganesh Subramanian (2011), "Collective hydrodynamics of swimming microorganisms: Living fluids," Ann. Rev. Fluid Mech. **43**, 637.

Kotar, Jurij, Luke Debono, Nicolas Bruot, Stuart Box, David Phillips, Stephen Simpson, Simon Hanna, and Pietro Cicuta (2013), "Optimal hydrodynamic synchronization of colloidal rotors," Phys. Rev. Lett. **111**, 228103.

Kotar, Jurij, Marco Leoni, Bruno Bassetti, Marco Cosentino Lagomarsino, and Pietro Cicuta (2010), "Hydrodynamic synchronization of colloidal oscillators," Proc. Natl. Acad. Sci. USA **107**, 7669–7673.

Koumakis, N, and R. Di Leonardo (2013), "Stochastic hydrodynamic synchronization in rotating energy landscapes," Phys. Rev. Lett. **110**, 174103.

Kraichnan, R H, and D. Montgomery (1980), "Two-dimensional turbulence," Rep. Prog. Phys. **43**, 547–619.

Kraikivski, Pavel, Reinhard Lipowsky, and Jan Kierfeld (2006), "Enhanced ordering of interacting filaments by molecular motors," Phys. Rev. Lett. **96**, 258103.

Kruse, K, S. Camalet, and F. Jülicher (2001), "Self-propagating patterns in active filament bundles," Phys. Rev. Lett. **87**, 138101.

Kruse, K, J. F. Joanny, F. Jülicher, J. Prost, and K. Sekimoto (2004), "Asters, vortices, and rotating spirals in active gels of polar filaments," Phys. Rev. Lett. **92** (7), 078101.

Lagomarsino, M Cosentino, P. Jona, and B. Bassetti (2003), "Metachronal waves for deterministic switching two-state oscillators with hydrodynamic interaction," Phys. Rev. E **68**, 021908.

Lauga, E (2011), "Life around the scallop theorem," Soft Matter **7**, 3060.

Lauga, E, W. R. DiLuzio, G. M. Whitesides, and H. A. Stone (2006), "Swimming in circles: motion of bacteria near solid boundaries," Biophys. J. **90**, 400.

Lauga, E, and R. E. Goldstein (2012), "Dancing of the microswimmers," Phys. Today **65**, 30.

Lauga, Eric, and Thomas R. Powers (2009), "The hydrodynamics of swimming microorganisms," Rep. Prog. Phys. **72**, 096601.

Lemelle, L, J.-F. Palierne, E. Chatre, and C. Place (2010), "Counterclockwise circular motion of bacteria swimming at the air-liquid interface," J. Bacteriol. **192**, 6307.

Lenz, Peter, and Andrey Ryskin (2006), "Collective effects in ciliar arrays," Phys. Biol. **3** (4), 285.

Leptos, Kyriacos C, Kirsty Y. Wan, Marco Polin, Idan Tuval, Adriana I. Pesci, and Raymond E. Goldstein (2013), "Antiphase synchronization in a flagellar-dominance mutant of *Chlamydomonas*," Phys. Rev. Lett. **111**, 158101.

Lhermerout, Romain, Nicolas Bruot, Giovanni M Cicuta, Jurij Kotar, and Pietro Cicuta (2012), "Collective synchronization states in arrays of driven colloidal oscillators," New J. Phys. **14**, 105023.

Li, Guanglai, Lick-Kong Tam, and Jay X. Tang (2008), "Amplified effect of Brownian motion in bacterial near-surface swimming," Proc. Natl Acad. Sci. USA **105** (47), 18355.

Li, Guanglai, and Jay X. Tang (2009), "Accumulation of microswimmers near a surface mediated by collision and rotational brownian motion," Phys. Rev. Lett. **103**, 078101.

Lighthill, J (1976), "Flagellar hydrodynamics—The John von Neumann Lecture 1975," SIAM Rev. **18**, 161.

Lighthill, M J (1952), "On the squirming motion of nearly spherical deformable bodies through liquids at very small reynolds numbers," Commun. Pure Appl. Math. **5**, 109.

Lindemann, C B (1994), "A geometric clutch hypothesis to explain oscillations of the axoneme of cilia and flagella," J. Theor. Biol. **168**, 175–189.

Lindemann, Charles B (2014), "Engaging the "clutch" to move forward," Biophys. J. **107**, 1487–1488.

Lindemann, Charles B, and Kathleen A. Lesich (2010), "Flagellar and ciliary beating: the proven and the possible," J. Cell Sci. **123**, 519–528.

Liu, Bin, Thomas R. Powers, and Kenneth S. Breuer (2011), "Force-free swimming of a model helical flagellum in viscoelastic fluids," Proc. Natl. Acad. Sci. USA **108**, 19516.

Liu, J-K, G.-H. Deng, Z.-T. Yuan, and D. J. Liu (2000), "Turbulence under the microscope," J. Biol. Phys. **26**, 77.

Llopis, I, and I. Pagonabarraga (2008), "Hydrodynamic regimes of active rotators at fluid interfaces," Eur. Phys. J. E **26**, 103–113.

Llopis, I, I. Pagonabarraga, M. Cosentino Lagomarsino, and C. P. Lowe (2013), "Cooperative motion of intrinsic and actuated semiflexible swimmers," Phys. Rev. E **87**, 032720.

Lopez, Diego, and Eric Lauga (2014), "Dynamics of swimming bacteria at complex interfaces," Phys. Fluids **26**, 071902.

Machemer, H (1972), "Ciliary activity and the origin of metachrony in paramecium: Effects of increased viscosity," J. Exp. Biol. **57**, 239–259.

Macnab, R M (1977), "Bacterial flagella rotating in bundles: A study in helical geometry," Proc. Natl. Acad. Sci. USA **74**, 221.

Magariyama, Y, S. Sugiyama, K. Muramoto, I. Kawagishi, Y. Imae, and S. Kudo (1995), "Simultaneous measurement of bacterial flagellar rotation rate and swimming speed," Biophys. J. **69**, 2154.

Manghi, Manoel, Xaver Schlagberger, and Roland R. Netz (2006), "Propulsion with a rotating elastic nanorod," Phys. Rev. Lett. **96**, 068101.

Marchetti, M C, J. F. Joanny, S. Ramaswamy, T. B. Liverpool, J. Prost, Madan Rao, and R. Aditi Simha (2013), "Hydrodynamics of soft active matter," Rev. Mod. Phys. **85**, 1143.

Matas-Navarro, Ricard, Ramin Golestanian, Tanniemola B. Liverpool, and Suzanne M. Fielding (2014), "Hydrodynamic suppression of phase separation in active suspensions," Phys. Rev. E **90**, 032304.

McCandlish, Samuel R, Aparna Baskaran, and Michael F. Hagan (2012), "Spontaneous segregation of self-propelled particles with different motilities," Soft Matter **8**, 2527–2534.

McCarter, L L (2010), "Bacterial acrobatics on a surface: Swirling packs, collisions, and reversals during swarming," J. Bacteriol. **192**, 3246.

Mei, Y F, A. A. Solovev, S. Sanchez, and O. G. Schmidt (2011), "Rolled-up nanotech on polymers: from basic perception to self-propelled catalytic microengines," Chem. Soc. Rev. **40**, 2109.

Mendelson, NH, A Bourque, K Wilkening, KR Anderson, and JC Watkins (1999), "Organized cell swimming motions in Bacillus subtilis colonies: Patterns of short-lived whirls and jets," J. Bacteriol. **181** (2), 600–609.

Miño, Gastón, Thomas E. Mallouk, Thierry Darnige, Mauri-

cio Hoyos, Jeremi Dauchet, Jocelyn Dunstan, Rodrigo Soto, Yang Wang, Annie Rousselet, and Eric Clement (2011), "Enhanced diffusion due to active swimmers at a solid surface," Phys. Rev. Lett. **106**, 048102.

Molaei, Mehdi, Michael Barry, Roman Stocker, and Jian Sheng (2014), "Failed escape: Solid surfaces prevent tumbling of *escherichia coli*," Phys. Rev. Lett. **113**, 068103.

Moore, H D M, K. Dvoráková, N. Jenkins, and W. G. Breed (2002), "Exceptional sperm cooperation in the wood mouse," Nature **418**, 174–177.

Moore, H D M, and D. A. Taggart (1995), "Sperm pairing in the opossum increases the efficiency of sperm movement in a viscous environment," Biol. Reprod. **52**, 947–953.

Mora, Thierry, Howard Yu, and Ned S. Wingreen (2009), "Modeling torque versus speed, shot noise, and rotational diffusion of the bacterial flagellar motor," Phys. Rev. Lett. **103**, 248102.

Mussler, Matthias, Salima Rafaï, Philippe Peyla, and Christian Wagner (2013), "Effective viscosity of non-gravitactic chlamydomonas reinhardtii microswimmer suspensions," EPL **101**, 54004.

Najafi, Ali, and Ramin Golestanian (2004), "Simple swimmer at low reynolds number: Three linked spheres," Phys. Rev. E **69**, 062901.

Nash, R W, R. Adhikari, J. Tailleur, and M. E. Cates (2010), "Run-and-tumble particles with hydrodynamics: Sedimentation, trapping, and upstream swimming," Phys. Rev. Lett. **104**, 258101.

Nédélec, F J, T. Surrey, A. C. Maggs, and S. Leibler (1997), "Self-organization of microtubules and motors," Nature **389**, 305–308.

Ni, Ran, Martien A. Cohen Stuart, and Marjolein Dijkstra (2013), "Pushing the glass transition towards random close packing using self-propelled hard spheres," Nat. Commun. **4**, 2704.

Niedermayer, Thomas, Bruno Eckhardt, and Peter Lenz (2008), "Synchronization, phase locking, and metachronal wave formation in ciliary chains," Chaos **18** (3), 037128.

Okamoto, Ken-Ichi, and Yasuo Nakaoka (1994), "Reconstitution of metachronal waves in ciliated cortical sheets of paramecium ii. asymmetry of the ciliary movements," J. Exp. Biol. **192**, 73–81.

Or, D, B.F. Smets, J.M. Wraith, A. Dechesne, and S.P. Friedman (2007), "Physical constraints affecting bacterial habitats and activity in unsaturated porous media – a review," Advances in Water Resources **30**, 1505–1527.

Osterman, Natan, and Andrej Vilfan (2011), "Finding the ciliary beating pattern with optimal efficiency," Proc. Natl. Acad. Sci. USA **108**, 15727–15732.

Ozin, Geoffrey A, Ian Manners, Sébastien Fournier-Bidoz, and André Arsenault (2005), "Dream nanomachines," Adv. Mater. **17**, 3011–3018.

Pagonabarraga, Ignacio, and Isaac Llopis (2013), "The structure and rheology of sheared model swimmer suspensions," Soft Matter **9**, 7174–7184.

Palacci, J, S. Sacanna, A. P. Steinberg, D. J. Pine, and P. M. Chaikin (2013), "Living crystals of light-activated colloidal surfers," Science **339**, 936–940.

Partridge, J D, and R. M. Harshey (2013a), "More than motility: *Salmonella* flagella contribution to overriding friction and facilitating colony hydration during swarming," J. Bacteriol. **195**, 919.

Partridge, J D, and R. M. Harshey (2013b), "Swarmming: flexible roaming plans," J. Bacteriol. **195**, 909.

Paxton, W, S. Sundararajan, T. Mallouk, and A. Sen (2006), "Chemical locomotion," Angew. Chem. Int. Ed. **45**, 5420.

Paxton, W F, K. C. Kistler, C. C. Olmeda, A. Sen, S. K. St. Angelo, Y. Cao, T. E. Mallouk, P. E. Lammert, and V. H. Crespi (2004), "Catalytic nanomotors: autonomous movement of striped nanorods," J. Am. Chem. Soc. **126**, 13424.

Peruani, F, L Schimansky-Geier, and M Bär (2010), "Cluster dynamics and cluster size distributions in systems of self-propelled particles," Eur. Phys. J. Special Topics **191** (1), 173–185.

Peruani, Fernando, Andreas Deutsch, and Markus Bär (2006), "Nonequilibrium clustering of self-propelled rods," Phys. Rev. E **74**, 030904(R).

Peruani, Fernando, Andreas Deutsch, and Markus Bär (2008), "A mean-field theory for self-propelled particles interacting by velocity alignment mechanisms," Eur. Phys. J. Special Topics **157** (1), 111–122.

Peruani, Fernando, Jörn Starruss, Vladimir Jakovljevic, Lotte Søgaard-Andersen, Andreas Deutsch, and Markus Bär (2012), "Collective motion and nonequilibrium cluster formation in colonies of gliding bacteria," Phys. Rev. Lett. **108**, 098102.

Peshkov, Anton, Igor S. Aranson, Eric Bertin, Hugues Chaté, and Francesco Ginelli (2012), "Nonlinear field equations for aligning self-propelled rods," Phys. Rev. Lett. **109**, 268701.

Petitjean, L, M Reffay, E Grasland-Mongrain, M Poujade, B Ladoux, A Buguin, and P Silberzan (2010), "Velocity fields in a collectively migrating epithelium," Biophys. J. **98** (9), 1790–800.

Pikovsky, A, M. Rosenblum, and J. Kurths (2002), *Synchronization: A Universal Concept in Nonlinear Science* (Cambridge University Press).

Platzer, J, W. Sterr, M. Hausmann, and R. Schmitt (1997), "Three genes of a motility operon and their role in flagellar rotary speed variation in *Rhizobium meliloti*," J. Bacteriol. **179**, 6391–6399.

Polin, M, Tuval I, K. Drescher, J. P. Gollub, and R. E. Goldstein (2009), "Chlamydomonas swims with two 'gears' in a eukaryotic version of run-and-tumble locomotion," Science **325**, 487.

Polotzek, K, and B. M. Friedrich (2013), "A three-sphere swimmer for flagellar synchronization," New. J. Phys. **15**, 045005.

Popescu, M N, S. Dietrich, and G. Oshanin (2009), "Confinement effects on diffusiophoretic self-propellers," J. Chem. Phys. **130**, 194702.

Popescu, M N, S. Dietrich, M. Tasinkevych, and J. Ralston (2010), "Phoretic motion of spheroidal particles due to self-generated solute gradients," Eur. Phys. J. E **31**, 351–367.

Poujade, M, E. Grasland-Mongrain, A. Hertzog, J. Jouanneau, P. Chavrier, B. Ladoux, A. Buguin, and P. Silberzan (2007), "Collective migration of an epithelial monolayer in response to a model wound," Proc. Natl. Acad. Sci. USA **104**, 15988–15993.

Prost, Jacques, Jean-Francois Joanny, Peter Lenz, and Cecile Sykes (2008), "Cell motility," Chap. The physics of Listeria propulsion (Springer, New York) p. 1.

Purcell, E M (1977), "Life at low reynolds numbers," Am. J. Phys. **45**, 3.

Purcell, E M (1997), "The efficiency of propulsion by a rotating flagellum," Proc. Natl. Acad. Sci. USA **94**, 11307.

Pusey, P N, and W. van Megen (1986), "Phase behaviour of concentrated suspensions of nearly hard colloidal spheres,"

Nature **320**, 340.
Qian, Bian, Hongyuan Jiang, David A. Gagnon, Kenneth S. Breuer, and Thomas R. Powers (2009), "Minimal model for synchronization induced by hydrodynamic interactions," Phys. Rev. E **80**, 061919.
Rafaï, Salima, Levan Jibuti, and Philippe Peyla (2010), "Effective viscosity of microswimmer suspensions," Phys. Rev. Lett. **104**, 098102.
Ramaswamy, Sriram (2010), "The mechanics and statistics of active matter," Annual Review of Condensed Matter Physics **1** (1), 323–345.
Ramaswamy, Sriram, R Aditi Simha, and John Toner (2003), "Active nematics on a substrate: Giant number fluctuations and long-time tails," Europhys. Lett. **62** (2), 196.
Redner, Gabriel S, Michael F. Hagan, and Aparna Baskaran (2013), "Structure and dynamics of a phase-separating active colloidal fluid," Phys. Rev. Lett. **110**, 055701.
Reichert, M, and H. Stark (2005), "Synchronization of rotating helices by hydrodynamic interactions," Eur. Phys. J. E **17**, 493.
Reigh, S Y, R. G. Winkler, and G. Gompper (2012), "Synchronization and bundling of anchored bacterial flagella," Soft Matter **8**, 4363.
Reigh, S Y, R. G. Winkler, and G. Gompper (2013), "Synchronization, slippage, and unbundling of driven helical flagella," PLoS ONE **8**, e70868.
Riedel, Ingmar H, Karsten Kruse, and Jonathon Howard (2005), "A self-organized vortex array of hydrodynamically entrained sperm cells," Science **309**, 300–303.
Riedel-Kruse, IH, A. Hilfinger, and F. Jülicher (2007), "How molecular motors shape the flagellar beat," HFSP **1**, 192–208.
Riley, E E, and E. Lauga (2014), "Enhanced active swimming in viscoelastic fluids," EPL **108**, 34003.
Risken, H (1989), *The Fokker-Planck Equation* (Springer, Berlin).
Rodenborn, Bruce, Chih-Hung Chen, Harry L. Swinney, Bin Liu, and H. P. Zhang (2013), "Propulsion of microorganisms by a helical flagellum," Proc. Natl. Acad. Sci. USA **110**, E338.
Romanczuk, P, M. Bär, W. Ebeling, B. Lindner, and L. Schimansky-Geier (2012), "Active brownian particles," Eur. Phys. J. Special Topics **1**, 202.
Rothschild, L (1963), "Non-random distribution of bull spermatozoa in a drop of sperm suspension," Nature **198**, 1221–1222.
Rückner, Gunnar, and Raymond Kapral (2007), "Chemically powered nanodimers," Phys. Rev. Lett. **98**, 150603.
Rüffer, U, and W. Nultsch (1998), "Flagellar coordination in Chlamydomonas cells held on micropipettes," Cell Motil. Cytoskeleton **41**, 297.
Rusconi, Roberto, Jeffrey S. Guasto, and Roman Stocker (2014), "Bacterial transport suppressed by fluid shear," Nat. Phys. **10**, 212.
Rycroft, Chris H (2009), "VORO++: A three-dimensional voronoi cell library in C++," Chaos **19**, 041111.
Sabass, Benedikt, and Udo Seifert (2012), "Dynamics and efficiency of a self-propelled, diffusiophoretic swimmer," J. Chem. Phys. **136**, 064508.
Saintillan, David (2010), "Extensional rheology of active suspensions," Phys. Rev. E **81**, 056307.
Saintillan, David, and Michael J. Shelley (2013), "Active suspensions and their nonlinear models," C. R. Physique **14**, 497–517.
Sanchez, Samuel, and Martin Pumera (2009), "Nanorobots: The ultimate wireless self-propelled sensing and actuating devices," Chem. Asian J. **4**, 1402–1410.
Sanchez, Samuel, Alexander A. Solovev, Stefan M. Harazim, Christoph Deneke, Yong Feng Mei, and Oliver G. Schmidt (2011a), "The smallest man-made jet engine," The Chemical Record **11**, 367–370.
Sanchez, Timothy, David Welch, Daniela Nicastro, and Zvonimir Dogic (2011b), "Cilia-like beating of active microtubule bundles," Science **333**, 456–459.
Sanderson, M J, and M. A. Sleigh (1981), "Ciliary activity of cultured rabbit tracheal epithelium: beat pattern and metachrony," J. Cell Sci. **47**, 331–347.
Saragosti, J, P. Silberzan, and A. Buguin (2012), "Modeling *e. coli* tumbles by rotational diffusion. implications for chemotaxis," PLoS ONE **7**, e35412.
Schaller, Volker, Christoph Weber, Christine Semmrich, Erwin Frey, and Andreas R Bausch (2010), "Polar patterns of driven filaments," Nature **467** (7311), 73–77.
Scharf, B (2002), "Real-time imaging of fluorescent flagellar filaments of *Rhizobium lupini* H13-3: flagellar rotation and pH-induced polymorphic transitions," J. Bacteriol. **184**, 5979–5986.
Schmitt, R (2002), "Sinorhizobial chemotaxis: a departure from the enterobacterial paradigm," Microbiology **148**, 627.
Sengupta, Samudra, Michael E. Ibele, and Ayusman Sen (2012), "Fantastic voyage: Designing self-powered nanorobots," Angew. Chem. Int. Ed. **51**, 8434–8445.
Shah, Deepan S H, Tania Perehinec, Susan M. Stevens, Shin-Ichi Aizawa, and R. Elizabeth Sockett (2000), "The flagellar filament of rhodobacter sphaeroides: ph-induced polymorphic transitions and analysis of the flic gene," J. Bacteriol. **182**, 5218.
Simha, R Aditi, and Sriram Ramaswamy (2002), "Hydrodynamic fluctuations and instabilities in ordered suspensions of self-propelled particles," Phys. Rev. Lett. **89**, 058101.
Sivinski, J (1984), "Sperm in competition," in *Sperm Competition and the Evolution of Animal Mating Systems*, edited by R. L. Smith (Academic, Orlando) p. 174.
Sleigh, MA (1962), "2.the biology of cilia and flagella," Chap. The Structure of Cilia (Pergamon Press, Oxford) pp. 11–75.
Smith, D J, E. A. Gaffney, J. R. Blake, and J. C. Kirkman-Brown (2009), "Human sperm accumulation near surfaces: a simulation study," J. Fluid Mech. **621**, 289–320.
Sokolov, A, I. S. Aranson, J. O. Kessler, and R. E. Goldstein (2007), "Concentration dependence of the collective dynamics of swimming bacteria," Phys. Rev. Lett. **98** (15), 158102.
Sokolov, Andrey, and Igor S. Aranson (2009), "Reduction of viscosity in suspension of swimming bacteria," Phys. Rev. Lett. **103**, 148101.
Solari, C A, K. Drescher, and R. E. Goldstein (2011), "The flagellar photoresponse in volvox species," J. Phycol. **47**, 580–583.
Son, Kwangmin, Jeffrey S. Guasto, and Roman Stocker (2013), "Bacteria can exploit a flagellar buckling instability to change direction," Nat. Phys. **9**, 494.
Spagnolie, S E, and E. Lauga (2012), "Hydrodynamics of self-propulsion near a boundary: predictions and accuracy of far-field approximations," Journal of Fluid Mechanics **700**, 105–147.
Spagnolie, S E, B. Liu, and T. R. Powers (2013), "Locomotion of helical bodies in viscoelastic fluids: enhanced swimming

at large helical amplitudes," Phys. Rev. Lett. **111**, 068101.
Speck, Thomas, Julian Bialké, Andreas M. Menzel, and Hartmut Löwen (2014), "Effective cahn-hilliard equation for the phase separation of active brownian particles," Phys. Rev. Lett. **112**, 218304.
Stahl, S J, K. R. Stewart, and F. D. Williams (1983), "Extracellular slime associated with *proteus mirabilis* during swarming," J. Bacteriol. **154**, 930.
Stenhammar, Joakim, Davide Marenduzzo, Rosalind J. Allen, and Michael E. Cates (2014), "Phase behaviour of active Brownian particles: the role of dimensionality," Soft Matter **10**, 1489–1499.
Stenhammar, Joakim, Adriano Tiribocchi, Rosalind J. Allen, Davide Marenduzzo, and Michael E. Cates (2013), "Continuum theory of phase separation kinetics for active Brownian particles," Phys. Rev. Lett. **111**, 145702.
Stocker, R, and W. M. Durham (2009), "Tumbling for stealth," Science **325**, 400.
Strogatz, S H (2004), *Sync: How Order Emerges From Chaos In the Universe, Nature, and Daily Life* (Hyperion).
Sumino, Yutaka, Ken H Nagai, Yuji Shitaka, Dan Tanaka, Kenichi Yoshikawa, Hugues Chaté, and Kazuhiro Oiwa (2012), "Large-scale vortex lattice emerging from collectively moving microtubules," Nature **483** (7390), 448–452.
Surrey, Thomas, Francois Nédélec, Stanislas Leibler, and Eric Karsenti (2001), "Physical properties determining self-organization of motors and microtubules," Science **292**, 1167–1171.
Szabó, B, G. J. Szöllösi, B. Gönci, Zs. Jurányi, D. Selmeczi, and Tamás Vicsek (2006), "Phase transition in the collective migration of tissue cells: Experiment and model," Phys. Rev. E **74**, 061908.
Tailleur, J, and M. E. Cates (2008), "Statistical mechanics of interacting run-and-tumble bacteria," Phys. Rev. Lett. **100**, 218103.
Tailleur, J, and M. E. Cates (2009), "Sedimentation, trapping, and rectification of dilute bacteria," Epl **86** (6), 60002.
Tamm, S L, and G. A. Horridge (1970), "Relation between orientation of central fibrils and direction of beat in cilia of opalina," Proc. R. Soc. Lond. B **175**, 219.
Tavaddod, S, M. A. Charsooghi, F. Abdi, H. R. Khalesifard, and R. Golestanian (2011), "Probing passive diffusion of flagellated and deflagellated escherichia coli," Eur. Phys. J. E **34** (2), 1–7.
Taylor, G I (1951), "Analysis of the swimming of microscopic organisms," Proc. Roy. Soc. Lond. A **209**, 447–461.
Thakur, Snigdha, and Raymond Kapral (2011), "Dynamics of self-propelled nanomotors in chemically active media," J. Chem. Phys. **135**, 024509.
Theers, Mario, and Roland G. Winkler (2013), "Synchronization of rigid microrotors by time-dependent hydrodynamic interactions," Phys. Rev. E **88**, 023012.
Theurkauff, I, C. Cottin-Bizonne, J. Palacci, C. Ybert, and L. Bocquet (2012), "Dynamic clustering in active colloidal suspensions with chemical signaling," Phys. Rev. Lett. **108**, 268303.
Thutupalli, S, R. Seemann, and S. Herminghaus (2011), "Swarming behavior of simple model squirmers," New. J. Phys. **13**, 073021.
Tierno, P, R. Golestanian, I. Pagonabarraga, and F. Sagues (2008), "Controlled swimming in confined fluids of magnetically actuated colloidal rotors," Phys. Rev. Lett. **101**, 218304.
Tirado, M M, C. López Martínez, and J. G. de la Torre (1984), "Comparison of theories for the translational and rotational diffusion coefficients of rod-like macromolecules. application to short DNA fragments," J. Chem. Phys. **81**, 2047.
Toner, J, Y. Tu, and S. Ramaswamy (2005a), "Hydrodynamics and phases of flocks," Ann. Phys. (N.Y.) **318**, 170.
Toner, John, and Yuhai Tu (1995), "Long-range order in a two-dimensional dynamical XY model: How birds fly together," Phys. Rev. Lett. **75**, 4326–4329.
Toner, John, Yuhai Tu, and Sriram Ramaswamy (2005b), "Hydrodynamics and phases of flocks," Ann. Phys. **318** (1), 170–244.
Trepat, X, M. R. Wasserman, T. E. Angelini, E. Millet, D. A. Weitz, J. P. Butler, and J. J. Fredberg (2009), "Physical forces during collective cell migration," Nature Physics **5**, 426–430.
Turner, L, R. Zhang, N. C. Darnton, and H. C. Berg (2010), "Visualization of flagella during bacterial swarming," J. Bacteriol. **192**, 3259.
Turner, Linda, William S. Ryu, and Howard C. Berg (2000), "Real-Time Imaging of Fluorescent Flagellar Filaments," J. Bacteriol. **182** (10), 2793.
Tuson, H H, M. F. Copeland, S. Carey, R. Sacotte, and D. B. Weible (2013), "Flagellum density regulates *proteus mirabilis* swarmer cell motility in viscous environments," J. Bacteriol. **195**, 368.
Uchida, Nariya, and Ramin Golestanian (2010), "Synchronization and collective dynamics in a carpet of microfluidic rotors," Phys. Rev. Lett. **104**, 178103.
Uchida, Nariya, and Ramin Golestanian (2011), "Generic conditions for hydrodynamic synchronization," Phys. Rev. Lett. **106**, 058104.
Uchida, Nariya, and Ramin Golestanian (2012), "Hydrodynamic synchronization between objects with cyclic rigid trajectories," Eur. Phys. J. E **35**, 1.
Uhlenbeck, G E, and L. S. Ornstein (1930), "On the theory of the Brownian motion," Phys. Rev. **36**, 823.
Uppaluri, Sravanti, Jan Nagler, Eric Stellamanns, Niko Heddergott, Stephan Herminghaus, Markus Engstler, and Thomas Pfohl (2011), "Impact of microscopic motility on the swimming behavior of parasites: Straighter trypanosomes are more directional," PLoS Comp. Biol. **7**, e1002058.
Vicsek, T, A. Czirók, E. Ben-Jacob, I. Cohen, and O. Shochet (1995a), "Novel type of phase transition in a system of self-driven particles," Phys. Rev. Lett. **75**, 1226.
Vicsek, Tamás, András Czirók, Eshel Ben-Jacob, Inon Cohen, and Ofer Shochet (1995b), "Novel type of phase transition in a system of self-driven particles," Phys. Rev. Lett. **75**, 1226–1229.
Vicsek, Tamás, and Anna Zafeiris (2012), "Collective motion," Phys. Rep. **517**, 71–140.
Vilfan, Andrej, and Frank Jülicher (2006), "Hydrodynamic flow patterns and synchronization of beating cilia," Phys. Rev. Lett. **96**, 058102.
Vogel, Reinhard, and Holger Stark (2010), "Force-extension curves of bacterial flagella," Eur. Phys. J. E **33**, 259.
Vogel, Reinhard, and Holger Stark (2013), "Rotation-induced polymorphic transitions in bacterial flagella," Phys. Rev. Lett. **110**, 158104.
Voituriez, R, J. F. Joanny, and J. Prost (2006), "Generic phase diagram of active polar films," Phys. Rev. Lett. **96**, 028102.

Volpe, G, I. Buttinoni, D. Vogt, H. J. Kümmerer, and C. Bechinger (2011), "Microswimmers in patterned environments," Soft Matter **7**, 8810.

Wang, Q, J. Pan, and W. J. Snell (2006), "Intraflagellar transport particles participate directly in cilium-generated signaling in Chlamydomonas," Cell **125**, 549.

Wang, Wei, Wentao Duan, Ayusman Sen, and Thomas E. Mallouk (2013), "Catalytically powered dynamic assembly of rod-shaped nanomotors and passive tracer particles," Proc. Natl. Acad. Sci. USA **110**, 17744–17749.

Wensink, H H, J. Dunkel, S. Heidenreich, K. Drescher, R. E. Goldstein, H. Löwen, and J. M. Yeomans (2012), "Mesoscale turbulence in living fluids," Proc. Natl. Acad. Sci. USA **109**, 14308.

Wensink, H H, V. Kantsler, R. E. Goldstein, and J. Dunkel (2014), "Controlling active self-assembly through broken particle-shape symmetry," Phys. Rev. E **89**, 010302(R).

Wensink, H H, and H. Löwen (2008), "Aggregation of self-propelled colloidal rods near confining walls," Phys. Rev. E **78**, 031409.

Williams, Brian J, Sandeep V. Anand, Jagannathan Rajagopalan, and M. Taher A. Saif (2014), "A self-propelled biohybrid swimmer at low reynolds number," Nat. Commun. **5**, 3081.

Winet, H, G. S. Bernstein, and J. Head (1984), "Observations on the response of human spermatozoa to gravity, boundaries and fluid shear," J. Reprod. Fert. **70**, 511–523.

Winkler, R G (2007), "Diffusion and segmental dynamics of rodlike molecules by fluorescence correlation spectroscopy," J. Chem. Phys. **127**, 054904.

Wittkowski, Raphael, Adriano Tiribocchi, Joakim Stenhammar, Rosalind J. Allen, Davide Marenduzzo, and Michael E. Cates (2014), "Scalar ϕ^4 field theory for active-particle phase separation," Nat. Commun. **5**, 4351.

Wolgemuth, Charles W (2008), "Collective swimming and the dynamics of bacterial turbulence," Biophys. J. **95**, 1564–1574.

Wollin, C, and H. Stark (2011), "Metachronal waves in a chain of rowers with hydrodynamic interactions," Eur. Phys. J. E **34**, 42.

Woolley, D M (2003), "Motility of spermatozoa at surfaces," Reprod. **126**, 259–270.

Woolley, David M, Rachel F. Crockett, William D. I. Groom, and Stuart G. Revell (2009), "A study of synchronization between the flagella of bull spermatozoa, with related observations," J. Exp. Biol. **212**, 2215–2223.

Wysocki, A, R. G. Winkler, and G. Gompper (2014), "Cooperative motion of active Brownian spheres in three-dimensional dense suspensions," EPL **105**, 48004.

Xing, Jianhua, Fan Bai, Richard Berry, and George Oster (2006), "Torque-speed relationship of the bacterial flagellar motor," Proc. Natl. Acad. Sci. USA **103**, 1260.

Yang, Xingbo, M. Lisa Manning, and M. Cristina Marchetti (2014a), "Aggregation and segregation of confined active particles," Soft Matter **10**, 6477.

Yang, Yingzi, Jens Elgeti, and Gerhard Gompper (2008), "Cooperation of sperm in two dimensions: Synchronization, attraction and aggregation through hydrodynamic interactions," Phys. Rev. E **78**, 061903 [1–9].

Yang, Yingzi, Vincent Marceau, and Gerhard Gompper (2010), "Swarm behavior of self-propelled rods and swimming flagella," Phys. Rev. E **82**, 031904 [1–13].

Yang, Yingzi, Feng Qiu, and Gerhard Gompper (2014b), "Self-organized vortices of circling self-propelled particles and curved active flagella," Phys. Rev. E **89**, 012720 [1–14].

Zheng, Xu, Borge ten Hagen, Andreas Kaiser, Meiling Wu, Haihang Cui, Zhanhua Silber-Li, and Hartmut Löwen (2013), "Non-gaussian statistics for the motion of self-propelled janus particles: Experiment versus theory," Phys. Rev. E **88**, 032304.

Zhu, L, E. Lauga, and L. Brandt (2012), "Self-propulsion in viscoelastic fluids: pushers vs. pullers," Phys. Fluids **24**, 051902.

Zöttl, Andreas, and Holger Stark (2012), "Nonlinear dynamics of a microswimmer in Poiseuille flow," Phys. Rev. Lett. **108**, 218104.

Zöttl, Andreas, and Holger Stark (2013), "Periodic and quasiperiodic motion of an elongated microswimmer in poiseuille flow," Eur. Phys. J. E **36**, 1.

Zöttl, Andreas, and Holger Stark (2014), "Hydrodynamics determines collective motion and phase behavior of active colloids in quasi-two-dimensional confinement," Phys. Rev. Lett. **112**, 118101.